RESEARCH ARTICLE | MAY 12 2025

Lattice Boltzmann method simulation of rotating channel flows: Improved modeling of diffusion and advection terms

Special Collection: Proceedings of the 33rd Conference on Discrete Simulation of Fluid Dynamics

Goncalo Silva ; Irina Ginzburg

Physics of Fluids 37, 052010 (2025)
https://doi.org/10.1063/5.0268025

Physics of Fluids ARTICLE pubs.aip.org/aip/pof

Lattice Boltzmann method simulation of rotating channel flows: Improved modeling of diffusion and advection terms

Cite as: Phys. Fluids **37**, 052010 (2025); doi: 10.1063/5.0268025
Submitted: 27 February 2025 · Accepted: 14 April 2025 ·
Published Online: 12 May 2025

View Online Export Citation CrossMark

Goncalo Silva[1,a)] and Irina Ginzburg[2]

AFFILIATIONS

[1]IDMEC, Mechatronics Engineering Department, University of Évora, R. Romão Ramalho 59, 7000-671 Évora, Portugal
[2]INRAE, Centre IDF Jouy-En-Josas/Antony, Université Paris-Saclay, 78352 Jouy-en-Josas, France

Note: This paper is part of the Special Topic, Proceedings of the 33rd Conference on Discrete Simulation of Fluid Dynamics.
[a)]**Author to whom correspondence should be addressed:** gnsilva@uevora.pt

ABSTRACT

This work presents an extensive analysis of the lattice Boltzmann method for solving rotating fluid flows inside channel-like geometries, a topic relevant to many scientific and engineering fields. The present research investigates the role of the collision operator, equilibrium and source term formulations, the number of discrete velocities in three-dimensional cubic lattices, and boundary schemes applied to this problem class. Here, it is considered the two-relaxation-time (TRT) collision operator with both equilibrium and source terms represented on the Hermite expansion formalism. Denoting by $\mathcal{H}^{(n)}$ the n-order Hermite orthonormal basis, the TRT modeling of the isothermal Navier–Stokes equations expands the symmetric and anti-symmetric components of equilibrium up to $\mathcal{H}^{(2)}$ and $\mathcal{H}^{(1)}$, respectively, and at $\mathcal{H}^{(1)}$ for the external source term, featuring the Coriolis force. This study proposes higher-order expansions of equilibrium and source terms to improve the accuracy of diffusion and advection in rotating fluids. Diffusion modeling is improved by including an $\mathcal{H}^{(3)}$ correction to the source term expansion to remedy artifacts from the Coriolis force discretization. Advection modeling is improved by including an $\mathcal{H}^{(4)}$ correction to the $\mathcal{H}^{(2)}$ expansion of the symmetric equilibrium in the D3Q19 lattice to retrieve an isotropy comparable to the D3Q27. These improvements are derived based on the exact analytical solution of the TRT equation at the discrete level and the steady Chapman–Enskog fourth-order expansion of the TRT solution, respectively, applied to two well-known benchmarks in this problem class: the Poiseuille–Ekman channel flow and the rotating square duct flow.

I. INTRODUCTION

Flows subject to rotational effects are relevant in numerous theoretical and applied fields.[1] Examples range from large-scale unbounded systems, as in geophysical fluid flow problems (e.g., in atmospheric or oceanic forecasting[2]) to geometrically constrained domains, such as in rotary machinery (e.g., in turbine or compressor technologies[3]) or in bioengineering devices (e.g., in centrifuge or lab-on-a-CD platforms[4]). The present study concerned with the modeling of rotating fluid flows inside channel-like geometries within physical regimes typically found in the microfluidic lab-on-a-CD platform.[5,6] This setup encapsulates key flow mechanisms induced by rotation,[7–11] which are known to be challenging to numerical approximations.[6,12] With this objective in mind, the present contribution intends to obtain accurate numerical solutions of the steady, isothermal, and incompressible Navier–Stokes equations[13] (NSEs) in a frame rotating with constant angular velocity $\vec{\Omega}$, given by

$$\vec{\nabla}\cdot\vec{u}=0, \tag{1a}$$

$$(\vec{u}\cdot\vec{\nabla})\,\vec{u}=\vec{a}-2\,\vec{\Omega}\times\vec{u}-\frac{1}{\rho_0}\vec{\nabla}P+\nu\nabla^2\vec{u}. \tag{1b}$$

Equations (1) solve for the fluid velocity $\vec{u}$ and the reduced pressure P, where $P=p-\frac{1}{2}\rho_0(\vec{\Omega}\times\vec{R})^2$ denotes the difference between static pressure p and the centrifugal potential $\frac{1}{2}\overline{\rho}(\vec{\Omega}\times\vec{R})^2$ in the rotating system.[7,8,11] The possibility of fluid motion being generated by a constant external acceleration field $\vec{a}$, e.g., due to gravity, is also considered. For simplicity, the thermophysical parameters ρ_0 (mass density) and ν (kinematic viscosity) are constants. At walls, Eqs. (1)

are considered to satisfy the no-slip velocity boundary conditions (BCs).

As it happens with the generality of fluid mechanics problems, the analytical study of rotating fluid flows is often untractable; notable exceptions are compiled by Wang.[14] The alternative route to solve Eqs. (1) typically relies on computational fluid dynamics (CFD) methods.[15,16] At present, traditional CFD tools have reached a consistent and mature state of development to handle the specificities of the rotating NSEs modeling.[15,16] However, given the popularity of the lattice Boltzmann method[17–22] (LBM) as an alternative CFD technique, it is pertinent to inquire about its performance in the modeling of this problem class. To the best of our knowledge, this question has not been the subject of a dedicated analysis yet.

In fact, research on the LBM modeling of flows subject to rotational effects has experienced rather irregular progress. One of the earliest LBM publications in this field was due to Salmon[23,24] in the context of geophysical applications. Inspired by Salmon's works, Dellar[25] proposed an *a priori* derivation of the LBM for rotating fluids starting from the continuous Boltzmann equation, where focus was put on the derivation of the source term in LBM. Although his work[25] was never published, it is noteworthy acknowledging that the very popular Guo forcing strategy[26] can already be found in that research. About the same time, Shi-De *et al.*[27] also considered the LBM modeling of flows in a Coriolis field but focused on the LBM equilibrium formulation, where they proposed a third-order expansion. Subsequent works adopted the existing LBM frameworks, typically relying upon Guo *et al.* work,[25,26] but viewing applications in diverse scientific fields. For example, Yu *et al.*[28] and Liou and Wang[29,30] considered the rotating frame formulation of LBM, based on the aforementioned works,[25,26] to study turbulent flows under rotating fields. Zhang *et al.*[31] focused on the impact of rotation over the secondary flow patterns. Basha *et al.*,[32] Kardani *et al.*,[33] and Werner *et al.*[34] studied the interplay between the flow rotation and other phenomena, such as thermal effects, porous media transport, and buoyancy, respectively. Zhou *et al.*[35] investigated turbomachinery flows, while Maneshian *et al.*[36] considered the effect of rotation on multiphase flows with application to bubble dynamics. Finally, Zhang *et al.*,[37] Far *et al.*,[38] and Yoo *et al.*[39] investigated the simulation of rotating objects within the LBM framework, although their description, based on moving meshes, is beyond the scope of the present work.

From the above literature review, one can conclude that the vast majority of studies dedicated to the LBM modeling of rotating fluids have been more concerned with applications than with the fundamentals. In practice, most of the aforementioned studies have taken for granted the consistency of preexisting LBM formulations in rotating frames, disregarding the emergence of possible artifacts due to the numerical approximations, which are specifically introduced in the modeling of this problem class. Hence, the objective of the present work is to perform a comprehensive theoretical assessment on this subject, searching for potential weaknesses and proposing suitable corrections to make LBM a reliable and competitive CFD tool to model rotating fluids.

In terms of numerical models, this work will focus on the LBM with the two-relaxation-time (TRT) collision operator.[40–42] This choice is justified by the TRT ability to model the steady-state NSEs in a physically consistent manner, meaning without the interference of the undesirable "viscosity-dependent" numerical errors[42–45] due to its extra relaxation collision. Putting this requisite in the context of the present study, we have that dimensionless solutions of Eqs. (1) are expected to be controlled by two dimensionless physical groups, such as the Reynolds and the Ekman numbers (to be defined later in the manuscript). However, single-relaxation-time collision models, typified by the Bhatnagar–Gross–Krook (BGK)[46] operator, do not support this parametrization property.[42,44] For example, two BGK models running on the same grid at the same Reynolds and Ekman numbers have the scope to yield two distinct steady-state solutions when two different viscosity values are used. This result is in strict contradiction with the basic principle of dimensional similarity, raising immediate reservations in the assessment of some previously published works that, as laid down on the BGK model, disqualify possible comparisons between them. The TRT model rectifies this defect in an inexpensive manner.

The distinctive point of the present contribution lies in the combination of two distinct LBM formalisms. On the one hand, we adopt the symmetrized structure of the TRT scheme, which splits the collision elements into symmetric and anti-symmetric parts.[40–42] On the other hand, the symmetric and anti-symmetric components of the equilibrium and external source terms are expressed under the Hermite basis framework.[47,48] Denoting by $\mathcal{H}^{(n)}$ the n-order Hermite orthonormal basis, then symmetric and anti-symmetric components of the NSE equilibrium are typically expanded up to $\mathcal{H}^{(2)}$ and $\mathcal{H}^{(1)}$ terms, respectively, and the external source term is projected onto the $\mathcal{H}^{(1)}$ basis only. This work provides further evidence that the inclusion of $\mathcal{H}^{(2)}$ terms in the source term formulation, which boils down to using the so-called Guo forcing strategy,[26] introduces undesirable terms, which damage the LBM accuracy[49,50] and, worse, corrupt the "viscosity-independent" parametrization property of the TRT scheme.[51,52] The main objective of the present work is to investigate to which extent the symmetric and anti-symmetric components of the equilibrium and source term formulations, which typically do not exceed the $\mathcal{H}^{(2)}$ projections, may give rise to numerical errors in the LBM modeling of rotating channel flow problems. Based on this analysis, the subsequent step of this work consists of the development of possible strategies to eliminate or, at least, to mitigate LBM numerical errors recurring to expansions on higher-order Hermite bases. For example, the present work indicates that including $\mathcal{H}^{(3)}$ terms in the anti-symmetrical part of the external source and $\mathcal{H}^{(4)}$ terms in the symmetrical part of the NSEs equilibrium leads to a significant accuracy improvement in the LBM modeling of rotating flows.

The identification of discretization artifacts coming from the LBM modeling of the external source term, which takes the form of a discrete Laplacian of the source, has been previously reported in the literature.[44,51,53–57] This shortcoming is particularly harmful when the source term is solution dependent since the unphysical Laplacian of the source term becomes similar in structure to the physical diffusion term. Then, the two may potentially lead to undesirable interferences in the discrete equations solved by LBM. This issue was recognized, for the first time, by Nie and Martys[53] in the context of the LBM Brinkman modeling of porous media flows. Immediately after, Ginzburg[44] clarified the origin of this defect and proposed a correction method. Further correction methods were proposed and examined in a subsequent unpublished work.[54] Later, Ginzburg *et al.*[55–57] developed a correction method that absorbs the artifacts of the Brinkman source term by resorting to a solution-dependent modification of the TRT-free relaxation rate. Overall, this strategy[55,56] was found superior in

performance. Unfortunately, its operation principle is not directly applicable to the Coriolis force modeling in rotating fluids as the numerical artifacts that arise in this case cannot be totally absorbed into the TRT relaxation rates, as it happens with the Brinkman force.

To overcome this limitation, this work revisits an alternative correction strategy developed in a previous contribution.[54] While originally constructed for Brinkman models, we will show that its use is particularly effective in the modeling of Coriolis forces for rotating fluids. Translating into the Hermite basis formalism, this early methodology,[54] named as "anisotropic force weights,"[44] is equivalent to including $\mathcal{H}^{(3)}$ projections into the LBM source term formulation that typically is built upon a $\mathcal{H}^{(1)}$ expansion. Still on this subject, the works[55,56] also pointed out the importance of the source term artifacts and their impact, not only in the bulk flow scheme but also on the setting of the conditions prescribed at boundaries. Often, the interplay between the external source and the boundary model ends up being the leading order error source. For that reason, this issue is also addressed in the present work. Here, the accommodation of rotating fluid flows on no-slip walls is examined, considering the two most popular operation principles underlying LBM boundary schemes: the (off-node) linkwise strategy, e.g., bounce-back (BB)[58–60] or multireflection[41,43,45,61,62] schemes, and the (on-node) wet node boundary model, e.g., the local second-order boundary (LSOB) scheme,[63–66] non-equilibrium bounce-back by Zou and He[67] or other methods.[68–70] To accurately model arbitrary-shaped walls within this problem class, a specific correction to eliminate the Coriolis source term artifacts is proposed to be included in the well-established modified linear interpolation (MLI) boundary scheme,[41,45,62] which is a parabolic accurate linkwise boundary scheme alternative to the multireflection class.[43] The MLI scheme was originally proposed in the work,[41] then thoroughly examined in the study,[45] and recently reinterpreted in the contribution[62] through a parabolic correction of the pressure-gradient accurate linear interpolations (so-called LI$^{(4)}$ class[43]). Everything considered, the effect of the source term and the boundary scheme will be examined through the testing of a Poiseuille–Ekman flow between parallel plates, discretized either aligned or arbitrarily inclined with respect to the LBM mesh. Comparisons between the LBM discretization and the popular finite element method (FEM) are also included in this study.

Numerical evidence on the lack of rotational invariance of LBM solutions produced by reduced cubic lattice models with 15 and 19 discrete velocities,[71] so-called D3Q15 and D3Q19, respectively, has also been reported in numerous publications.[72–76] The root of this defect was explained on the basis of truncation error analyses.[75,76] Through theoretical studies, it was pointed out the link between the anisotropy of the D3Q15 and D3Q19 solutions and the angular-dependent structure of the truncation error terms of the momentum advection. Alternatively, this deficiency would only cease to exist if the NSEs were modeled with the 27 discrete velocity lattice, D3Q27. In common, the D3Q15, D3Q19, and D3Q27 lattice models considered in those studies employed the same LBM equilibrium structure to model the NSEs, based on the Hermite expansion of the Maxwell–Boltzmann continuous equilibrium up to $\mathcal{H}^{(2)}$ basis. By recognizing this fact, it was later proposed[77,78] the introduction of specific amendments to the standard LBM equilibrium that would correct the anisotropy defects of the D3Q19 lattice. Such an improved equilibrium (IE) for the D3Q19 lattice was initially developed[77,78] via a top-down approach, based on a steady Chapman–Enskog fourth-order expansion that was previously developed.[75] Subsequently, Coreixas *et al.*[79] deduced the same D3Q19 improved equilibrium via a bottom-up procedure; that is, by looking for the isotropy requirements directly on the equilibrium state formulation at the lattice level. This same procedure was also pursued by other researchers.[80] In the end, both top-down and bottom-up approaches lead to the same improved equilibrium for the D3Q19 lattice that guarantees rotationally invariant LBM solutions. Compared to the standard equilibrium (SE), this improved equilibrium formulation for the D3Q19 lattice includes the projection of the non-linear momentum term not only on the $\mathcal{H}^{(2)}$ basis but also on the $\mathcal{H}^{(4)}$ basis. As demonstrated in the present work, the use of this improved equilibrium is fundamental when solving rotating fluid flows on the D3Q19 lattice. Otherwise, the induced lattice artifacts may compete with the Coriolis source terms at the discrete level, and lead to numerical solutions that are seriously distorted or even completely corrupted. These LBM results, for both D3Q19 and D3Q27 lattices, will be illustrated in this work and further compared against results from other more well-established CFD solvers, such as the FEM, in application to this problem class.

The remainder of the manuscript is organized as follows. Section II introduces the lattice Boltzmann method (LBM) and the two-relaxation-time (TRT) collision operator, with a focus on the equilibrium and source term formulations based on the Hermite expansion formalism. Also, the different LBM boundary schemes utilized in this work are introduced at the end of Sec. II. Section III covers the modeling of the Poiseuille–Ekman rotating channel flow. The effect of the source term formulation for the Coriolis force modeling and the switch from the linkwise boundary schemes vs the wet node ones are the primary topics of discussion here. Section IV concerns the modeling of a rotating square duct flow problem. Here, the relationship between the lattice choice and the LBM equilibrium is thoroughly investigated, revealing the importance of the advection term modeling. Section V concludes the work with a summary of the main findings and guidelines for the LBM modeling of rotating fluid flows. Additionally, Appendix A discusses the TRT formulation of the popular Guo forcing model[26] and its inconsistency in modeling stationary solutions in rotating systems. Appendix B presents alternative formulations for writing the LBM standard and improved equilibria in a computationally more efficient manner. Appendix C provides details on the derivations leading to the bulk flow results presented in Sec. III. Appendix D details the derivation steps leading to the MLI boundary scheme, devised to handle the specificities of this problem class. Finally, Appendix E presents details on the steady-state Chapman–Enskog fourth-order expansion considering different equilibria and cubic lattice choices.

II. LATTICE BOLTZMANN METHOD

A. Two-relaxation-time (TRT) model

The lattice Boltzmann method[17–22] (LBM) solves for the populations $f_q(\vec{x}, t)$, defined on configuration space $\vec{x}$ and time t, along a discrete velocity set, called lattice, which features one immobile $\vec{c}_0 = \vec{0}$ and $Q_m = Q - 1$ non-zero velocity vectors $\vec{c}_q$ per grid node. The first $Q_m/2$ velocity vectors $\vec{c}_q$ are set diametrically opposite to the other $Q_m/2$ vectors $\vec{c}_{\bar{q}} = -\vec{c}_q$, where the pair $\{\vec{c}_q, \vec{c}_{\bar{q}}\}$ is referred to as a link. This work considers the D3Q19 and D3Q27 cubic lattices,[21,46,75] which are depicted in Fig. 1.

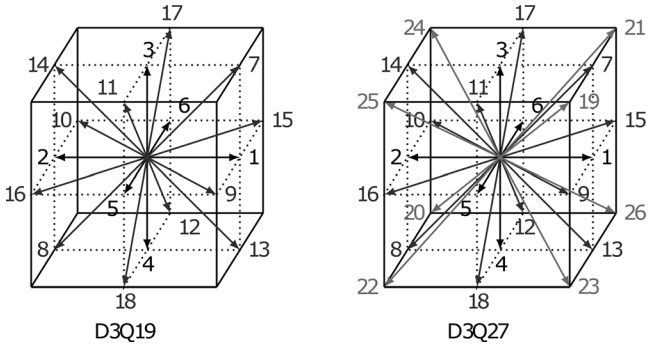

FIG. 1. Lattice structures of D3Q19 and D3Q27 discrete velocity sets, based on the notation of the LBM textbook.[21]

The LBM update rule operates over a succession of streaming, given by Eq. (2a), and collision steps, given by Eqs. (2b)–(2d). This work adopts the two-relaxation-time (TRT) model,[40–42] which formulates based on the symmetry argument that any lattice quantity ψ_q can be decomposed into symmetric and anti-symmetric components as follows: $\psi_q^{\pm} = \frac{1}{2}(\psi_q \pm \psi_{\overline{q}})$. The LBM-TRT evolution equations are expressed as

$$f_q(\vec{x}+\vec{c}_q, t+1) = \hat{f}_q(\vec{x}, t), \quad q = 0, 1, \ldots, Q-1, \tag{2a}$$

$$\hat{f}_0(\vec{x}, t) = [f_0 + \hat{n}_0](\vec{x}, t), \quad \hat{n}_0 = -\frac{1}{\tau^+}(f_0 - e_0), \quad q = 0, \tag{2b}$$

$$\hat{f}_q(\vec{x}, t) = \left[f_q + \hat{n}_q^+ + \hat{n}_q^-\right](\vec{x}, t), \quad \hat{n}_q^{\pm} = -\frac{1}{\tau^{\pm}}\left(f_q^{\pm} - e_q^{\pm}\right), \quad q = 1, \ldots, \frac{Q_m}{2}, \tag{2c}$$

$$\hat{f}_{\overline{q}}(\vec{x}, t) = \left[f_{\overline{q}} + \hat{n}_q^+ - \hat{n}_q^-\right](\vec{x}, t), \quad \vec{c}_{\overline{q}} = -\vec{c}_q, \quad \overline{q} = \frac{Q_m}{2} + 1, \ldots, Q-1. \tag{2d}$$

In terms of notation, f_q denotes the LBM populations composed of equilibrium $e_q^{\pm}$ and non-equilibrium $n_q^{\pm} = f_q^{\pm} - e_q^{\pm}$ components. The post-collision state of populations is denoted by $\hat{f}_q$ and the post-collision non-equilibrium term is defined by $\hat{n}_q = -\frac{1}{\tau^{\pm}} n_q$. The relaxation times $\tau^{\pm} > \frac{1}{2}$ determine the two positive relaxation functions $\Lambda^{\pm}$ and their product according to

$$\Lambda^{\pm} = \left(\tau^{\pm} - \frac{1}{2}\right) \quad \text{and} \quad \Lambda = \Lambda^+\Lambda^-. \tag{3}$$

For the modeling of NSEs, Λ^+ determines the fluid kinematic viscosity

$$\nu = \frac{1}{3}\Lambda^+, \tag{4}$$

and Λ^- is typically determined by the choice of Λ, following Eq. (3). For steady solutions, the relaxation parameter $\Lambda > 0$ (so-called "magic" parameter) controls the bulk and boundary truncation terms. The consequence is that, with Λ fixed, the TRT[41,42] steady solutions in dimensionless form, when set on the same grid, are identical for any variation of the dimensionless groups governing the physical problem.

Remark 2.1. The single-relaxation-time (BGK) collision model only operates with $\tau = \tau^{\pm}$. Consequently, the "magic" parameter becomes given by $\Lambda = 9\nu^2$, which will give rise to viscosity-dependent numerical errors. In practice, although running on the same grid and with the same physical dimensionless numbers, two BGK steady solutions in dimensionless form will differ if the ν assigned is distinct. In other words, the BGK steady solutions do not support the principle of dimensional similarity above the second-order polynomial solutions.[41,42,45]

At steady state, the TRT evolution equations, given by Eq. (2), can be equivalently expressed through the following two exact recurrence equations:[42,44]

$$\hat{n}_q^{\pm}(\vec{x}) = \left[\overline{\Delta}_q e_q^{\mp} - \Lambda^{\mp}\overline{\Delta}_q^2 e_q^{\pm} + \left(\Lambda - \frac{1}{4}\right)\overline{\Delta}_q^2 \hat{n}_q^{\pm}\right](\vec{x}), \tag{5a}$$

$$(\overline{\Delta}_q^2 e_q^{\pm} - \Lambda^{\pm}\overline{\Delta}_q^2 \hat{n}_q^{\pm} - \overline{\Delta}_q \hat{n}_q^{\mp})(\vec{x}) = 0, \tag{5b}$$

with the two linkwise finite-difference operators defined as follows:

$$\begin{aligned} \overline{\Delta}_q \psi(\vec{x}) &= \frac{1}{2}\left[\psi(\vec{x}+\vec{c}_q) - \psi(\vec{x}-\vec{c}_q)\right], \\ \overline{\Delta}_q^2 \psi(\vec{x}) &= \psi(\vec{x}+\vec{c}_q) - 2\,\psi(\vec{x}) + \psi(\vec{x}-\vec{c}_q), \end{aligned} \tag{6}$$

where ψ denotes an arbitrary variable.

Equations (5a) and (5b) are useful as they provide explicit access to the $\hat{n}_q^{\pm}(\vec{x})$ solution. In this work, they will be used to set the content of $\hat{n}_q^{\pm}(\vec{x})$ either in exact form (refer to Sec. III B and Appendix C) or in approximated form (refer to Sec. IV B and Appendix E).

B. Standard equilibrium (SE) and standard force (SF) models

The TRT scheme is designed to approximate the incompressible NSEs,[81,82] given by Eq. (1). The equilibrium is split into symmetric e_q^+ and anti-symmetric e_q^- components as follows:[40–42,44]

$$e_q^+ = P_q + E_q, \tag{7a}$$

$$e_q^- = j_q + \Lambda^- F_q. \tag{7b}$$

The anti-symmetric external source term F_q is put into the equilibrium following previous works.[41,44]

The NSE equilibrium features the following macroscopic quantities. The pressure P is related to the mass density ρ through the state equation $P = c_s^2\,\rho$, where c_s^2 is a free tunable parameter[83] (so-called "squared speed of sound"). The momentum density $\vec{j}$ is related to the fluid velocity $\vec{u}$ as $\vec{j} = \rho_0\,\vec{u}$, where ρ_0 is a constant (background) mass density.[82] The external force density $\vec{F}$ is related to the external acceleration field $\vec{a}$ through $\vec{F} = \rho_0\,\vec{a}$. Altogether, these macroscopic variables are projected onto the (lattice) discrete velocity space, formed by an orthonormal basis, here denoted by the Hermite polynomials,

$$\begin{aligned} P_q &= t_q\,\mathcal{H}_q^{(0)} P \\ &= t_q\,P, \end{aligned} \tag{8a}$$

$$\begin{aligned} E_q &= 3\,t_q\,\mathcal{H}_{q\alpha\beta}^{(2)}\,\frac{j_\alpha j_\beta}{2\,\rho_0} \\ &= 3\,t_q\left(c_{q\alpha}c_{q\beta} - \frac{1}{3}\delta_{\alpha\beta}\right)\frac{j_\alpha j_\beta}{2\,\rho_0}, \end{aligned} \tag{8b}$$

$$j_q = t_q\,\mathcal{H}^{(1)}_{q\alpha}\,j_\alpha = t_q\,c_{q\alpha}\,j_\alpha, \tag{8c}$$

$$F_q = t_q\,\mathcal{H}^{(1)}_{q\alpha}\,F_\alpha = t_q\,c_{q\alpha}\,F_\alpha. \tag{8d}$$

Above, the first three Hermite polynomials[21,47,48] have been introduced

$$\mathcal{H}^{(0)}_q = 1, \quad \mathcal{H}^{(1)}_{q\alpha} = c_{q\alpha}, \quad \mathcal{H}^{(2)}_{q\alpha\beta} = c_{q\alpha}c_{q\beta} - \frac{1}{3}\delta_{\alpha\beta}. \tag{9}$$

Remark 2.2. The TRT model formulated on the Hermite basis formalism obeys the following rule. The TRT symmetric components, denoted by index (+), must only contain macroscopic variables projected onto even Hermite bases $\mathcal{H}^{(2n)}_q$ with $n \in \mathbb{N}_0$. The TRT anti-symmetric components, denoted by index (−), must only contain macroscopic variables projected onto odd Hermite bases $\mathcal{H}^{(2n+1)}_q$ with $n \in \mathbb{N}_0$. To approximate the isothermal NSEs, it suffices to consider Hermite projections in the equilibria up to the following orders: e^+_q up to $\mathcal{H}^{(2)}_q$ and e^-_q up to $\mathcal{H}^{(1)}_q$. On this basis, the leading order correction for the symmetric component contains projections onto $\mathcal{H}^{(4)}_q$ while the leading order correction for the anti-symmetric component projects onto $\mathcal{H}^{(3)}_q$.

The isotropic weights t_q featuring in Eq. (7) satisfy the lattice constraints[46]

$$2\sum_{q=1}^{Q_m/2} t_q\,c_\alpha c_\beta = \delta_{\alpha\beta}, \quad 6\sum_{q=1}^{Q_m/2} t_q\,c_\alpha c_\beta c_\gamma c_\delta = \delta_{\alpha\beta}\delta_{\gamma\delta} + \delta_{\alpha\gamma}\delta_{\beta\delta} + \delta_{\alpha\delta}\delta_{\beta\gamma}, \tag{10}$$

where $t_0 = 1$, $t_{1,\ldots,6} = 1/6$, and $t_{7,\ldots,18} = 1/12$ for the D3Q19 lattice, and $t_0 = 8/9$, $t_{1,\ldots,6} = 4/9$, $t_{7,\ldots,18} = 1/18$, and $t_{19,\ldots,26} = 1/72$ for the D3Q27 lattice. This definition of the weights t_q follows the TRT nomenclature[40,41,43] and is related to the standard weights w_q, popular in the LBM literature,[20–22] through the relationship $t_q = 3\,w_q$.

Given that the local force quantity $\vec{F}$ is put into the equilibrium, Eq. (7b), then the exact mass and momentum conservation equations are established as follows:[40–42,44]

$$\hat{n}_0(\vec{x},t) + 2\sum_{q=1}^{Q_m/2} \hat{n}^+_q(\vec{x},t) = 0, \quad 2\sum_{q=1}^{Q_m/2} \vec{c}_q\,\hat{n}^-_q(\vec{x},t) = \vec{F}(\vec{x},t). \tag{11}$$

The macroscopic quantities in Eq. (7) are determined via the moments of the symmetric/anti-symmetric populations $f^{\pm}_q$ as follows:

$$\rho = f_0 + 2\sum_{q=1}^{Q_m/2} f^+_q, \quad \vec{j} = \vec{J} + \frac{1}{2}\vec{F} \quad \text{where} \quad \vec{J} = 2\sum_{q=1}^{Q_m/2} \vec{c}_q f^-_q,$$
$$\vec{F} = 2\sum_{q=1}^{Q_m/2} \vec{c}_q\,F_q. \tag{12}$$

C. Rotating forces

The external force density F_α in Eq. (8d) includes two contributions:[9,11] (1) a constant force field, $\rho_0 a_\alpha$, representing gravity or a constant pressure gradient, and (2) a Coriolis force representing the non-inertial rotating frame, $-2\epsilon_{\alpha\beta\gamma}\Omega_\beta j_\gamma$, which rotates steadily at constant angular velocity $\vec{\Omega}$. Altogether, the content of F_α is given by

$$F_\alpha = \rho_0 a_\alpha - 2\epsilon_{\alpha\beta\gamma}\Omega_\beta j_\gamma, \tag{13}$$

where $\epsilon_{\alpha\beta\gamma}$ is the permutation tensor.

For the sake of convenience, the above vector quantities are expressed on the streamline-rotated coordinate system (x', y', z'). In this work, only rotations about two axes will be considered, but the extension to other orientations follows along similar lines. The streamline-rotated frame (x', y', z') relates to the fixed one (x, y, z) through the following transforms:

$$\begin{aligned} x' &= x\cos\theta + y\sin\theta\sin\alpha + z\sin\theta\cos\alpha, \\ y' &= y\cos\alpha - z\sin\alpha, \\ z' &= -x\sin\theta + y\cos\theta\sin\alpha + z\cos\theta\cos\alpha. \end{aligned} \tag{14}$$

The angle θ measures the rotation about the $y = y'$ axis and the angle α measures the rotation about the $x = x'$ axis, as sketched in Fig. 2. Recall, the rotated frame (x', y', z') is oriented to locally align with the $\vec{j}(\vec{x})$ flow field.

With the shift to operate on the (x', y', z') frame, one guarantees that the constant acceleration $\vec{a} = a_{x'}\,\vec{\imath}_{x'}$ and the constant angular velocity $\vec{\Omega} = \Omega_{z'}\,\vec{\imath}_{z'}$ (where $\Omega_{z'} > 0$ for a counterclockwise rotation)

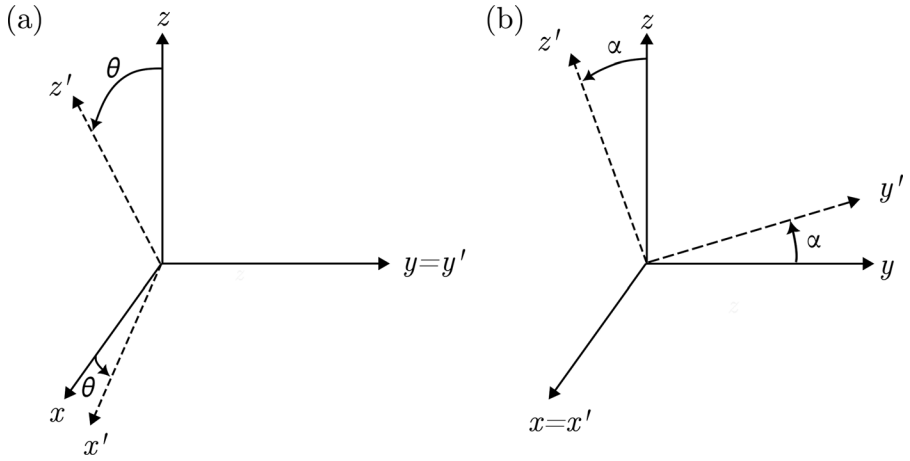

FIG. 2. Relation between fixed (x, y, z) and rotated (x', y', z') Cartesian axes. (a) Rotation about y axis by θ angle. (b) Rotation about x axis by α angle.

have projections on a single axis. As a result, each component of $\vec{F}$ in the (x', y', z') frame takes the simpler form

$$F_{x'} = \rho_0 a_{x'} + 2\,\Omega_{z'}\,j_{y'}, \quad F_{y'} = -2\,\Omega_{z'}\,j_{x'}, \quad F_{z'} = 0. \tag{15}$$

Finally, as $\vec{F}$ is momentum dependent, due to the Coriolis force, the determination of $\vec{j} = \vec{J} + \frac{1}{2}\vec{F}$ in Eq. (12) can be made explicit as follows:

$$\begin{aligned} j_{x'} &:= \rho_0\, u_{x'} = \frac{J_{x'} + \frac{1}{2}\rho_0 a_{x'} + J_{y'}\,\Omega_{z'}}{1 + \Omega_{z'}^2}, \\ j_{y'} &:= \rho_0\, u_{y'} = \frac{J_{y'} - \left(J_{x'} + \frac{1}{2}\rho_0 a_{x'}\right)\Omega_{z'}}{1 + \Omega_{z'}^2}, \\ j_{z'} &:= \rho_0\, u_{z'} = J_{z'}. \end{aligned} \tag{16}$$

D. Improved equilibrium (IE) for advection modeling in D3Q19

For the D3Q19 lattice, it is proposed to replace the quadratic velocity component of the standard NSE equilibrium by an improved formulation,[77–79] employing the transform $E_q \mapsto E_q^{(\star)}$. In practice, instead of considering E_q, given in Eq. (8b), the alternative expression for the quadratic velocity term is suggested

$$\begin{aligned} E_q^{(\star)} = t_q \frac{1}{\rho_0}\Bigg[& \frac{3}{2}\left(\mathcal{H}^{(2)}_{qxx} j_x^2 + \mathcal{H}^{(2)}_{qyy} j_y^2 + \mathcal{H}^{(2)}_{qzz} j_z^2\right) \\ & + 3\left(\mathcal{H}^{(2)}_{qxy} j_x j_y + \mathcal{H}^{(2)}_{qxz} j_x j_z + \mathcal{H}^{(2)}_{qyz} j_y j_z\right) \\ & + \frac{1}{3}\left(2\,\mathcal{H}^{(4o2)}_{qxxyy} + 2\,\mathcal{H}^{(4o2)}_{qxxzz} + 5\,\mathcal{H}^{(4o2)}_{qyyzz}\right) j_x^2 \\ & + \frac{1}{3}\left(2\,\mathcal{H}^{(4o2)}_{qxxyy} + 5\,\mathcal{H}^{(4o2)}_{qxxzz} + 2\,\mathcal{H}^{(4o2)}_{qyyzz}\right) j_y^2 \\ & + \frac{1}{3}\left(5\,\mathcal{H}^{(4o2)}_{qxxyy} + 2\,\mathcal{H}^{(4o2)}_{qxxzz} + 2\,\mathcal{H}^{(4o2)}_{qyyzz}\right) j_z^2\Bigg], \end{aligned} \tag{17}$$

where $\mathcal{H}^{(4o2)}_{qxxyy} = \mathcal{H}^{(4)}_{qxxyy} + \frac{1}{6}\mathcal{H}^{(2)}_{qzz}$, $\mathcal{H}^{(4o2)}_{qxxzz} = \mathcal{H}^{(4)}_{qxxzz} + \frac{1}{6}\mathcal{H}^{(2)}_{qyy}$, and $\mathcal{H}^{(4o2)}_{qyyzz} = \mathcal{H}^{(4)}_{qyyzz} + \frac{1}{6}\mathcal{H}^{(2)}_{qxx}$ are orthogonal bases that result from the orthogonalization of the fourth-order Hermite polynomials with respect to the second-order Hermite polynomials under the weighted scalar product.[79] The fourth-order Hermite polynomial is defined as follows:

$$\mathcal{H}^{(4)}_{q\alpha\alpha\beta\beta} = \left(c_{q\alpha}^2 - \frac{1}{3}\right)\left(c_{q\beta}^2 - \frac{1}{3}\right) = c_{q\alpha}^2 c_{q\beta}^2 - \frac{1}{3}\left(c_{q\alpha}^2 + c_{q\beta}^2\right) + \frac{1}{9}. \tag{18}$$

Remark 2.3. The improved equilibrium $E_q^{(\star)}$ in Eq. (17) is constructed by augmenting the standard non-linear equilibrium term, E_q, given in Eq. (8b), on the first and second lines of Eq. (17), with a supplementary correction that takes into account the additional projections of j_α^2 onto $\mathcal{H}^{(4o2)}_{q\alpha\alpha\beta\beta}$, described by the third, fourth and fifth lines of Eq. (17).

In order to understand the need for an improved representation of the equilibrium state in the D3Q19 model, as given by Eq. (17), it is convenient to reassess its original formulation. Differently from the original contributions, e.g., Qian *et al.*,[46] employing the Taylor expansion (up to velocity terms squared) of the continuous Maxwell–Boltzmann equilibrium, nowadays the standard second-order LBM equilibrium is typically derived through the Hermite expansion approach.[47,48] According to this methodology, the second-order discrete velocity equilibrium is obtained as a projection of the Maxwell–Boltzmann local equilibrium on the orthonormal basis spanned by the Hermite polynomials from zeroth up to the second order. Based on this Hermite projection procedure, it is possible to ensure that the moments of the discrete equilibrium match their continuous counterparts (up to the second order, in this case). However, this equivalence is only verified on the so-called complete velocity sets,[79] formed by the D1Q3 lattice and its tensor product-based extensions, the D2Q9 and the D3Q27 lattices.

In three-dimensional (3D), it is common to adopt cubic lattices with fewer than 27 discrete velocities, such as the D3Q15 and the D3Q19, as they offer higher computational efficiency.[20–22] Even though in these reduced cubic lattices the number of moments that are matched is smaller, it turns out that this number is less than the linearly independent moments available with the standard equilibrium, based on the second-order Hermite expansion, see Table I. The correction of this deficiency suggests a different equilibrium structure. Among the reduced cubic lattices, the D3Q19 lattice seems to be the only one qualified for this task since, unlike the D3Q15 lattice, the D3Q19 contains all the discrete velocities of the D2Q9 lattice in each of its 2D planes (x, y), (y, z), and (x, z), see Fig. 1. So, under the requirement that the discrete equilibrium of the D3Q19 lattice must preserve the same moments supported by the D2Q9 lattice on its three planes, it is possible to identify the 8 moments in excess and discard them.[79] The projection of the standard equilibrium, based on the second-order Hermite expansion, on the full set of the selected 19 admissible moments reveals a spurious coupling between hydrodynamic and high-order moments. This defect can be corrected with the inclusion of the $\mathcal{H}^{(4o2)}_{q\alpha\alpha\beta\beta}$ orthogonal basis in the original equilibrium, as shown in Eq. (17). With the discrete velocity equilibrium given by Eq. (17), all the 19 moments supported by the D3Q19 lattice now match their continuous Maxwellian counterpart, as indicated in Table I. This result holds regardless of the collision model adopted. In the TRT model, it has a cleaner appearance as it applies exclusively to the non-linear velocity term.

It is worth noticing that the particular structure of the discrete equilibrium for the NSE in the D3Q19 lattice, given by Eq. (17), was originally derived by Bauer *et al.*[77,78] based on a top-down approach to construct the discrete equilibrium under the requirement of isotropic macroscopic equations. This inverse-type methodology led to less comprehensible results at the end, although they could be expressed in a more compact presentation form, as summarized in Appendix B. Here, to derive Eq. (17) we opted to follow the theoretical framework put forward by Coreixas *et al.*[79] where the isotropy requirement is explicitly enforced at the level of the discrete equilibrium state. This bottom-up approach naturally leads to the isotropy of the recovered macroscopic equations. Nonetheless, we underline that the two methodologies, top-down and bottom-up, provide the same discrete equilibrium structure for the preservation of isotropy in the D3Q19 lattice. It is also worth noting the recent work by Taha *et al.*[80] that also proposed an $\mathcal{H}^{(4o2)}_{q\alpha\alpha\beta\beta}$ orthogonal basis correction on the j_α^2 terms of the original equilibrium in order to improve isotropy; however, a slightly different numerical pre-factor is identified in this work.[80]

TABLE I. Comparison between the moments of the continuous Maxwell–Boltzmann function and the non-aliased moments of the discrete equilibrium employed in D3Q19 and D3Q27 lattices. The D3Q27-SE equilibrium matches all 27 non-aliased moments. The D3Q19-IE equilibrium matches all 19 non-aliased moments. The D3Q19-SE equilibrium matches only 16 of the 19 non-aliased moments. It is highlighted in bold the differences with respect to the isothermal continuous Maxwellian $f^{(\mathrm{eq})}(\rho,\,u_\alpha)=\frac{\rho}{(2\pi c_s^2)^{3/2}}\exp\left[-\frac{(c_\alpha-u_\alpha)^2}{2c_s^2}\right]$. The equilibrium moments are computed as $\Pi^{(\mathrm{eq})}_{\alpha_1\alpha_2\ldots\alpha_n}=\int c_{\alpha_1}c_{\alpha_2}\ldots c_{\alpha_n}\left[f^{(\mathrm{eq})}(\rho,\,u_\alpha)-f^{(\mathrm{eq})}(\rho,\,0)\right]dc_{\alpha_1}dc_{\alpha_2}\ldots dc_{\alpha_n}$ where the following linearization $\rho\,u_\alpha\rightarrow\rho_0\,u_\alpha(=j_\alpha)$ is considered.[77] Taking the symmetric component of the discrete equilibrium function $E_q=e_q^+-P_q$ the equilibrium moments are computed as $\Pi^{(\mathrm{eq})^+}_{\alpha_1\alpha_2\ldots\alpha_n}=\sum c_{q\alpha_1}c_{q\alpha_2}\ldots c_{q\alpha_n}E_q$. Here, the index variables may not have the same value and repeating indices are not summed over. For example, the moment $\Pi^{(\mathrm{eq})^+}_{\alpha\alpha\beta\gamma}=\sum c_{q\alpha}c_{q\alpha}c_{q\beta}c_{q\gamma}E_q$ encompasses the velocity sets $c^2_{qx}c_{qy}c_{qz}$, $c^2_{qy}c_{qx}c_{qz}$, and $c^2_{qz}c_{qx}c_{qy}$. Odd-order moments are omitted from the analysis given that all non-aliased moments match their continuous Maxwellian counterpart. The information presented here is inspired by Bauer and Rüde work.[81]

Order	Moment	Maxwellian	D3Q19-SE	D3Q19-IE	D3Q27-SE
0	$\Pi^{(\mathrm{eq})^+}$	0	0	0	0
2	$\Pi^{(\mathrm{eq})^+}_{\alpha\alpha}$	j_α^2	j_α^2	j_α^2	j_α^2
2	$\Pi^{(\mathrm{eq})^+}_{\alpha\beta}$	$j_\alpha j_\beta$	$j_\alpha j_\beta$	$j_\alpha j_\beta$	$j_\alpha j_\beta$
4	$\Pi^{(\mathrm{eq})^+}_{\alpha\alpha\beta\beta}$	$\frac{1}{3}(j_\alpha^2+j_\beta^2)$	$\frac{1}{3}(j_\alpha^2+j_\beta^2)-\mathbf{\frac{1}{6}j_\gamma^2}$	$\frac{1}{3}(j_\alpha^2+j_\beta^2)$	$\frac{1}{3}(j_\alpha^2+j_\beta^2)$
4	$\Pi^{(\mathrm{eq})^+}_{\alpha\alpha\beta\gamma}$	$\frac{1}{3}j_\alpha j_\beta$	**0**	**0**	$\frac{1}{3}j_\alpha j_\beta$
6	$\Pi^{(\mathrm{eq})^+}_{\alpha\alpha\beta\beta\gamma\gamma}$	$\frac{1}{9}(j_\alpha^2+j_\beta^2+j_\gamma^2)$	**0**	**0**	$\frac{1}{9}(j_\alpha^2+j_\beta^2+j_\gamma^2)$

In terms of nomenclature, this work will denote by D3Q19-SE the D3Q19 model operating with the standard symmetric component of equilibrium (SE), given by Eq. (8b), whereas the use of the improved equilibrium (IE), given by Eq. (17), will be denoted by D3Q19-IE.

Remark 2.4. While for the purpose of theoretical analyses the form of $E_q^{(\star)}$ given by Eq. (17) is preferred, from the computational efficiency standpoint it is more suitable to work with the form of $E_q^{(\star)}$ given by Eq. (B2) in Appendix B. Indeed, Appendix B displays two efficient ways to compute the non-linear equilibrium term: the E_q form of the D3Q19-SE model given by Eq. (B1) and the $E_q^{(\star)}$ form of the D3Q19-IE model given by Eq. (B2). The two implementations require virtually the same number of operations. Hence, in practice, the D3Q19-IE model supports an improved isotropy with virtually no extra computational cost added.

E. Improved force (IF) model for diffusion modeling in D3Q19

The improved force (IF) strategy corrects the standard force (SF) formulation, i.e., $F_q\mapsto F_q^{(\star)}$, by including a high-order correction on the anti-symmetric source term. This correction was originally proposed by Ginzburg[44] under the name of "anisotropic force weights." For the D3Q19 lattice, the formulation of the IF scheme on the LBM source term reads

$$F_q^{(\star)}=t_q\left(\mathcal{H}^{(1)}_{q\alpha}+3\,k_\alpha\,\mathcal{H}^{(3)}_{q\alpha\beta\beta}\right)F_\alpha, \tag{19}$$

where the standard LBM source model, based on the first-order Hermite expansion, given by Eq. (8d), is augmented with a third-order Hermite polynomial correction, defined as follows:

$$\mathcal{H}^{(3)}_{q\alpha\beta\beta}=c_{q\alpha}\left(c^2_{q\beta}-\frac{1}{3}\right). \tag{20}$$

Here, $\mathcal{H}^{(3)}_{q\alpha\beta\beta}$ are mass- and momentum-conserving basis vectors[44] given that $\sum t_q\,\mathcal{H}^{(3)}_{q\alpha\beta\beta}=0$ and $\sum t_q\,\mathcal{H}^{(3)}_{q\alpha\beta\beta}c_{q\alpha}=0\;(\forall\,\alpha,\,\beta)$. The coefficients k_α in Eq. (19) are freely adjustable parameters. Their form is established under the requisite to cancel (or, at least, to mitigate) the artifacts coming from the force term discretization, i.e., they are problem specific. Below, specific k_α values are provided for the cases shown in Fig. 3; details about the derivations are given in Appendix C. Following the frame definitions introduced in Sec. II C, we adopt a coordinate system $(x',\,y',\,z')$ that locally aligns with the channel, which in turn may be arbitrarily rotated with respect to the fixed $(x,\,y,\,z)$ coordinate system, see Fig. 3.

- *Horizontal channel.* The flow is aligned with the (x,y) plane according to Fig. 3(a). In this configuration, Eq. (19) becomes

$$F_q^{(\star)}=t_q\left[\left(\mathcal{H}^{(1)}_{qx}+3\,k_x\,\mathcal{H}^{(3)}_{qxzz}\right)F_x+\left(\mathcal{H}^{(1)}_{qy}+3\,k_x\,\mathcal{H}^{(3)}_{qyzz}\right)F_y\right], \tag{21}$$

and the exact removal of the force artifacts is achieved with

$$k_x=k_y=1-\frac{3}{8\Lambda}. \tag{22}$$

- *Diagonal channel.* The flow is rotated the angles $\alpha=\theta=\pi/4$ around the x and y axes, respectively; see Fig. 3(b) with $\alpha=\theta=\pi/4$. In this configuration, Eq. (19) becomes

$$F_q^{(\star)}=t_q\left[\left(\mathcal{H}^{(1)}_{qx'}+3\,k_{x'}\,\mathcal{H}^{(3)}_{qx'z'z'}\right)F_{x'}+\left(\mathcal{H}^{(1)}_{qy'}+3\,k_{y'}\,\mathcal{H}^{(3)}_{qy'z'z'}\right)F_{y'}\right], \tag{23}$$

where $\mathcal{H}^{(3)}_{qx'z'z'}=c_{qx'}\left(c^2_{qz'}-\frac{1}{3}\right)$ and $\mathcal{H}^{(3)}_{qy'z'z'}=c_{qy'}\left(c^2_{qz'}-\frac{1}{3}\right)$ in which (x',y',z') is defined by Eq. (14), and the exact removal of the force artifacts is achieved with

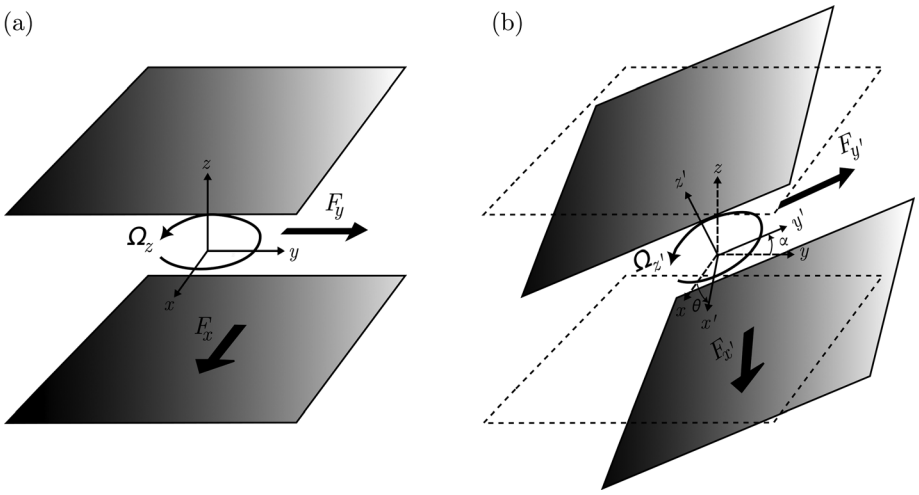

FIG. 3. Force-driven flow between two parallel walls in a channel setup. (a) Horizontal channel with $\alpha = \theta = 0$. (b) Arbitrarily inclined channel with $\alpha \neq 0$ and $\theta \neq 0$.

$$k_{x'} = k_{y'} = 1 - \frac{3}{4\Lambda}. \tag{24}$$

- *Inclined channel.* The flow is rotated an arbitrary angle $\theta \in [0, \pi/2]$ around the y axis and an arbitrary angle $\alpha \in [0, \pi/2]$ around x axis; see Fig. 3(b) with α and θ arbitrary, and the coordinate system (x', y', z'), defined by Eq. (14), is adopted herein. Under this configuration, Eq. (19) is also represented by Eq. (23), but the removal of the force artifacts is now only achieved in approximate form through

$$\begin{aligned} k_{x'} &= 1 - \frac{3\,\gamma_{x'}(\theta)}{4\Lambda(3\,\gamma_{x'}(\theta) - 1)}, \\ k_{y'} &= 1 - \frac{3\,\gamma_{y'}(\alpha)}{4\Lambda(3\,\gamma_{y'}(\alpha) - 1)}, \end{aligned} \tag{25}$$

where $\gamma_{x'}(\theta)$ and $\gamma_{y'}(\alpha)$ measure the (angular-dependent) sixth-order velocity moments given by

$$\begin{aligned} \gamma_{x'}(\theta) &= 6\sum_{q=1}^{Q_m/2} t_q\, c_{qx'}^2 c_{qz'}^4 = \frac{1}{4}(3 + \cos(4\theta)), \\ \gamma_{y'}(\alpha) &= 6\sum_{q=1}^{Q_m/2} t_q\, c_{qy'}^2 c_{qz'}^4 = \frac{1}{4}(3 + \cos(4\alpha)). \end{aligned} \tag{26}$$

Remark 2.5. The improved force (IF) strategy, compared to the SF scheme, is more prone to stability issues when Λ is small. A heuristic stability argument[54] reveals that, for a horizontal channel, the overall coefficient weighing the forcing term obtains a negative pre-factor when $\Lambda < \frac{1}{4}$, i.e., $t_q\, c_{qx}(1 + 2k_x)|_{k_x = 1 - \frac{3}{8\Lambda}} = 3\, t_q\, c_{qx}\left(1 - \frac{1}{4\Lambda}\right)$, which might explain why the use of small Λ values might lead to instabilities. Still, numerical evidence has indicated that, for this problem class, stability can be maintained within the typical range $\Lambda \in [\frac{1}{12}, 1]$, providing the numerical parameters of the simulation are carefully tuned. In terms of extra computational overhead, the IF strategy only brings one extra term compared to the original SF scheme. Additionally, this extra term is a constant pre-factor. As such, it can be computed only once, during the initialization stage of the computational algorithm. In practice, the computational cost of the IF scheme becomes virtually identical to the SF scheme.

To conclude this section, it is noted that an analysis of the very popular Guo forcing strategy,[26] which includes non-zero symmetric components on the second-order Hermite basis $\mathcal{H}_q^{(2)}$, is presented in Appendix A. This analysis reveals the inadequacy of Guo's model[26] to incorporate the Coriolis force term, a conclusion in line with other studies[49–52] considering the LBM modeling of a variety of steady fluid flows driven by other kinds of body forces. In any case, if we would like to extend the IF idea to Guo's model[26] then, according to the explanation given in Remark 2.2, two independent corrections would be necessary: one projected onto $\mathcal{H}_q^{(3)}$, which acts upon $\vec{F}$, and another projected onto $\mathcal{H}_q^{(4)}$, which acts upon $\vec{j}\vec{F}$.

F. Boundary schemes

In this section, two types of LBM boundary schemes are presented. Section II F 1 describes an (on-node) wet node boundary scheme. Section II F 2 revises existing and proposes new (off-node) linkwise boundary schemes. Both families of boundary schemes will be extensively used throughout this work.

1. Wet node boundary schemes (on-node)

The wet node formulation enforces the prescribed macroscopic boundary condition, $\vec{u}(\vec{x}_b) = \vec{u}(\vec{x}_w) = \vec{0}$, into the LBM boundary populations. Under this framework, we follow a simplified version of the local second-order boundary (LSOB) scheme.[63,64] The formulation employed here is restricted to straight on-lattice walls, where $\vec{x}_b = \vec{x}_w$. However, we underline the wet node formulation,[68–70] and LSOB[63,64] in particular, can be generalized to accommodate arbitrary shaped walls, although this task is beyond the scope of the present work. For this task, off-lattice walls will be modeled with linkwise schemes, as will be discussed in Sec. II F 2.

The general LSOB method enforces the intended macroscopic BCs by explicitly reconstructing the unknown incoming boundary populations according to the TRT decomposition[64]

$$f_{\bar{q}}(\vec{x}_b, t+1) = \left[e_{\bar{q}}^{+} + e_{\bar{q}}^{-} - \tau^{+}\hat{n}_{\bar{q}}^{+} - \tau^{-}\hat{n}_{\bar{q}}^{-}\right]_{(\vec{x}_b, t)}, \tag{27}$$

where $\vec{c}_{\overline{q}} = -\vec{c}_q$ and $\hat{n}_q^{\pm} = -\frac{1}{\tau^{\pm}}(f_q^{\pm} - e_q^{\pm})$. The overbar notation $\overline{q}$ denotes populations coming from outside the fluid domain, meaning they belong to the set of unknown populations, i.e., $\mathcal{U} = \{\overline{q} \,|\, f_{\overline{q}} \text{ is unknown}\}$. The transcription of Eq. (27) toward our problem specification, further subject to on-node no-slip walls, leads to

$$f_{\overline{q}}(\vec{x}_b, t+1) = t_q P(\vec{x}_b, t) + t_q \vec{c}_{\overline{q}} \cdot \left(\rho_0 \underbrace{\vec{u}(\vec{x}_b, t)}_{=\vec{u}(\vec{x}_w)=\vec{0}} + \Lambda^- \left(1 + 3k_x\left(c_{qz}^2 - \frac{1}{3}\right)\right) \underbrace{\vec{F}(\vec{x}_b, t)}_{=\rho_0 a_x \vec{i}_x} \right) - \tau^+ \hat{n}_{\overline{q}}^+(\vec{x}_b, t) - \tau^- \hat{n}_{\overline{q}}^-(\vec{x}_b, t). \quad (28)$$

The simplification of Eq. (28) leads to the wet node boundary scheme used in practice

$$f_{\overline{q}}(\vec{x}_b, t+1) = t_q P(\vec{x}_b, t) + \Lambda^- t_q c_{\overline{q}x}\left(1 + 3k_x\left(c_{qz}^2 - \frac{1}{3}\right)\right)\rho_0 a_x - \tau^+ \hat{n}_{\overline{q}}^+(\vec{x}_b, t) - \tau^- \hat{n}_{\overline{q}}^-(\vec{x}_b, t). \quad (29)$$

Finally, pressure in Eq. (28) is available locally, for example, by exploiting existing algorithms.[63,67,84] Here, the algorithm employed is based on the zeroth-order mass moment $\frac{P}{c_s^2} = \sum_{q\in\mathcal{K}} f_q + \sum_{\overline{q}\in\mathcal{U}} f_{\overline{q}}$ at $\vec{x}_b$, in which the f_q populations belonging to the unknown set $\mathcal{U}$ are replaced by their LSOB reconstruction, Eq. (28), where $\mathcal{K} = \{q \,|\, f_q \text{is known}\}$ and $\mathcal{U} = \{\overline{q} \,|\, f_{\overline{q}} \text{ is unknown}\}$; in this way, the pressure at the boundary node is determined as follows:[63]

$$P(\vec{x}_b, t) = \frac{1}{c_s^{-2} - \sum_{\overline{q}\in\mathcal{U}} t_{\overline{q}}} \Bigg[\sum_{\overline{q}\in\mathcal{K}} f_q(\vec{x}_b, t) + \rho_0 \underbrace{\vec{u}(\vec{x}_b, t)}_{=\vec{u}(\vec{x}_w)=\vec{0}} \cdot \sum_{\overline{q}\in\mathcal{U}} t_{\overline{q}} c_{\overline{q}x} + \Lambda^- \rho_0 a_x \sum_{\overline{q}\in\mathcal{U}} t_{\overline{q}} c_{\overline{q}x}\left(1 + 3k_x\left(c_{qz}^2 - \frac{1}{3}\right)\right) - \tau^+ \sum_{\overline{q}\in\mathcal{U}} \hat{n}_{\overline{q}}^+(\vec{x}_b, t) - \tau^- \sum_{\overline{q}\in\mathcal{U}} \hat{n}_{\overline{q}}^-(\vec{x}_b, t) \Bigg]. \quad (30)$$

We note that the LSOB scheme is local and explicit since the non-equilibrium populations $\hat{n}_q^{\pm}(\vec{x}_b, t)$ are always available, a condition that follows from the TRT symmetry property: $\hat{n}_q^+ = \hat{n}_{\overline{q}}^+$ and $\hat{n}_q^- = -\hat{n}_{\overline{q}}^-$; the same condition applies to the weights $t_{\overline{q}} = t_q$.

2. Linkwise boundary schemes (off-node)

Within the linkwise formulation, boundary conditions are operated on the boundary nodes $\vec{x}_b$, whose location is typically shifted from the wall placement $\vec{x}_w$ as follows $\vec{x}_b = \vec{x}_w + \delta_q \vec{c}_q$, where $\vec{c}_q$ represents a wall cut link and δ_q the wall-boundary node distance measured along the considered wall cut link. Due to their operation principle, the modeling of off-node walls is naturally covered. Here, two types of linkwise formulations are considered as no-slip boundary condition models. They are summarized next.

- The bounce-back (BB) rule,[21,43,45,58–62] which determines the populations streaming in from $\vec{x}_b$ by their mirrored state from the post-collision step at $\vec{x}_b$, given as follows:

$$f_{\overline{q}}(\vec{x}_b, t+1) = \hat{f}_q(\vec{x}_b, t) - 2 j_q(\vec{x}_w), \quad (31)$$

with $\vec{x}_b + \vec{c}_q \in$ solid. The last term in Eq. (31) is a Dirichlet correction accounting for the (time-independent in our particular context) wall movement $\vec{u}_w$, given by $j_q(\vec{x}_w) = t_q \rho_0 \vec{c}_q \cdot \vec{u}_w$. For a resting wall, the $j_q(\vec{x}_w)$ correction in Eq. (31) vanishes because $\vec{u}_w = \vec{0}$.

- The modified linear interpolation (MLI) rule[41,45,56,62] specifies the streaming in populations coming from $\vec{x}_b$ according to the following generic reflection rule:

$$f_{\overline{q}}(\vec{x}_b, t+1) = \kappa_1 \hat{f}_q(\vec{x}_b, t) + \overline{\kappa}_{-1} \hat{f}_{\overline{q}}(\vec{x}_b, t) + \kappa_0 f_q(\vec{x}_b, t+1) + F_q^{p.c.}(\vec{x}_b, t) - \alpha^{(u)} j_q(\vec{x}_w), \quad (32)$$

with $\vec{x}_b + \vec{c}_q \in$ solid. The last term in Eq. (32) is once again a Dirichlet boundary correction, given by $j_q(\vec{x}_w) = t_q \rho_0 \vec{c}_q \cdot \vec{u}_w$, which accounts for the wall movement $\vec{u}_w$. Equation (32) contains several adjustable parameters, which permit establishing different classes of linkwise boundary schemes, ranging from the simplest and low-order accurate BB scheme to the more complex and high-order (parabolic) accurate MLI schemes. The MLI family of schemes comprises the central (MCLI), the upwind (MULI), or the downwind (MDLI) interpolation schemes, see Table II. They all share an identical formal order of accuracy but might exhibit different numerical characteristics in terms of stability; more details on the characteristics of the MLI schemes can be found in the works.[41,45,56,61,62] The detailed derivation of the MLI terms and coefficients for this problem class is presented in Appendix D. The $F_q^{p.c.}$ term is a post-collision (non-local) correction, designed to recover the parabolic accuracy, and is explicitly given as follows:

$$F_q^{p.c.} = \alpha^{(u)} \Lambda^- (\hat{n}_q^- - F_q^{(\star)}) + (1 - \kappa_1)\hat{n}_q^- - \alpha^{(u)} j_q(\vec{x}_w) + \alpha^{(u)} \delta_q \frac{\overline{\delta\nu}_\alpha^{(2)}}{2\,\Omega_{z'}} \overline{\Delta}_q F_q|^{f.d.} + \alpha^{(u)} \frac{\delta_q^2}{2} \overline{\Delta}_q^2 j_q|^{f.d.}, \quad (33)$$

TABLE II. Parameters featuring in Eq. (32) for the different classes of linkwise boundary schemes within the MLI family.[41,45,56] While all schemes within the MLI family share the same formal accuracy, i.e., parabolic accuracy, they have a different stability behavior. As shown in the work,[61] the MCLI is expected to have a more limited stability behavior than the MULI and MDLI schemes.

		MLI family		
	BB	MCLI	MULI	MDLI
κ_1	1	1	$2\,\delta_q$	$\frac{1}{2\,\delta_q}$
κ_0	0	$\frac{1 - 2\,\delta_q}{1 + 2\,\delta_q}$	$1 - \kappa_1$	0
$\overline{\kappa}_{-1}$	0	$-\kappa_0$	0	$1 - \kappa_1$
$\alpha^{(u)}$	2	$\frac{4}{1 + 2\,\delta_q}$	2	$\frac{1}{\delta_q}$
$F_q^{p.c.}$	0		Eq. (33)	
δ_q	$\frac{1}{2}$	$]0, 1]$	$\left]0, \frac{1}{2}\right]$	$\left[\frac{1}{2}, 1\right]$

where $\overline{\delta\nu}_{\alpha}^{(2)}$ is a viscosity correction term given by $\overline{\delta\nu}$ for horizontal flow, see Eq. (43), or by $(\overline{\delta\nu}_{x'}^{(2)}, \overline{\delta\nu}_{y'}^{(2)}, 0)$ for arbitrary oriented flows, see Eq. (C10), whose components are subject to the inner product with $(F_{x'}, F_{y'}, 0)$ in Eq. (33). The last two terms in Eq. (33) can be determined by linkwise second-order finite-difference formulas. The discrete Laplacian term $\overline{\Delta}_q^2 j_q|^{f.d.}$ in Eq. (33) is evaluated as

$$\overline{\Delta}_q^2 j_q\Big|^{f.d.} = \frac{2}{(\delta_q + \delta_{\overline{q}})}\left(\frac{j_q(\vec{x}_{\rm w}) - j_q(\vec{x}_{\rm b})}{\delta_q} - \frac{j_q(\vec{x}_{\rm b}) - j_q(\vec{x}_{\overline{\rm w}})}{\delta_{\overline{q}}}\right), \quad (34)$$

and the discrete gradient term $\overline{\Delta}_q F_q|^{f.d.}$ in Eq. (33) is computed as

$$\overline{\Delta}_q F_q\Big|^{f.d.} = \frac{1}{(\delta_q + \delta_{\overline{q}})}\left(\frac{\delta_{\overline{q}}}{\delta_q}\big(F_q(\vec{x}_{\rm w}) - F_q(\vec{x}_{\rm b})\big) + \frac{\delta_q}{\delta_{\overline{q}}}\big(F_q(\vec{x}_{\rm b}) - F_q(\vec{x}_{\overline{\rm w}})\big)\right), \quad (35)$$

where $\vec{x}_{\rm w} = \vec{x}_{\rm b} + \delta_q \vec{c}_q$, $\vec{x}_{\overline{\rm w}} = \vec{x}_{\rm b} + \delta_{\overline{q}} \vec{c}_{\overline{q}}$, $\delta_q \neq 0$, and $\delta_{\overline{q}} \neq 0$. In this notation, if $\vec{x}_{\rm w}$ denotes a solid node with wall velocity $\vec{u}(\vec{x}_{\rm w})$ (or simply $\vec{0}$ for a resting wall), then $\vec{x}_{\overline{\rm w}}$ denotes a fluid node with $\delta_{\overline{q}} = 1$ and $\vec{u}(\vec{x}_{\overline{\rm w}})$ is extracted from the LBM bulk solution. In Eq. (34) the term j_q is given by Eq. (8c) and in Eq. (35) the term F_q is given by Eq. (8d) for the SF source model or by Eq. (19) for the IF source model.

III. POISEUILLE–EKMAN ROTATING CHANNEL FLOW: IMPROVED DIFFUSION MODELING

To understand the role of the force discretization and the boundary scheme on the LBM modeling of a rotating channel flow, a pure viscous problem will be considered. In this way, the effect of these two elements can be isolated, without the interference of the non-linear advection term, which will be considered ahead.

A. Theoretical formulation

Consider the 3D channel sketched in Fig. 4. The geometry consists of two parallel infinite walls at rest and located at $z = -H/2$ and $z = H/2$. The channel undergoes rotation about an axis perpendicular to its own axis with steady constant angular velocity $\vec{\Omega} = \Omega_z \vec{\imath}_z$, where $\Omega_z > 0$. Inside the channel an incompressible fluid flows with velocity field $\vec{u} = u_x \vec{\imath}_x + u_y \vec{\imath}_y$, subject to an external body force $\vec{F}$ given by Eq. (15). The flow is stationary $\frac{\partial \vec{u}}{\partial t} = 0$ and invariant along both streamwise $\frac{\partial \vec{u}}{\partial x} = 0$ and spanwise $\frac{\partial \vec{u}}{\partial y} = 0$ directions. Hence, the only flow variation happens along the z axis. Under these general considerations, the incompressible NSE in a rotating frame, Eqs. (1), leads to the following differential equations system, known as the Ekman–Poiseuille equations,[14] given by

$$a_x + 2\,\Omega_z\, u_y + \nu \frac{{\rm d}^2 u_x}{{\rm d}z^2} = 0, \quad (36a)$$

$$-2\,\Omega_z\, u_x + \nu \frac{{\rm d}^2 u_y}{{\rm d}z^2} = 0, \quad (36b)$$

and are subject to the no-slip boundary conditions $u_x(z = \pm H/2) = 0$ and $u_y(z = \pm H/2) = 0$.

To facilitate the problem solving, let us introduce the complex velocity

$$\phi = u_x + i\,u_y, \quad (37)$$

where $i = \sqrt{-1}$. Based on this new variable, Eqs. (36) reduce to the single equation

$$a_x - 2\,\Omega_z i\,\phi + \nu \frac{{\rm d}^2 \phi}{{\rm d}z^2} = 0, \quad (38)$$

with boundary conditions $\phi(z = \pm H/2) = 0$. The ϕ solution yields

$$\phi(\overline{z}) = -\frac{i\,a_x}{2\,\Omega_z}\left[1 - \frac{\cosh((1+i)\,\omega\,\overline{z})}{\cosh\left((1+i)\,\frac{\omega}{2}\right)}\right] \text{ with } \omega^2 = \frac{\Omega_z H^2}{\nu}$$
$$\text{and } \overline{z} = \frac{z}{H} \in \left[-\frac{1}{2}, \frac{1}{2}\right]. \quad (39)$$

The parameter ω is an important dimensionless group determining the problem dynamical regime based on the system rotation, and it relates to the inverse of the Ekman number, Ek, defined ahead in Eq. (62). Working out Eq. (39), the streamwise $u_x = {\rm Re}[\phi]$ and spanwise $u_y = {\rm Im}[\phi]$ velocity components are explicitly given as:

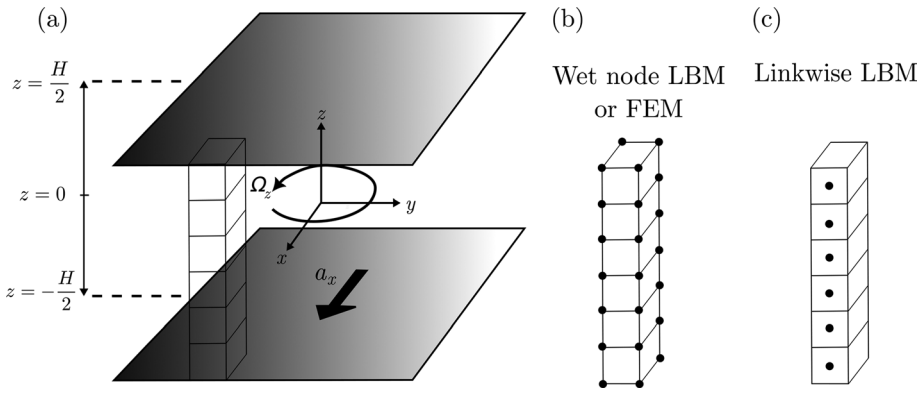

FIG. 4. Poiseuille–Ekman rotating channel flow. (a) Geometry and relevant parameters. (b) Computational cells according to wet node boundary discretization or cell vertex FEM discretization (vertex-centered discretization). (c) Computational cells according to linkwise boundary discretization (cell-centered discretization).

$$u_x(\overline{z}) = \frac{a_x}{\Omega_z}\left(\frac{\cos(\omega\overline{z})\cosh(\omega\overline{z})\sin\left(\frac{\omega}{2}\right)\sinh\left(\frac{\omega}{2}\right) - \sin(\omega\overline{z})\sinh(\omega\overline{z})\cos\left(\frac{\omega}{2}\right)\cosh\left(\frac{\omega}{2}\right)}{\cos(\omega)+\cosh(\omega)}\right), \tag{40a}$$

$$u_y(\overline{z}) = -\frac{a_x}{\Omega_z}\left(\frac{1}{2} - \frac{\cos(\omega\overline{z})\cosh(\omega\overline{z})\cos\left(\frac{\omega}{2}\right)\cosh\left(\frac{\omega}{2}\right) + \sin(\omega\overline{z})\sinh(\omega\overline{z})\sin\left(\frac{\omega}{2}\right)\sinh\left(\frac{\omega}{2}\right)}{\cos(\omega)+\cosh(\omega)}\right). \tag{40b}$$

The self-consistency of Eqs. (40) is verified through the recovery of the well-established Poiseuille flow solutions[14] in the non-rotating limit, that is, $\lim_{\omega\to 0} u_x(\overline{z}) = \frac{a_x H^2}{8\nu}(1-4\overline{z}^2)$ and $\lim_{\omega\to 0} u_y(\overline{z}) = 0$.

Based on the rotation parameter ω, the Poiseuille–Ekman flow solutions, given by Eqs. (40), may undergo three distinct dynamical regimes. Figure 5 sketches the domain of definition of each rotating flow regime in terms of the ω value. A summary of the corresponding flow topologies will be discussed next.

At small ω the flow lies in the *diffusion-dominated* regime, see Figs. 6(a) and 6(d). Here, the flow presents a quasi-parabolic profile in both directions, although possessing a higher velocity magnitude in the streamwise flow direction u_x. The diffusion-dominated regime is abandoned when u_x and u_y reach the same magnitude, i.e., when ω is such that $|u_x| = |u_y|$. This condition is met at $\omega = 2.163596505058589$.

The intermediate $\omega \approx 2.16$ value sets the beginning of the *Coriolis-dominated* regime, see Figs. 6(b) and 6(e). Here, the spanwise velocity profile u_y continues to develop in a parabolic-type fashion, although decreasing its magnitude, whereas the streamwise profile u_x becomes flatter in the central region. This topological change indicates

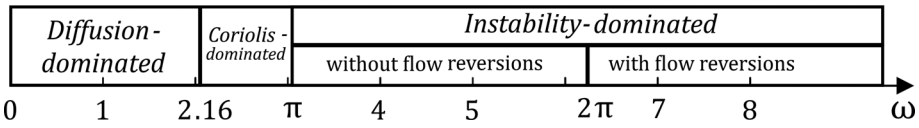

FIG. 5. Domain of each flow dynamical regime as function of the rotation parameter $\omega = \sqrt{\frac{\Omega_z H^2}{\nu}}$.

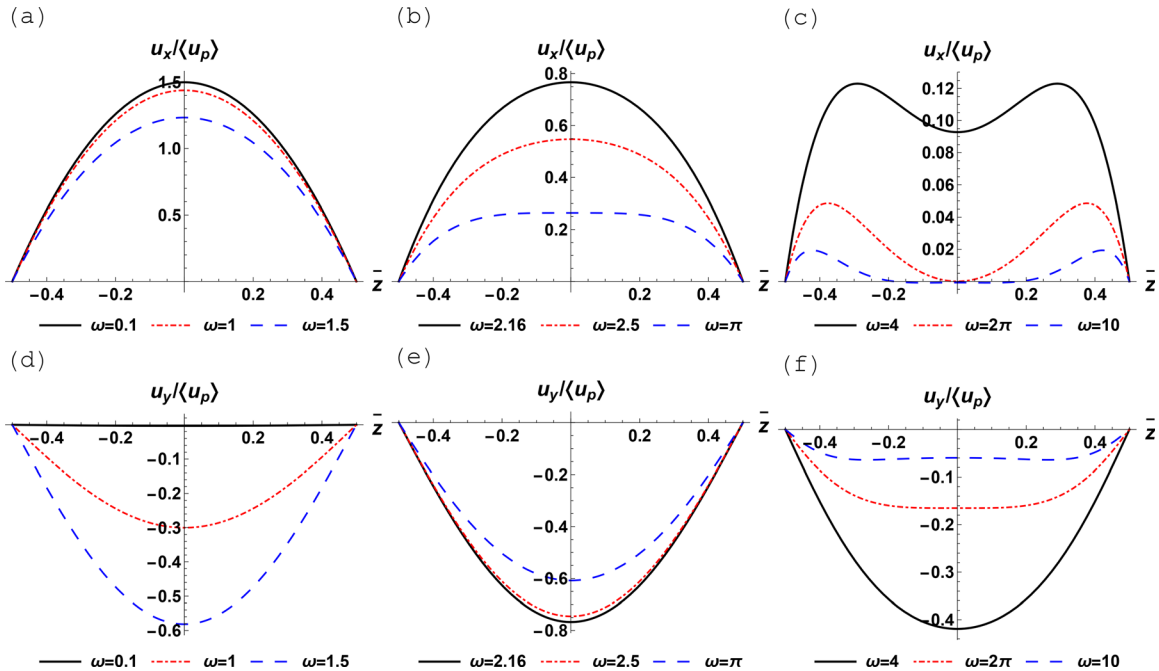

FIG. 6. Normalized velocity profiles for various rotation regimes $\omega = \sqrt{\frac{\Omega_z H^2}{\nu}}$, with $\Omega_z > 0$. The normalization velocity scale is $\langle u_p\rangle = \frac{a_x H^2}{12\nu}$, i.e., the non-rotating (Poiseuille) mean velocity. Panels (a) and (d) Diffusion-dominated regime. Panels (b) and (e) Coriolis-dominated regime. Panels (c) and (f) Instability-dominated regime.

that the Coriolis force has reached a competing magnitude compared to the constant acceleration a_x in the channel central region. Alongside this phenomenon, the viscous effects become confined to an increasingly thinner boundary layer next to the walls.

The value $\omega = \pi$ sets the transition to the *instability-dominated* regime, see Figs. 6(c) and 6(f). This regime is characterized by the appearance of inflection points in the velocity profile that result from the accumulation of the flow kinetic energy in the balance between the Coriolis force retarding effect at the channel center and the viscous boundary layer at the wall region. Progressively increasing the rotation rates makes the size of the boundary layers reduce even further, together with the widening of the geostrophic-like profile at the core region. At $\omega = 2\pi$ the streamwise velocity u_x decreases to $u_x = 0$ at the channel center region $\overline{z} = 0$. From this point onwards, i.e., $\omega > 2\pi$, the u_x profile develops oscillations around the aforementioned zero velocity state. At the same time, the inflection points continue to move closer to the walls. In contrast, the u_y evolution stays roughly insensitive to this behavior. The u_y magnitude decreases with ω and, like the u_x case, the u_y core region also tends to a geostrophic-like structure. Yet, unlike the u_x profile, the u_y component never experiences flow reversions.

B. Lattice Boltzmann formulation—horizontal channel flow

This section focuses on the LBM discrete solution of the problem previously introduced in Sec. III A. The presentation is split into three subsections. Section III B 1 derives the exact difference equations satisfied by the TRT scheme in bulk. While in bulk the same equations are obtained with vertex- or cell-centered discretizations, see sketches in Fig. 4, they will differ depending on how we treat the boundaries. Section III B 2 provides the solution of the problem using wet node boundaries, i.e., where the grid points of the cell coincide with the boundary location, so-called vertex-centered discretization, see Fig. 4(b). Section III B 3 derives the same solution for linkwise boundaries, i.e., where the extremities of the cell, which are not grid points, coincide with the boundary location, so-called cell-centered discretization, see Fig. 4(c).

1. Bulk formulation

Here, we cover the discrete formulation of the problem presented in Sec. III A, focused on bulk. Since fluid advection is not relevant in this particular setup, the non-linear velocity terms will be omitted from the numerical analysis; the validity of this simplification is limited to straight geometries, as demonstrated in the works.[44,61]

The discretization process sets the grid nodes z_j within computational cells differently depending on whether a wet node or a linkwise boundary condition is applied, see Figs. 4(b) and 4(c). In both instances, macroscopic velocities at the discrete level are represented as $\mathrm{u}_j := u_x(z_j)$ and $\mathrm{v}_j := u_y(z_j)$ along streamwise and spanwise directions, respectively.

Based on the adopted discretization, the LBM equations can be exactly solved by following the procedures developed by He *et al.*[60] or by Ginzburg.[44] This work adopts the latter, which is summarized in Appendix C. By doing so, it can be proven that the discrete system satisfied by the LBM equations, applied to the problem governed by Eqs. (36), is given by

$$a_x + 2\,\Omega_z\,\mathrm{v}_j + \nu\,\overline{\Delta}_z^2\mathrm{u}_j = \nu\,\overline{\delta\nu}\,\overline{\Delta}_z^2\mathrm{v}_j, \tag{41a}$$

$$-2\,\Omega_z\,\mathrm{u}_j + \nu\,\overline{\Delta}_z^2\mathrm{v}_j = -\nu\,\overline{\delta\nu}\,\overline{\Delta}_z^2\mathrm{u}_j. \tag{41b}$$

For notation convenience, above we have introduced the central difference operators for the discrete Laplacian of streamwise and spanwise velocities (using simulation units $\Delta x = 1$), which read as follows:

$$\overline{\Delta}_z^2\mathrm{u}_j = \mathrm{u}_{j+1} - 2\,\mathrm{u}_j + \mathrm{u}_{j-1} \quad \text{and} \quad \overline{\Delta}_z^2\mathrm{v}_j = \mathrm{v}_{j+1} - 2\,\mathrm{v}_j + \mathrm{v}_{j-1}. \tag{42}$$

Here, the fluid viscosity ν is given by Eq. (4) and the right-hand side terms in Eqs. (41) feature a viscosity correction $\overline{\delta\nu}$, which is a numerical artifact coming from the source term discretization that is explicitly determined as follows:

$$\overline{\delta\nu} = \left(\frac{8\Lambda - 3}{12}\right) T \quad \text{with} \quad T = \frac{2\,\Omega_z}{\nu}. \tag{43}$$

Alternatively, $\overline{\delta\nu}$ can be expressed as follows:

$$\overline{\delta\nu} = \left(\frac{8\Lambda - 3}{12}\right) \frac{2\,\omega^2}{H^2}. \tag{44}$$

By repeating the solution procedure of Sec. III A, the introduction of the complex discrete variable $\phi_j = \mathrm{u}_j + i\,\mathrm{v}_j$ permits merging Eqs. (41a) and (41b) into a single discrete equation

$$a_x - 2\,\Omega_z\,i\,\phi_j + \nu_e\,\overline{\Delta}_z^2\phi_j = 0 \quad \text{with} \quad \nu_e = \nu\,(1 + i\,\overline{\delta\nu}). \tag{45}$$

a. Analysis of bulk formulation. The comparison between the continuous formulation, Eqs. (36), and its LBM discrete counterpart, Eqs. (41), reveals the following two main differences.

First, the differential Laplacian terms are replaced by second-order central finite-difference approximations, respectively, $\frac{\mathrm{d}^2 u_x}{\mathrm{d}z^2} \to \overline{\Delta}_z^2\mathrm{u}_j$ and $\frac{\mathrm{d}^2 u_y}{\mathrm{d}z^2} \to \overline{\Delta}_z^2\mathrm{v}_j$. Considering the continuous solutions $\{u_x, u_y\}$ are characterized by transcendental-type functions, see Eqs. (40), their discrete counterparts make unavoidable the presence of $\mathcal{O}(\epsilon^2)$ discretization errors, where $\epsilon = 1/H$.

Second, the right-hand sides of Eqs. (41) feature spurious discrete velocity Laplacian terms, created by the non-local discretization of the (velocity-dependent) Coriolis body force, and display as coefficients the viscosity correction $\overline{\delta\nu}$ term. Looking at Eq. (44), the artifact $\overline{\delta\nu}$ depends on three factors:[44]

(i) the physical flow regime, determined by the square of ω, which perturbs $\overline{\delta\nu}$ linearly, and vanishes in the no-rotation limit $\omega \to 0$;
(ii) the inverse square of the mesh size $\overline{\delta\nu} \propto 1/H^2$, where H counts the grid nodes number;
(iii) the relaxation parameter of the TRT collision scheme, which sets $\overline{\delta\nu} = 0$ for $\Lambda = 3/8$.

Remark 3.1. If considering the single-relaxation-time BGK scheme[46] to solve this problem, then the numerical artifact $\overline{\delta\nu}$ leads to a non-linear viscosity dependence[44] in the solution structure, i.e., $\overline{\delta\nu} \propto (\tau - \frac{1}{2})^2 \propto 9\nu^2$. In this way, when the mesh size H is fixed, then the BGK solutions are no longer controlled by ω alone, as it would be required by the principle of dimensional similitude, but they will vary depending on the ν individual value. The TRT scheme is exempt from

this defect since Λ is a pure numerical parameter that does not enter the construction of the physical dimensionless groups, contrary to ν. This explains why the BGK must be considered an *inconsistent* numerical scheme.

Remark 3.2. In addition to the aforementioned dependencies, it is also important to recall that the structure of $\overline{\delta\nu}$ is anisotropic. While Eq. (43) has been derived considering the flow is aligned with the lattice's main links, if we would repeat this derivation, but now consider the flow aligned with the lattice's diagonal links[44] then Eq. (43) would become $\overline{\delta\nu} = \left(\frac{4\Lambda-3}{24}\right) T$. In general, the $\overline{\delta\nu}$ angular dependence[44] can be vanished for $\Lambda = \frac{1}{4}$. Yet, this relaxation choice does not eliminate the $\overline{\delta\nu}$ numerical artifact, but fixes it to $\overline{\delta\nu} = -\frac{1}{12}\, T$.

Remark 3.3. The $\overline{\delta\nu}$ numerical artifact is inherent to the LBM approximation, and it has been identified in other LBM problems featuring solution-dependent sources, such as in the Brinkman force modeling[44,51,55,56] or in the discretization of reaction–diffusion-type equations.[57] Also, other numerical schemes, such as those making use of weighted integral approximations, like the finite element method (FEM), enforce a neighbor averaging representation of the source term, recovering a very similar discretization structure in terms of spurious terms. For example, the linear FEM discretization of the above problem is also described by Eqs. (41) with $\overline{\delta\nu} = -\frac{1}{6}\, T$. Therefore, the TRT scheme with $\Lambda = \frac{1}{8}$ has the same bulk discretization structure as the linear FEM on a uniform mesh, although the validity of this result is limited to straight geometries.[55,56] This exact equivalence between apparently so different numerical schemes will be demonstrated ahead through numerical results.

Finally, to better understand how the $\overline{\delta\nu}$ artifact modifies the discrete approximation toward the physical continuous description given by Eqs. (36), it is convenient to re-express Eqs. (41) in the following equivalent form:

$$a_x + 2\,\Omega_z\, \mathrm{v}_j + \nu\,(1+\overline{\delta\nu}^2)\,\overline{\Delta}_z^2 \mathrm{u}_j = \overline{\delta\nu}\,(2\,\Omega_z\,\mathrm{u}_j), \tag{46a}$$

$$-2\,\Omega_z\,\mathrm{u}_j + \nu\,(1+\overline{\delta\nu}^2)\,\overline{\Delta}_z^2 \mathrm{v}_j = \overline{\delta\nu}\,(a_x + 2\,\Omega_z\,\mathrm{v}_j). \tag{46b}$$

Looking at Eqs. (46), the impact of $\overline{\delta\nu}$ can be identified on two fronts.

First, it modifies the model viscosity as $\nu \to \nu\,(1+\overline{\delta\nu}^2)$, making the numerical model slightly over-dissipative. At leading order, this term contributes to $\mathcal{O}(\epsilon^4)$ modifications, which can be considered of minor importance compared to the leading order truncation error $\mathcal{O}(\epsilon^2)$.

Second, the most striking effect comes from the right-hand side terms introduced in the discrete momentum balance, which scale with $\overline{\delta\nu}$. Given that $\overline{\delta\nu}$ scales with $\mathcal{O}(\epsilon^2)$, these spurious sources equally compete with the leading truncations of the physical discrete Laplacian terms. For example, $\overline{\delta\nu}(2\,\Omega_z\,u_x) = \left(\frac{8\Lambda-3}{12}\right) 2\,\omega^2\,\epsilon^2\,(2\,\Omega_z\,u_x)$ interferes at the same level with $\nu\,\frac{\epsilon^2}{12}\frac{\mathrm{d}^4 u_x}{\mathrm{d}z^4}$, the leading order truncation from $\overline{\Delta}_z^2 \mathrm{u}_j \simeq \frac{\mathrm{d}^2 u_x}{\mathrm{d}z^2} + \frac{\epsilon^2}{12}\frac{\mathrm{d}^4 u_x}{\mathrm{d}z^4} + \cdots$.

With the improved force (IF) source model, given by Eq. (19) in Sec. II E, the TRT scheme reproduces the artifact-free discrete system of equations

$$a_x + 2\,\Omega_z\,\mathrm{v}_j + \nu\,\overline{\Delta}_z^2 \mathrm{u}_j = 0, \tag{47a}$$

$$-2\,\Omega_z\,\mathrm{u}_j + \nu\,\overline{\Delta}_z^2 \mathrm{v}_j = 0, \tag{47b}$$

which also releases the bulk solution from any constraint on Λ. The extension of the IF model to other channel flow orientations, e.g., diagonal or arbitrarily inclined ones, as proposed in Sec. II E, is theoretically derived in Subsection 2 of Appendix C and will be numerically tested in Sec. III C.

2. Wet node solution

a. Formulation. The wet node formulation considers the LBM discretization of the channel flow depicted in Fig. 4(b) to be split into H computational cells of unitary size, with cell vertex grids nodes located at $z_j = -\frac{H}{2} + j$ where $j = 0, 1, \ldots, H$.

The fluid velocity is subject to the no-slip velocity boundary condition (BC), $\vec{u}(\vec{x}_\mathrm{w}) = \vec{0}$, at bottom and top solid walls. Note, the boundary node coincides with the solid wall, $\vec{x}_\mathrm{b} = \vec{x}_\mathrm{w}$. Hence, the no-slip BC at the boundary node, $\vec{x}_\mathrm{b} = (x, y, z_b)$ where $z_b = \pm H/2$, applies in the discrete solution as follows:

$$(\mathrm{u}_j,\, \mathrm{v}_j) = (0,\, 0) \quad \text{at} \quad z_j = \pm\frac{H}{2}. \tag{48}$$

Owing to its "wet node" character, the use of Eq. (29) with Eq. (30) permits exactly assigning the macroscopic BC, Eq. (48), on the boundary nodes $\vec{x}_b$, similarly to what is done by standard macroscopic (cell vertex) difference schemes.

Under this framework, the *exact discrete solution* of this problem, constructed in symbolic form, yields the following $\phi_j := \phi(z_j)$ solution:

$$\phi_j = -\frac{i\,a_x}{2\,\Omega_z}\left[1 - \mathcal{A}(\lambda^{-z_j} + \lambda^{z_j})\right], \tag{49}$$

with

$$\mathcal{A} = \frac{\lambda^{H/2}}{1+\lambda^H}, \tag{50}$$

and the parameter λ is found as the root of the quadratic equation $\lambda^2 - \lambda(\frac{i\,T}{(1+i\,\overline{\delta\nu})} + 1) + 1 = 0$, which has the following solutions

$$\lambda = \frac{1 \pm R}{1 \mp R} \quad \text{with} \quad R^2 = \frac{i\,T}{4\,(1+i\,\overline{\delta\nu}) + i\,T} \quad \text{and} \quad T = \frac{2\,\Omega_z}{\nu}, \tag{51}$$

where the viscosity correction $\overline{\delta\nu}$ is given by Eq. (43) for the standard force (SF) or by $\overline{\delta\nu} = 0$ for the improved force (IF) scheme. Given that $\phi_j = \mathrm{u}_j + i\,\mathrm{v}_j$, the velocity solutions are easily extracted as $\mathrm{u}_j = \mathrm{Re}[\phi_j]$ and $\mathrm{v}_j = \mathrm{Im}[\phi_j]$, with their values defined on grid nodes $z_j = -\frac{H}{2} + j$ with $j = 0, 1, \ldots, H$.

b. Results. Here, the accuracy of numerical solutions for u_x and u_y is measured with the standard L_2 norm as follows:

$$\mathrm{L}_2(u_x) = \sqrt{\frac{\sum\left(u_x - u_x^{(\mathrm{exact})}\right)^2}{\sum\left(u_x^{(\mathrm{exact})}\right)^2}}, \quad \mathrm{L}_2(u_y) = \sqrt{\frac{\sum\left(u_y - u_y^{(\mathrm{exact})}\right)^2}{\sum\left(u_y^{(\mathrm{exact})}\right)^2}}, \tag{52}$$

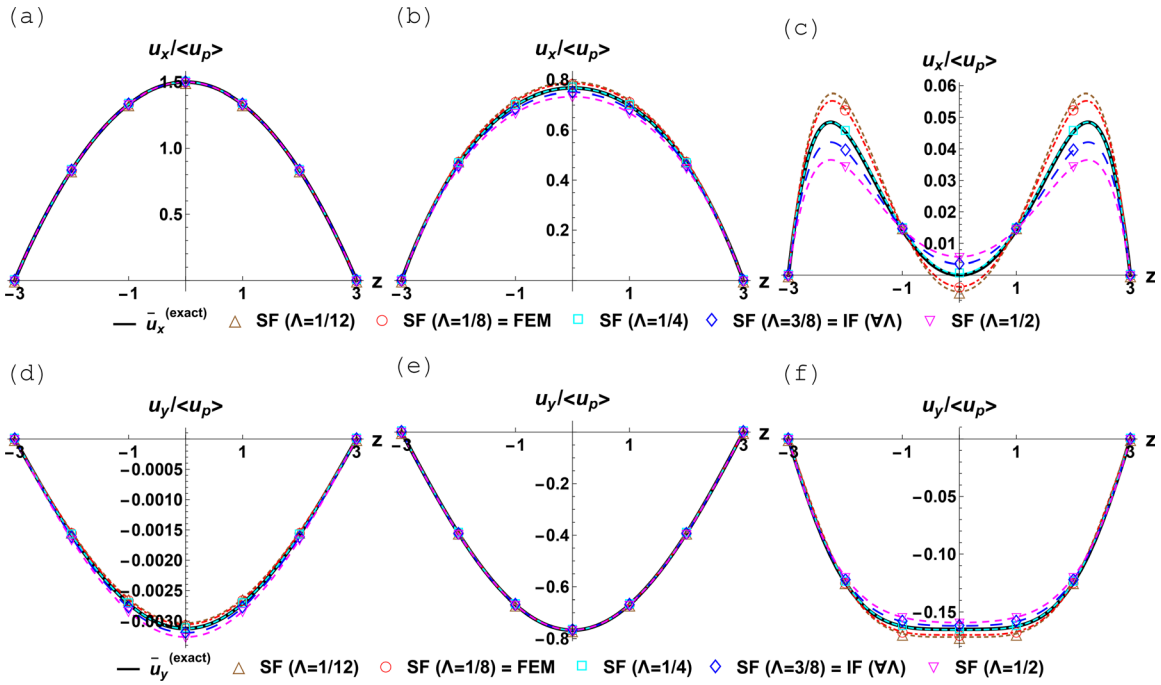

FIG. 7. Velocity profiles in a horizontal channel of size $H = 6$, discretized with $H + 1$ grid nodes, and using LSOB boundary conditions. For the same discretization FEM also employs $H + 1$ grid nodes. Panels (a) and (d) $\omega = 0.1$. Panels (b) and (e) $\omega = 2.16$. Panels (c) and (f) $\omega = 2\pi$. The normalization velocity scale is $\langle u_p\rangle = \frac{a_x H^2}{12\nu}$.

where sums are taken over all grid nodes, and $u_x := \mathrm{u}_j$ and $u_y := \mathrm{v}_j$ refer to the numerical solutions, whereas $u_x^{(\mathrm{exact})}$ and $u_y^{(\mathrm{exact})}$ are the solutions of the continuous problem; in this case, given by Eqs. (40).

Figure 7 displays symbolic solutions of the numerical velocity profiles compared against the analytical ones for three ω regimes. Table III provides the quantitative error measures. The validity of the constructed symbolic solutions was confirmed by attesting to their exact agreement with the numerical results, within their operational range of stability. For this verification analysis, the LBM symbolic solutions were compared against our in-house numerical code solutions and the FEM symbolic solutions against the COMSOL commercial code solutions.[85]

For low non-dimensional rotation rates, e.g., $\omega = 0.1$, the flow falls into the diffusion-dominated regime. Here, the numerical artifact $\overline{\delta\nu}$, which is induced by rotation, has vanishingly small values. As a result, the parabolic velocity profile tends to be recovered exactly, regardless the Λ value. When ω increases, in particular for large non-dimensional rotation rates, e.g., $\omega = 2\pi$, the numerical artifact $\overline{\delta\nu}$ takes the dominant role in the discrete momentum balance. Surprisingly, while the choice $\Lambda = \frac{3}{8}$ eliminates the $\overline{\delta\nu}$ numerical artifact, the best match between LBM and analytical solutions does not happen for this value, but close to $\Lambda = \frac{1}{4}$ (as shown in Fig. 8). To understand such an unexpected result, it is convenient to assess how continuous and discrete solutions for ϕ relate to one another. By

TABLE III. L_2 error quantification of LSOB solutions shown in Fig. 7.

	$\Lambda = \frac{1}{12}$	$\Lambda = \frac{1}{8} = \mathrm{FEM}$	$\Lambda = \frac{1}{4}$	$\Lambda = \frac{3}{8} = \mathrm{IF}(\forall\Lambda)$	$\Lambda = \frac{1}{2}$
			$\omega = 0.1$		
$L_2(u_x)$	2.45×10^{-7}	1.84×10^{-7}	1.29×10^{-9}	1.91×10^{-7}	3.85×10^{-7}
$L_2(u_y)$	0.0305	0.0228	2.69×10^{-9}	0.0228	0.0457
			$\omega = 2.16$		
$L_2(u_x)$	0.0291	0.0218	2.21×10^{-5}	0.0213	0.0422
$L_2(u_y)$	0.0032	0.0023	2.96×10^{-4}	0.0016	0.0032
			$\omega = 2\pi$		
$L_2(u_x)$	0.2149	0.1590	0.0123	0.1333	0.2453
$L_2(u_y)$	0.0336	0.0247	0.0032	0.0223	0.0432

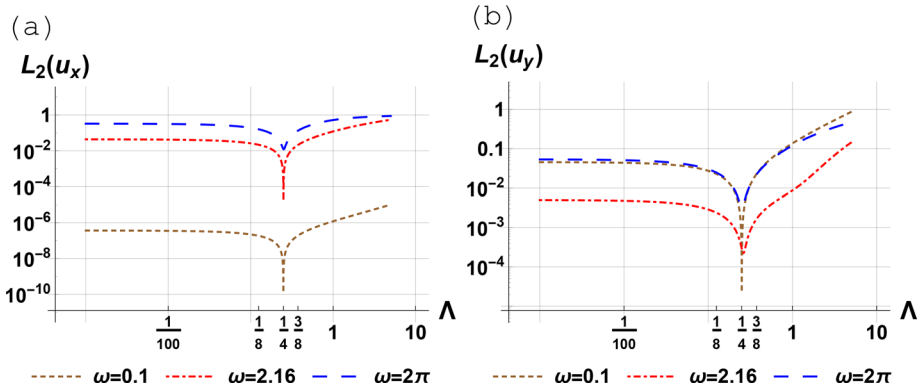

FIG. 8. Effect of the TRT free relaxation parameter Λ on the accuracy of LBM solutions with SF source scheme and LSOB boundary conditions, for the parameters considered in Fig. 7. Note, the TRT with IF source scheme and FEM solutions are Λ-independent, and their L_2 values $\forall\,\Lambda$ are given in Table III.

comparing Eqs. (39)–(49), it is found[44] that solutions for continuous ϕ and discrete ϕ_j profiles exactly match for $\lambda = \exp[(1+i)\sqrt{T/2}]$. Bearing in mind λ given by Eq. (51) with $\overline{\delta\nu}$ given by Eq. (43), then continuous, Eq. (39), and discrete, Eq. (49), ϕ solutions become identical when Λ takes the following form:

$$\Lambda = \frac{3}{8}\left[i\,\frac{4}{T} + \coth^2\left(\sqrt{i\,\frac{T}{4}}\right)\right] = \frac{3}{8}\left[i\,2\left(\frac{H}{\omega}\right)^2 + \coth^2\left(\sqrt{\frac{i}{2}\frac{\omega}{H}}\right)\right]. \tag{53}$$

Based on our in-house code, we numerically verified that the LBM solution of the complex-valued problem, given by Eq. (38), exactly matches the exponential-type solution, given by Eq. (39), when Λ is assigned to Eq. (53). However, the extension of this result to the velocity components $\mathrm{u}_j = \mathrm{Re}[\phi_j]$ and $\mathrm{v}_j = \mathrm{Im}[\phi_j]$ does not find an exact direct matching because, in this case, the continuous u_x and u_y solutions become expressed by more complex analytical functions, see Eq. (40). Nonetheless, some insight can be gained from the ϕ analysis, and in particular, from Eq. (53), if we focus on what happens for the ratio $\frac{H}{\omega} \gg 1$, which corresponds to the typical situation found in practice. When the physical regime ω is fixed, the limit $H \to \infty$ to Eq. (53) yields $\Lambda = \frac{1}{4}$, which corresponds to the Λ value that minimizes the $L_2(u_x)$ and $L_2(u_y)$ error measures, as shown in Fig. 7. The minimum at $\Lambda = \frac{1}{4}$ becomes more evident the lower ω or the higher the grid resolution H. On the other hand, when the grid resolution H is fixed, the increase in rotation rate, which is found by setting the limit $\omega \to \infty$ in Eq. (53), yields $\Lambda = \frac{3}{8}$. While not shown in the manuscript, this case was also verified numerically with our in-house LBM code.

Finally, we would like to point out that, in this setup, the TRT with $\Lambda = \frac{1}{8}$ and the linear FEM produce the same discretization structure. In other words, they recover the same discrete solutions, up to the machine's accuracy. The validity of the FEM symbolic solutions was confirmed numerically using the COMSOL commercial software.[85] This test permits showing that by adjusting the extra degree of freedom Λ available in the TRT, the discrete structure of the scheme can be optimized in order to reach more accurate solutions than the traditional discretization methods for the NSEs with the same formal order of accuracy, such as the linear FEM studied herein.

3. Linkwise solution

a. Formulation. Based on the linkwise formulation, the LBM discretization of the channel flow depicted in Fig. 4(c) is split into H computational cells of unitary size, with cell-centered grid nodes located at $z_j = -\frac{H}{2} + \frac{1}{2} + j$ where $j = 0, 1, \ldots, H-1$.

To construct the symbolic solutions, it is necessary to unfold the explicit form of the closure relations satisfied by the linkwise boundary rules in terms of the macroscopic variables of interest. The works[21,41,43,58,59] showed that, for linkwise boundary schemes, the macroscopic BC applying at $\vec{x}_\mathrm{w}$ is expressed as a truncated Taylor series of the fluid velocity around the boundary node $\vec{x}_\mathrm{b}$, with the spatial increment δ_q directed along the wall cut link $\vec{c}_q$.

Let us consider the horizontal channel with walls located at $z_\mathrm{w} = \pm\left(\frac{H}{2} - \frac{1}{2} + \delta_z\right)$ and boundary nodes located at $z_\mathrm{b} = \pm\left(\frac{H}{2} - \frac{1}{2}\right)$ with the distance between these two sites, $\delta_z = |z_\mathrm{w} - z_\mathrm{b}|$, with $\delta_z = \frac{1}{2}$ here, so that $z_\mathrm{w} = \pm\frac{H}{2}$. For the purpose of analysis, only the nontrivial links cut by walls are considered, i.e., the diagonal links satisfying $c_{qx}c_{qz} \neq 0$ and/or $c_{qy}c_{qz} \neq 0$, where c_{qz} points in the wall normal direction. By following the derivation steps explained in the works,[55,56] it is possible to derive the symbolic solutions of the closure relations obeyed by linkwise boundary schemes, such as BB or MLI, which for the rotating channel setup are given by

$$\begin{aligned} c_{qx}\Big[&\mathrm{u}_j + \mathrm{sgn}(c_{qz})\,\alpha^+\,\overline{\Delta}_z\mathrm{u}_j + \alpha^-\,\overline{\Delta}_z^2\mathrm{u}_j \\ &+ \overline{\delta\nu}\left(\mathrm{sgn}(c_{qz})\,\alpha^+\,\overline{\Delta}_z\mathrm{v}_j + \alpha^-\,\overline{\Delta}_z^2\mathrm{v}_j\right)\Big]\Big|_{z_\mathrm{b}} \\ + c_{qy}\Big[&\mathrm{v}_j + \mathrm{sgn}(c_{qz})\,\alpha^+\,\overline{\Delta}_z\mathrm{v}_j + \alpha^-\,\overline{\Delta}_z^2\mathrm{v}_j \\ &- \overline{\delta\nu}\left(\mathrm{sgn}(c_{qz})\,\alpha^+\,\overline{\Delta}_z\mathrm{u}_j + \alpha^-\,\overline{\Delta}_z^2\mathrm{u}_j\right)\Big]\Big|_{z_\mathrm{b}} = 0, \end{aligned} \tag{54}$$

where $z_\mathrm{b} = \mathrm{sgn}(c_{qz})\left(\frac{H}{2} - \frac{1}{2}\right)$ and the sgn function is defined as

$$\mathrm{sgn}(c_{qz}) = \begin{cases} +1 & c_{qz} > 0, \\ -1 & c_{qz} < 0. \end{cases} \tag{55}$$

Note that, for notation convenience, Eq. (54) is once again expressed in terms of compact finite-difference operators, where the discrete Laplacian was defined in Eq. (42) and the discrete gradient operator is defined as

$$\overline{\Delta}_z\mathrm{u}_j = \frac{\mathrm{u}_{j+1} - \mathrm{u}_{j-1}}{2} \quad \text{and} \quad \overline{\Delta}_z\mathrm{v}_j = \frac{\mathrm{v}_{j+1} - \mathrm{v}_{j-1}}{2}. \tag{56}$$

TABLE IV. Coefficients α^+ and α^- in Eqs. (54) and (57), with $\delta_z \in]0, 1]$.

	SF [Eq. (8d)]		IF [Eq. (19)]	
	α^+	α^-	α^+	α^-
BB [Eq. (31)]	$\frac{1}{2}$	$\frac{2\Lambda}{3}$	$\frac{1}{2}$	$\frac{1}{4}$
MLI [Eq. (32)]	δ_z	$\frac{\delta_z^2}{2}$	δ_z	$\frac{\delta_z^2}{2}$

Remark 3.4. When applied at boundary nodes, the discrete operators $\overline{\Delta}_z$ and $\overline{\Delta}_z^2$ require values from the nodes $j \pm 1$ that lie outside the fluid domain. For the construction of the symbolic solutions, they are computed on the virtual linkwise continuation of the solution at node j, as explained in previous works.[55,56] By following this procedure, the obtained symbolic solutions exactly match the numerical LBM solutions over all nodal values.

By using the IF strategy, Eq. (54), the viscosity correction term becomes $\overline{\delta\nu} = 0$, which reduces the boundary closure relation, Eq. (54), to an artifact-free Taylor-type condition for the wall no-slip condition

$$c_{qx}\left[\mathrm{u}_j + \mathrm{sgn}(c_{qz})\,\alpha^+\,\overline{\Delta}_z \mathrm{u}_j + \alpha^-\,\overline{\Delta}_z^2 \mathrm{u}_j\right]\Big|_{z_b} + c_{qy}\left[\mathrm{v}_j + \mathrm{sgn}(c_{qz})\,\alpha^+\,\overline{\Delta}_z \mathrm{v}_j + \alpha^-\,\overline{\Delta}_z^2 \mathrm{v}_j\right]\Big|_{z_b} = 0. \tag{57}$$

The coefficients α^+ and α^- in Eqs. (54) and (57) are specified in Table IV for the BB and MLI schemes and the source model employed, SF and IF.

Remark 3.5. According to Eq. (54), the source term artifact $\overline{\delta\nu}$ comes in the closure relation of the linkwise boundary schemes by introducing extra gradient and Laplacian velocity terms. As a result, the boundary closure relations, which should only depend on δ_z to determine the no-slip wall location, will be dependent on the $\overline{\delta\nu}$ value as well. Worse, if the BGK or REG collision models were to be used with the BB boundary scheme, then this $\overline{\delta\nu}$ artifact would make the no-slip wall location become viscosity dependent already at the first order, as dictated by the $\overline{\delta\nu}\,\alpha^+$ combination. This unphysical $\nu-$dependency is removed from the BB scheme by TRT or MRT collision operators. Yet, even with these models, the $\overline{\delta\nu}$ artifact remains present. As such, the no-slip wall location can still vary with the rotational regime through the ω-dependency on $\overline{\delta\nu}$ (this issue can be visualized in Fig. 9). The vanishing of $\overline{\delta\nu}$ in the BB boundary closure relations can be achieved either: (1) by tuning Λ to suitable values in the SF scheme, e.g., the $\Lambda = 3/8$ in horizontal channel case, or (2) by using the IF scheme, which liberates Λ to other features. The alternative consists in using higher-order boundary schemes, such as the MLI presented in Eq. (32), where this $\overline{\delta\nu}$ artifact is removed by design.

To proceed with the analysis, and in order to aid in the construction of the symbolic solutions, we rewrite the above boundary closure relations, Eqs. (54) and (57), in terms of the complex velocity ϕ_j parameter, which takes the form

$$\phi_j + \mathrm{sgn}(c_{qz})\,\beta^+\,\overline{\Delta}_z \phi_j + \beta^-\,\overline{\Delta}_z^2 \phi_j\big|_{z_b} = 0, \tag{58}$$

where the boundary coefficients $\beta^{\pm}$ are given in Table V. Based on this complex velocity, the $\mathrm{Re}[\phi_j]$ and $\mathrm{Im}[\phi_j]$ solutions of Eq. (58) provide the boundary closures for u_j and v_j, respectively.

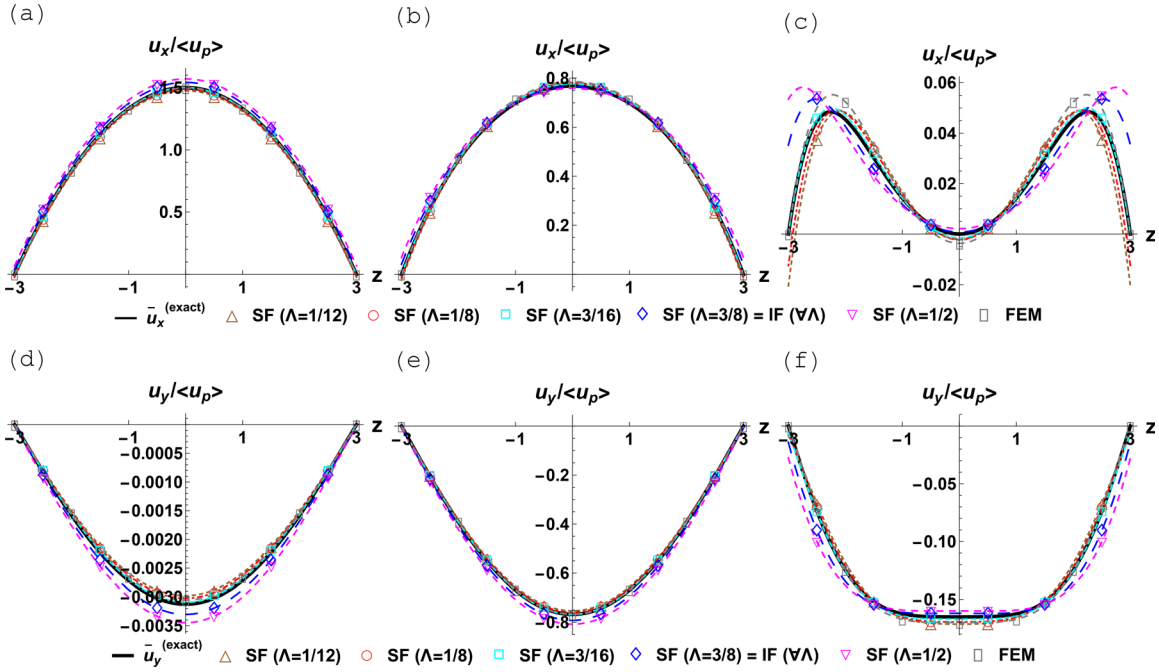

FIG. 9. Velocity profiles in a horizontal channel of size $H = 6$, discretized with H grid nodes and $\delta_z = 1/2$, and using BB boundary conditions. For the same discretization FEM employs $H + 1$ grid nodes. Panels (a) and (d) $\omega = 0.1$. Panels (b) and (e) $\omega = 2.16$. Panels (c) and (f) $\omega = 2\pi$. The normalization velocity scale is $\langle u_p\rangle = \frac{g_z H^2}{12\nu}$.

TABLE V. Coefficients β^+ and β^- in Eq. (58), with $\delta_z \in]0,1]$, and $\overline{\delta\nu}$ is given by Eq. (43).

	SF [Eq. (8d)]		IF [Eq. (19)]	
	β^+	β^-	β^+	β^-
BB [Eq. (31)]	$\frac{1}{2}(1+i\overline{\delta\nu})$	$\frac{2\Lambda}{3}(1+i\overline{\delta\nu})$	$\frac{1}{2}$	$\frac{1}{4}$
MLI [Eq. (32)]	δ_z	$\frac{\delta_z^2}{2}$	δ_z	$\frac{\delta_z^2}{2}$

In this framework, the *exact discrete solution* of this problem is constructed by coupling Eq. (54) with the bulk solution from Eq. (45). The symbolic solution of $\phi_j := \phi(z_j)$ is

$$\phi_j = -\frac{i\,a_x}{2\,\Omega_z}\left[1-\mathcal{B}(\lambda^{z_j}+\lambda^{-z_j})\right], \tag{59}$$

with

$$\mathcal{B} = \frac{\lambda^{(3+H)/2}}{\lambda(\lambda+\lambda^H)+\frac{1}{2}\beta^+(-1+\lambda^2)(-\lambda+\lambda^H)+\beta^-(-1+\lambda)^2(\lambda+\lambda^H)}, \tag{60}$$

where the coefficients $\beta^{\pm}$ are given in Table V and λ is a root of the quadratic equation whose solution is given in Eq. (51). Since $\phi_j = \mathrm{u}_j + i\,\mathrm{v}_j$, discrete velocity solutions are $\mathrm{u}_j = \mathrm{Re}[\phi_j]$ and $\mathrm{v}_j = \mathrm{Im}[\phi_j]$, defined on the grid nodes $z_j = -\frac{H}{2}+\frac{1}{2}+j$ with $j = 0, 1, \ldots, H-1$.

b. Results. The accuracy of u_x and u_y numerical solutions is measured with the standard L_2 norm given by Eq. (52). Figure 9 displays symbolic solutions of the numerical velocity profiles obtained with the BB boundary scheme and compares them against analytical ones for the aforementioned three ω regimes. Table VI provides the quantitative error measures. Once again, the validity of the constructed symbolic solutions was attested by verifying their exact agreement with numerical results in both LBM and FEM cases; LBM was computed with our in-house code and FEM was computed with COMSOL software.[85]

The repetition of the study, previously performed for wet node boundaries, now using the BB rule, introduces as a new feature the interplay of the $\overline{\delta\nu}$ numerical error between bulk discretization and no-slip BC approximation. According to the symbolic solutions derived above, see Eq. (54), the leading order error in this case [that scales with $\mathcal{O}(\epsilon)$] is due to the BB boundary rule. This theoretical result is numerically confirmed by the profiles shown in Fig. 9; they clearly reveal that the influence of $\overline{\delta\nu}$, reflected by the effect of Λ on the solutions, becomes significantly more noticeable close to the walls, where the profile accommodation gets controlled by the LBM boundary scheme. In this respect, we find that increasing Λ leads to larger wall slips, while lowering Λ may lead to negative slips, which implies the existence of near-wall flow reversions artificially promoted by the BB rule. In other words, the accommodation of the overall solution is determined by a condition of insufficient lower accuracy when the BB boundary is used. A further testament to the dominating role of the force discretization artifact $\overline{\delta\nu}$ is dominated by the BB boundary, which is seemed on the variability of the solution with Λ, which tends to diminish when shifting away from the walls toward the bulk region.

Figure 10 provides a more detailed look at the Λ effect over the BB overall accuracy. When $\omega = 0.1$, the $\overline{\delta\nu}$ artifact becomes negligibly small and the u_x profile gets near parabolic. Hence, in agreement with theoretical results for the Poiseuille flow solution,[41,43,45,59] the best accuracy for u_x with the BB rule happens for $\Lambda = 3/16$. Interestingly, this $\Lambda = 3/16$ optimal choice remains approximately fixed when ω increases toward higher rotational regimes, which seems to indicate that, for all ω regimes, boundary errors dominate over bulk ones. This conclusion is corroborated by the fact that the IF scheme, which vanishes $\overline{\delta\nu}$ from the BB solutions, does not seem to provide the best numerical accuracy. The reason comes from the inaccurate values taken by the coefficients of the BB closure relation when the IF scheme is adopted, which is identical to the $\Lambda = 3/8$ choice in the SF case. The two cases lead to an overestimation by a factor of 2 on the coefficient of the flow curvature in the boundary closure relation, i.e., α^- in Table IV, and this error controls accuracy here. In this regard, letting the $\overline{\delta\nu}$ force artifact be present in both bulk and boundary approximations and just correcting the error specific to the BB scheme, as done by the $\Lambda = 3/16$ choice, seems to be the preferable choice. This observation suggests that any attempt to eliminate $\overline{\delta\nu}$ through an improved force discretization alone, like with the IF scheme proposed here, does

TABLE VI. L_2 error quantification of BB solutions shown in Fig. 9.

	$\Lambda = \frac{1}{12}$	$\Lambda = \frac{1}{8}$	$\Lambda = \frac{3}{16}$	$\Lambda = \frac{3}{8} = \mathrm{IF}\ (\forall\,\Lambda)$	$\Lambda = \frac{1}{2}$	FEM
			$\omega = 0.1$			
$L_2(u_x)$	0.0211	0.0127	8.95×10^{-8}	0.0380	0.0634	1.84×10^{-7}
$L_2(u_y)$	0.0486	0.0336	0.0108	0.0590	0.1069	0.0228
			$\omega = 2.16$			
$L_2(u_x)$	0.0185	0.0135	0.0103	0.0313	0.0495	0.0218
$L_2(u_y)$	0.0212	0.0129	0.0005	0.0363	0.0604	0.0023
			$\omega = 2\pi$			
$L_2(u_x)$	0.1580	0.0935	0.0355	0.1821	0.2338	0.1590
$L_2(u_y)$	0.0382	0.0238	0.0111	0.0731	0.1146	0.0247

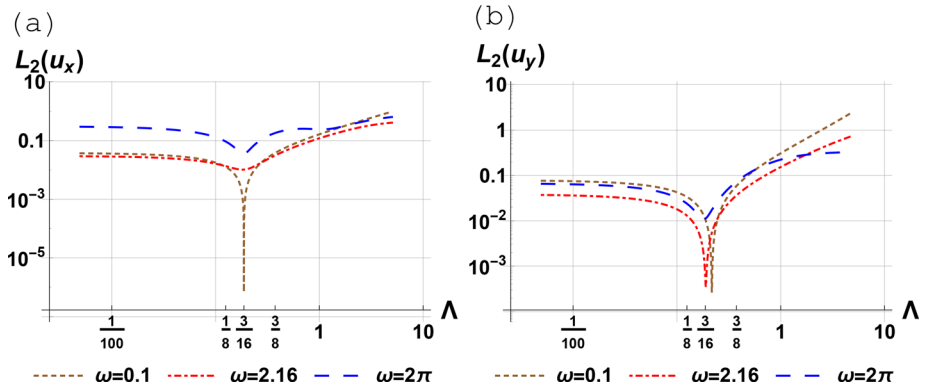

FIG. 10. Effect of the TRT-free relaxation parameter Λ on the accuracy of LBM solutions with SF source scheme and BB boundary conditions, for the parameters considered in Fig. 9. Note, the TRT with IF source scheme and FEM solutions do not vary with Λ, and their L_2 values $\forall\,\Lambda$ are given in Table VI.

not guarantee improved accuracy, but it should be combined with an equally accurate boundary model.

In order to clear up this last conclusion, Fig. 11 provides the velocity profiles of the parabolic accurate MLI boundary scheme. Table VII lists the respective error measures. The MLI scheme eliminates the $\overline{\delta\nu}$ error from its boundary closure relation. Hence, although LBM solutions, for the same ω, may vary in bulk due to featuring different Λ values, they all converge to the same velocity at the wall location. Even if solutions typically improve in accuracy, it turns out that the symbolic continuation of these velocity profiles toward the wall does not match the prescribed wall velocity boundary condition. This artificial wall slip is particularly noticeable when boundary layers are sharp and cannot be resolved by the mesh, e.g., as happens when ω is large and H is coarse. Such behavior is intrinsic to linkwise schemes as, due to their off-node placement of the no-slip BC, they realize the wall in an implicit way, through a second-order Taylor series approximation, as described by Eq. (58). Therefore, when the solution features a steep velocity gradient close to the wall, the unaccounted $\mathcal{O}(\epsilon^3)$ truncations in the Taylor series representation of the no-slip BC become relevant, and the mismatch causes the observed wall slip. Yet, rather than a drawback, this freedom to slip at the wall tends to be beneficial in under-resolved simulations since it permits a smoother accommodation of the bulk solution on the boundary. This behavior contrasts with the on-node placement of the no-slip BC, typically considered by wet node boundary schemes, where the wall condition is enforced exactly. Its downside is that, when the bulk solution is not sufficiently

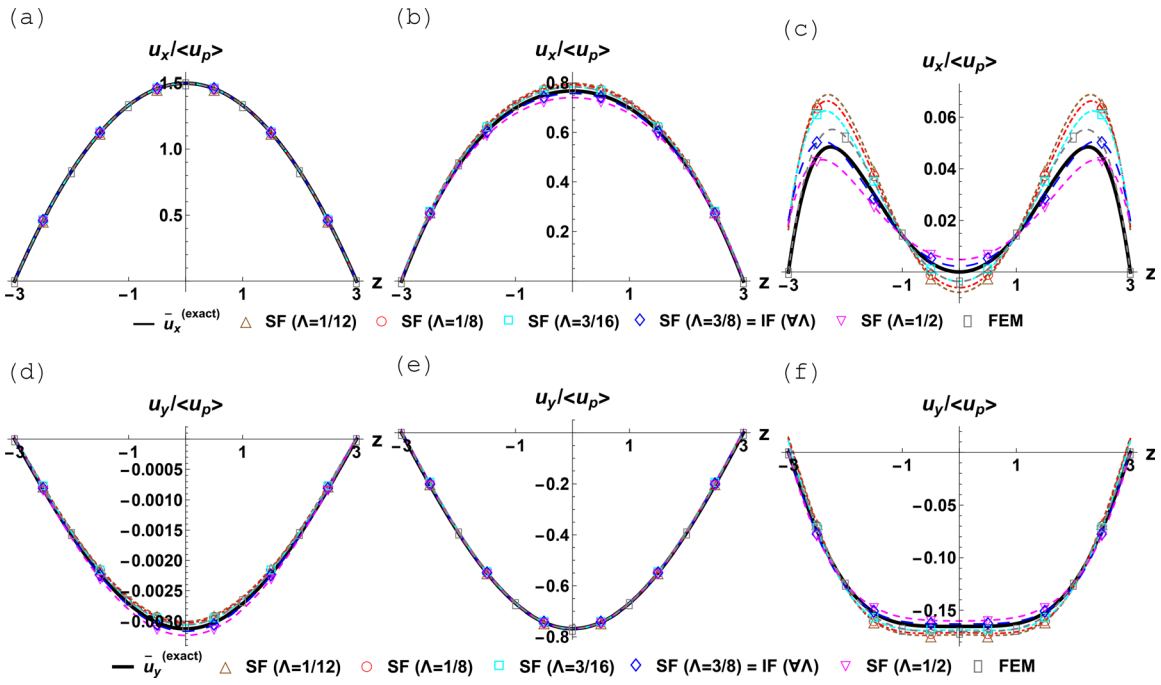

FIG. 11. Velocity profiles in a horizontal channel of size $H = 6$, discretized with H grid nodes and $\delta_z = 1/2$, and using MLI boundary conditions. For the same discretization FEM employs $H + 1$ grid nodes. Panels (a) and (d) $\omega = 0.1$. Panels (b) and (e) $\omega = 2.16$. Panels (c) and (f) $\omega = 2\pi$. The normalization velocity scale is $\langle u_p\rangle = \frac{a_x H^2}{12\nu}$.

TABLE VII. L_2 error quantification of MLI solutions shown in Fig. 11.

	$\Lambda = \frac{1}{12}$	$\Lambda = \frac{1}{8}$	$\Lambda = \frac{3}{16}$	$\Lambda = \frac{3}{8} = \text{IF}\ (\forall\, \Lambda)$	$\Lambda = \frac{1}{2}$	FEM
			$\omega = 0.1$			
$L_2(u_x)$	3.39×10^{-7}	2.79×10^{-7}	1.89×10^{-7}	9.45×10^{-8}	2.84×10^{-7}	1.84×10^{-7}
$L_2(u_y)$	0.0435	0.0359	0.0247	0.0114	0.0335	0.0228
			$\omega = 2.16$			
$L_2(u_x)$	0.0416	0.0342	0.0234	0.0108	0.0311	0.0218
$L_2(u_y)$	0.0095	0.0086	0.0073	0.0041	0.0026	0.0023
			$\omega = 2\pi$			
$L_2(u_x)$	0.4366	0.3871	0.3118	0.1089	0.1138	0.1590
$L_2(u_y)$	0.0583	0.0459	0.0296	0.0204	0.0386	0.0247

well-resolved near the wall, such an exact enforcement of the no-slip velocity condition at the boundary node may act as an over-constraint, distorting the velocity profile in the process to accommodate it.

In a similar fashion, the attempt to accommodate a defective bulk solution on an error-free boundary condition also creates an incompatible over-constraint on the simulated flow field. This mismatch leads to the distortion of the numerical velocity profiles, and it explains why the attempt to match a $\overline{\delta\nu}$-contaminated SF solution on an error-free MLI boundary condition leads to such inaccurate solutions. For example, at $\omega = 2\pi$, the error in SF solutions is typically much larger with the MLI scheme than with the BB rule, which allows the $\overline{\delta\nu}$ artifact to be present at boundaries. The improvement in the accuracy of solutions requires eliminating the $\overline{\delta\nu}$ artifact in both bulk and boundary approximations. This optimal accuracy is achieved with the MLI boundary rule combined with the SF scheme using $\Lambda = 3/8$ or preferably with the IF, which is valid for all Λ values.

Figure 12 shows the effect of Λ on the SF solution accuracy with MLI boundaries and confirms that the error minima occur around $\Lambda = 3/8$. Small deviations to this value are due to the coarseness of the mesh; while not shown in the manuscript, it was confirmed that refining the mesh shifts the error minima toward $\Lambda = 3/8$.

C. Inclined channel setup

This section revisits the study developed in Sec. III B 3, extending it from a horizontal lattice-aligned Ekman–Poiseuille channel flow to a channel orientation not compliant with the mesh, considering $\alpha = 0$ and $\theta = \arctan(1/2)$ inclinations with respect to the 3D lattice; other angles were also tested and do not modify conclusions. Moreover, due to the particular problem geometry, the obtained numerical solutions are not impacted by the cubic lattice choice. Hence, without loss of generality, the standard D3Q19 was used throughout this study. To keep up with the analysis of Sec. III, the non-linear velocity terms are absent from the numerical model, $E_q = 0$ in Eq. (8b). While this choice does not make any difference in the previous test case, where the flow is parallel to the lattice, it is now important because these non-linear velocities, if considered in E_q, they will not vanish in the numerical solution of inclined channels, contrary to what should be expected from the physical solution, as explained in Sec. II D of work.[61] The analytical solutions remain given by Eq. (40), but are now more conveniently represented on the (x', y', z') coordinate system, given by Eq. (14).

In this test case, the exact symbolic construction of the numerical solutions is no longer possible. The consequence is that the $\overline{\delta\nu}$ correction, determined by the exact discrete equations, has to be expressed in approximated form.[44] A second-order approximation $\overline{\delta\nu}^{(2)}$ is derived in Subsection 2 of Appendix C and is used in this study. Also, since the geometry walls do not align with the underlying mesh, the off-node treatment of boundaries is mandatory to avoid a staircase description of the geometry.[21] The study of the correct representation of the flow walls focuses on the linkwise schemes BB and MLI, described in

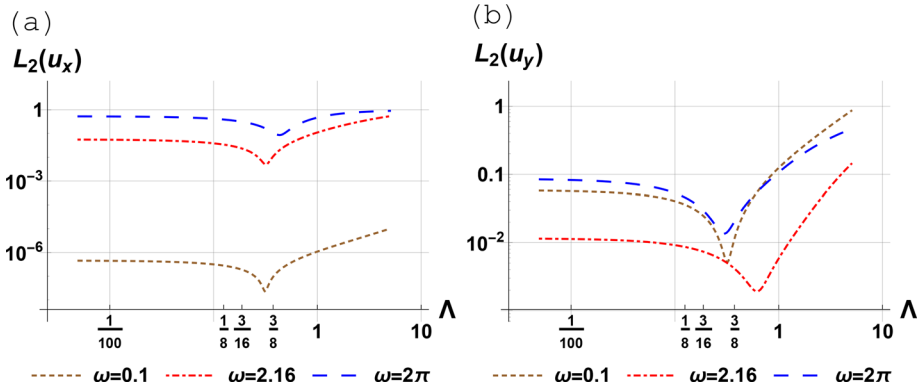

FIG. 12. Effect of the TRT-free relaxation parameter Λ on the accuracy of LBM solutions with SF source scheme and MLI boundary conditions, for the parameters considered in Fig. 11. Note, the TRT with IF source scheme and FEM solutions do not vary with Λ, and their L_2 values $\forall\, \Lambda$ are given in Table VII.

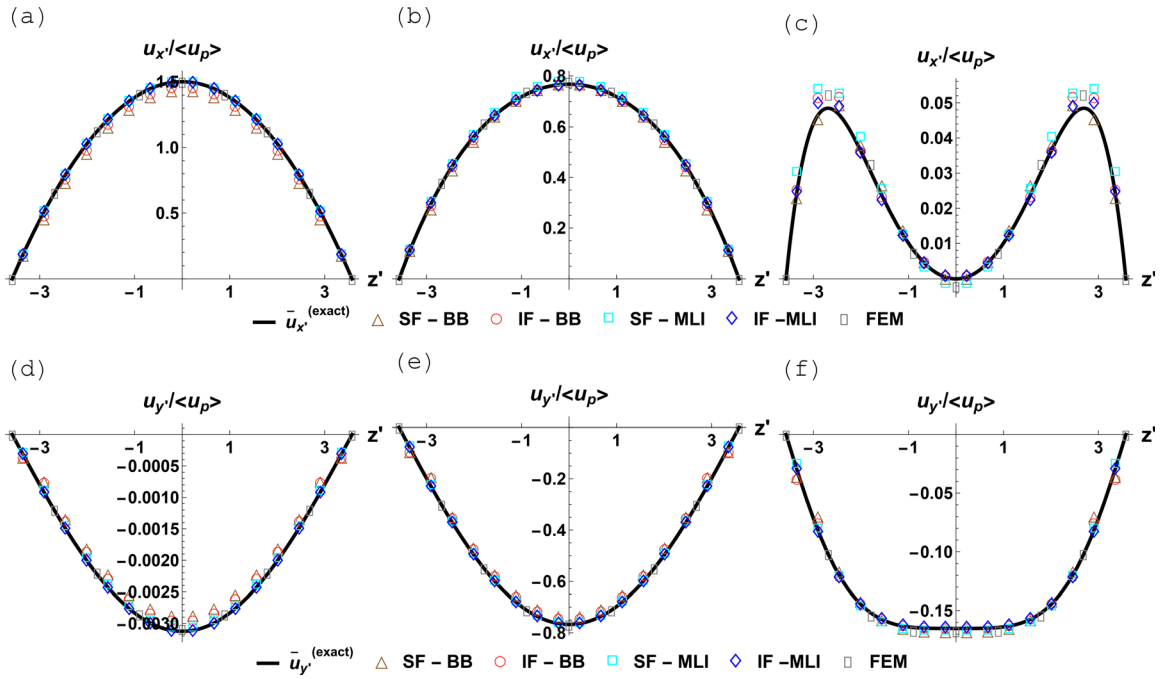

FIG. 13. Velocity profiles in an inclined channel of size $h = H\cos(\theta)$, where $\theta = \arctan(1/2)$, discretized with $H = 8$ grid nodes per column (so that the effective channel height is $h = 8\cos(0.46) \approx 7.15$), and using different forcing schemes and boundary conditions, with $\Lambda = 3/16$. For the same discretization FEM employs $H + 1$ grid nodes. Panels (a) and (d) $\omega = 0.1$. Panels (b) and (e) $\omega = 2.16$. Panels (c) and (f) $\omega = 2\pi$. The normalization velocity scale is $\langle u_p\rangle = \frac{a_x h^2}{12\nu}$.

Sec. II F 2. The discretization of the inclined channel geometry in FEM uses a body-fitted structured grid constructed with COMSOL code.[85]

Figure 13 illustrates the numerical velocity profiles for LBM and FEM vs the exact solutions over the three ω rotation regimes, previously considered. The corresponding L_2 accuracy values are listed in Table VIII. Comparing the results obtained here against those presented in Sec. III B 3 for a horizontal channel flow with linkwise boundary schemes, the two cases show many similarities. At small ω, it is confirmed that the accurate representation of the boundary, through the parabolic accurate MLI boundary scheme, leads to the best accuracy alongside FEM. In the other limit, at large ω, the rotation force becomes dominant. So, the ability to correct the source term artifacts, via the IF scheme, assumes the key role in the solution accuracy. The TRT operating on a simple uniform Cartesian mesh discretization, when using the IF together with the MLI scheme, tends to surpass the accuracy of FEM, which employs hardworking body-fitted meshes. Overall, this test intends to showcase that, whenever ω is large, the accuracy of the numerical solutions is essentially controlled by the Coriolis force term approximation rather than by how well the boundary is resolved.

TABLE VIII. L_2 error quantification of TRT and FEM solutions shown in Fig. 13.

	SF-BB	IF-BB	SF-MLI	IF-MLI	FEM
			$\omega = 0.1$		
$L_2(u_x)$	0.0478	0.0292	1.10×10^{-7}	2.53×10^{-8}	1.19×10^{-7}
$L_2(u_y)$	0.0921	0.0641	0.0141	0.0024	0.0128
			$\omega = 2.16$		
$L_2(u_x)$	0.0175	0.0082	0.0132	0.0035	0.0122
$L_2(u_y)$	0.0551	0.0414	0.0032	0.0005	0.0012
			$\omega = 2\pi$		
$L_2(u_x)$	0.0604	0.0887	0.1439	0.0539	0.0852
$L_2(u_y)$	0.0389	0.0283	0.0187	0.0074	0.0139

IV. ROTATING DUCT FLOW: IMPROVED ADVECTION MODELING

In this section, we aim to understand the role of the equilibrium term in the LBM modeling of rotating fluid flows. For that, we consider the modeling of a fully developed duct flow subject to rotation.[9,11] This test case permits studying how the LBM modeling of the advection term may interfere with the correct hydrodynamic description of this problem class. In this regard, an improved equilibrium structure[77–79] is shown in this section to be able to correct defects present in the D3Q19 lattice model.

A. Theoretical formulation

Consider the 3D channel sketched in Fig. 14, which has a square cross section with length H and rotates about an axis perpendicular to its own axis with steady constant angular velocity $\vec{\Omega} = \Omega_z \vec{i}_z$, where $\Omega_z > 0$. Inside the channel an incompressible fluid flows with a velocity field $\vec{u} = u_x \vec{i}_x + u_y \vec{i}_y + u_z \vec{i}_z$, subject to the external body force $\vec{F}$ given by Eq. (15). The flow is steady $\frac{\partial}{\partial t} = 0$ and invariant along the streamwise flow directions $\frac{\partial}{\partial x} = 0$.

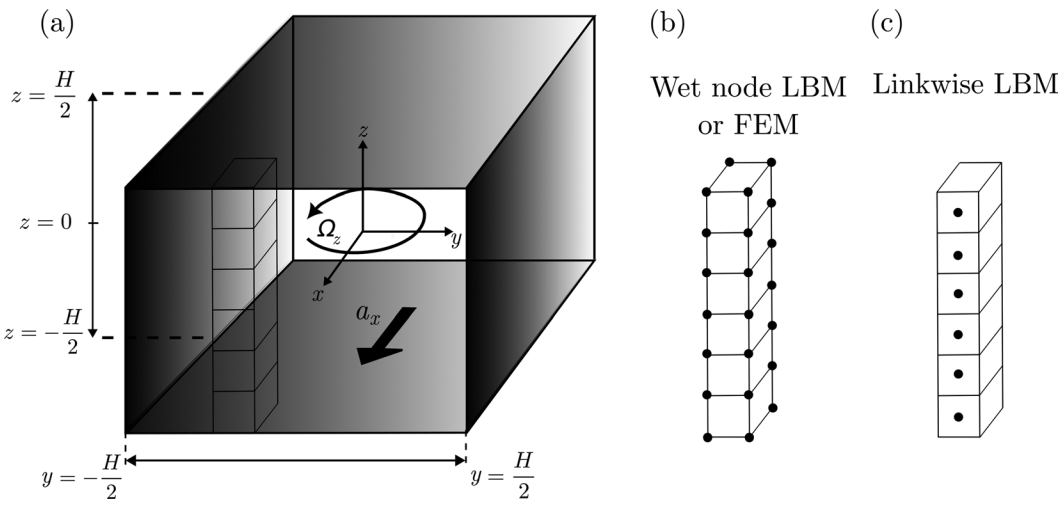

FIG. 14. Square duct rotating channel flow. (a) Geometry and relevant parameters. (b) Computational cells according to wet node boundary discretization or cell vertex FEM discretization (vertex-centered discretization). (c) Computational cells according to linkwise boundary discretization (cell-centered discretization).

To assess the magnitude of each term in the dynamical balance of this problem, let us introduce the dimensionless transformations $x_i \mapsto H\,\overline{x}_i$ and $u_i \mapsto U\,\overline{u}_i$, where H and U are length and velocity reference scales, respectively. In dimensionless form, the steady and incompressible NSEs, Eqs. (1), applied to the rotating channel setup shown in Fig. 14 read as follows:[9,11]

$$\partial_{\overline{y}}\overline{u}_y + \partial_{\overline{z}}\overline{u}_z = 0, \tag{61a}$$

$$\partial_{\overline{y}}(\overline{u}_x\overline{u}_y) + \partial_{\overline{z}}(\overline{u}_x\overline{u}_z) = \overline{a}_x + \frac{1}{\mathrm{Re}}\left[\partial_{\overline{y}\overline{y}}\overline{u}_x + \partial_{\overline{z}\overline{z}}\overline{u}_x\right] + 2\,\frac{\mathrm{Ek}}{\mathrm{Re}}\,\overline{u}_y, \tag{61b}$$

$$\partial_{\overline{y}}(\overline{u}_y^2) + \partial_{\overline{z}}(\overline{u}_y\overline{u}_z) = -\partial_{\overline{y}}\overline{P} + \frac{1}{\mathrm{Re}}\left[\partial_{\overline{y}\overline{y}}\overline{u}_y + \partial_{\overline{z}\overline{z}}\overline{u}_y\right] - 2\,\frac{\mathrm{Ek}}{\mathrm{Re}}\,\overline{u}_x, \tag{61c}$$

$$\partial_{\overline{y}}(\overline{u}_y\overline{u}_z) + \partial_{\overline{z}}(\overline{u}_z^2) = -\partial_{\overline{z}}\overline{P} + \frac{1}{\mathrm{Re}}\left[\partial_{\overline{y}\overline{y}}\overline{u}_z + \partial_{\overline{z}\overline{z}}\overline{u}_z\right], \tag{61d}$$

where $\overline{a}_x = \frac{a_x H}{U^2}$, $\overline{P} = \frac{P}{\rho_0 U^2}$, and the following dimensionless parameters have been introduced

$$\mathrm{Ek} = \frac{\Omega_z H^2}{\nu} \quad \text{and} \quad \mathrm{Re} = \frac{U H}{\nu}. \tag{62}$$

Above, Ek is identical to the square of the rotation parameter, i.e., $\mathrm{Ek} = \omega^2$, which parameterizes the Poiseuille–Ekman rotating channel flow in Sec. III. Here, Ek stands for the inverse of the Ekman number.[2] According to Eqs. (61), the effect of rotation on the fluid momentum balance is scaled by the ratio Ek/Re while the relative importance between momentum advection and diffusion is controlled by Re. Therefore, depending on the relative magnitudes of Ek and Re, the flow may fall into different physical regimes, which have been studied in dedicated contributions.[9–11] This work will exclusively focus on the regime of *slow laminar flow* $\mathrm{Re} \sim \mathcal{O}(1)$ under *weak rotation* $\mathrm{Ek} \ll \mathcal{O}(1)$, where the behavior of the fluid is characterized by an "*asymptotic invariance property*."[86] That is, providing the scalings $\mathrm{Ek}/\mathrm{Re} \ll \mathcal{O}(1)$ and $\mathrm{Re} \sim \mathcal{O}(1)$ are satisfied, variations on the individual values of these dimensionless parameters will not alter the overall structure of the flow solution. In practice, the velocity profile along the main flow direction, $\overline{u}_x$, will remain described by the Poiseuille flow solution, given by the no-rotation solution, and the secondary flow field, developing along the cross-flow directions, $(\overline{u}_y, \overline{u}_z)$, will be represented by an invariable two-cell structure. Consequently, a primary requisite for any consistent numerical solver is that it is capable of reproducing these solution features. This point will be explored in Sec. IV B to examine the capabilities of the LBM as a numerical solver for this problem class.

From the above exposition, let us first consider the base flow solution of the problem governed by Eqs. (61), which happens in the no-rotation limit. By taking $\mathrm{Ek}/\mathrm{Re} \to 0$ with $\mathrm{Re} \neq 0$ on Eqs. (61) and solving them, we obtain the classical Poiseuille flow solution in a square duct, $-1/2 \leq (\overline{y}, \overline{z}) \leq 1/2$, given by[13]

$$\overline{u}_x(\overline{y}, \overline{z}) = \frac{4\,\overline{a}_x\,\mathrm{Re}}{\pi}\sum_{n=1,3,\ldots}^{\infty}\frac{1}{n^3}(-1)^{(n-1)/2}\left[1 - \frac{\cosh(n\pi\overline{y})}{\cosh(n\pi/2)}\right]\cos(n\pi\overline{z}), \tag{63a}$$

$$\overline{u}_y(\overline{y}, \overline{z}) = 0, \tag{63b}$$

$$\overline{u}_z(\overline{y}, \overline{z}) = 0. \tag{63c}$$

The LBM simulation of the NSEs to solve the Poiseuille duct flow problem, given by Eqs. (63), has been addressed in many previous publications.[64,67,75,84,87,88] While those works focused on demonstrating the second-order accuracy of the $\overline{u}_x$ solution predicted by the LBM with respect to its NSE counterpart, given by Eq. (63a), they overlooked the vanishing of the cross-flow field in the (y, z) plane, where the solutions are given by Eqs. (63b) and (63c). Even though satisfaction with such solutions might seem trivial, the work[75] showed that, when considering the non-linear velocity term in equilibrium, e.g., given by the E_q term in the TRT framework, then reduced cubic lattice models, such as the D3Q15 and D3Q19, yield non-zero cross-flow

velocity solutions $(\overline{u}_y, \overline{u}_z)$, regardless of how fine the mesh is. This contrasts with the D3Q27 model, which yields the correct $(\overline{u}_y, \overline{u}_z)$ solutions. Such a behavior was originally attributed to the lack of rotational invariance of the truncation errors in the reduced lattice schemes.[75] Subsequently, it was demonstrated[77,78] that certain amendments to the discrete equilibrium of the D3Q19 model could be made in order to guarantee that the LBM solutions of the NSEs on this lattice model could maintain rotational invariance.

Based on both theoretical and numerical analyses, the goal of the next two sections is to demonstrate: (1) how the D3Q19 lack of rotational invariance leads to distortions in the LBM solution of the $(\overline{u}_y, \overline{u}_z)$ field and (2) how an improved equilibrium for the D3Q19 is able to correct this issue and recover the proper advection flow patterns, in line with the theoretically expected solutions of the weakly rotating flow regime.

B. Lattice Boltzmann formulation—fourth-order expansion analysis

This section presents a comprehensive theoretical assessment of the LBM simulation of rotating duct flows. The study consists of a truncation error analysis based on the steady-state Chapman–Enskog fourth-order expansion.[44,78] Details on the main derivation steps are provided in Appendix E. In consistency with Sec. III B, we consider for the metric of the truncation error analysis the smallness parameter $\epsilon = \frac{1}{H}$, with H the number of computational cells of unitary size. According to this definition ϵ quantifies the effect of the mesh size on the numerical approximation, which will be accounted for up to $\mathcal{O}(\epsilon^4)$. On this basis, the LBM fourth-order approximation to the problem is governed by Eqs. (61) may be rewritten as follows:

$$\partial_{\overline{y}}\overline{u}_y + \partial_{\overline{z}}\overline{u}_z = \epsilon^2\,\mathrm{TE}_{\mathrm{Poisson}} + \epsilon^2\,\mathrm{TE}_{\mathrm{Solenoidal}} + \mathcal{O}(\epsilon^4), \tag{64a}$$

$$\partial_{\overline{y}}(\overline{u}_x\overline{u}_y) + \partial_{\overline{z}}(\overline{u}_x\overline{u}_z) = \overline{a}_x + \mathrm{Re}^{-1}\left(\partial_{\overline{y}\overline{y}}\overline{u}_x + \partial_{\overline{z}\overline{z}}\overline{u}_x\right) + 2\,\frac{\mathrm{Ek}}{\mathrm{Re}}\,\overline{u}_y + \epsilon^2\,(\mathrm{TE}_{\mathrm{Coriolis}})_x + \epsilon^2\,(\mathrm{TE}_{\mathrm{Advection}})_x + \epsilon^2\,(\mathrm{TE}_{\mathrm{Diffusion}})_x + \mathcal{O}(\epsilon^4), \tag{64b}$$

$$\begin{aligned}\partial_{\overline{y}}(\overline{u}_y^2) + \partial_{\overline{z}}(\overline{u}_y\overline{u}_z) = {} & -\partial_{\overline{y}}\overline{P} + \mathrm{Re}^{-1}\left(\partial_{\overline{y}\overline{y}}\overline{u}_y + \partial_{\overline{z}\overline{z}}\overline{u}_y + 2\,\partial_{\overline{y}}(\partial_{\overline{y}}\overline{u}_y + \partial_{\overline{z}}\overline{u}_z)\right) - 2\,\frac{\mathrm{Ek}}{\mathrm{Re}}\,\overline{u}_x \\ & + \epsilon^2\,(\mathrm{TE}_{\mathrm{Coriolis}})_y + \epsilon^2\,(\mathrm{TE}_{\mathrm{Advection}})_y + \epsilon^2\,(\mathrm{TE}_{\mathrm{Diffusion}})_y + \mathcal{O}(\epsilon^4),\end{aligned} \tag{64c}$$

$$\begin{aligned}\partial_{\overline{y}}(\overline{u}_y\overline{u}_z) + \partial_{\overline{z}}(\overline{u}_z^2) = {} & -\partial_{\overline{z}}\overline{P} + \mathrm{Re}^{-1}\left(\partial_{\overline{y}\overline{y}}\overline{u}_z + \partial_{\overline{z}\overline{z}}\overline{u}_z + 2\,\partial_{\overline{z}}(\partial_{\overline{y}}\overline{u}_y + \partial_{\overline{z}}\overline{u}_z)\right) + \epsilon^2\,(\mathrm{TE}_{\mathrm{Coriolis}})_z \\ & + \epsilon^2\,(\mathrm{TE}_{\mathrm{Advection}})_z + \epsilon^2\,(\mathrm{TE}_{\mathrm{Diffusion}})_z + \mathcal{O}(\epsilon^4),\end{aligned} \tag{64d}$$

where the TE symbol denotes the truncation error terms in the numerical approximation; their meaning is summarized in Table IX.

1. D3Q19-SE

Consider the case of the D3Q19 lattice with the standard quadratic equilibrium, named D3Q19-SE, which was described in Sec. II B. Starting from the derivations presented in Subsection 1 of Appendix E, and then properly non-dimensionalizing them, we obtain for each of the truncation error terms in the fourth-order approximation of the D3Q19-SE model the results given below.

- Mass balance equation [Eq. (64a)]

$$\mathrm{TE}_{\mathrm{Poisson}} = \frac{\Lambda}{3}\,\mathrm{Re}\left(\left(\partial_{\overline{y}\overline{y}}\overline{P} + \partial_{\overline{z}\overline{z}}\overline{P}\right) + \left(\partial_{\overline{y}\overline{y}}\overline{u}_y^2 + \partial_{\overline{z}\overline{z}}\overline{u}_z^2 + 2\,\partial_{\overline{y}\overline{z}}(\overline{u}_y\overline{u}_z)\right) + 2\,\frac{\mathrm{Ek}}{\mathrm{Re}}\,\partial_{\overline{y}}\overline{u}_x\right), \tag{65a}$$

$$\mathrm{TE}_{\mathrm{Solenoidal}} = -\left(\Lambda - \frac{1}{12}\right)\left(\partial_{\overline{y}\overline{y}\overline{y}}\overline{u}_y + \partial_{\overline{z}\overline{z}\overline{z}}\overline{u}_z + \partial_{\overline{y}\overline{z}\overline{z}}(\overline{u}_y + \overline{u}_z)\right). \tag{65b}$$

- Momentum balance equation along x direction [Eq. (64b)]

$$(\mathrm{TE}_{\mathrm{Coriolis}})_x = \frac{2}{3}\frac{\Lambda}{\mathrm{Re}}\,\mathrm{Ek}\left(\partial_{\overline{y}\overline{y}}\overline{u}_y + \partial_{\overline{z}\overline{z}}\overline{u}_y\right), \tag{66a}$$

TABLE IX. Definition of truncation error terms in Eqs. (64), where $i = \{x, y, z\}$.

Symbol	Definition
$\mathrm{TE}_{\mathrm{Poisson}}$	Truncation error taking the form of the pressure **Poisson** condition in the mass balance equation
$\mathrm{TE}_{\mathrm{Solenoidal}}$	Leading order truncation error to the **solenoidal** velocity condition in the mass balance equation
$(\mathrm{TE}_{\mathrm{Coriolis}})_i$	Leading order truncation error of the **Coriolis** force term in momentum balance equation along i
$(\mathrm{TE}_{\mathrm{Advection}})_i$	Leading order truncation error of the non-linear **advection** term in momentum balance equation along i
$(\mathrm{TE}_{\mathrm{Diffusion}})_i$	Leading order truncation error of the viscous **diffusion** term in momentum balance equation along i

$$(\mathrm{TE}_{\mathrm{Advection}})_x = -\left(\Lambda - \frac{1}{12}\right)\left(\partial_{\overline{y}\overline{y}\overline{y}}(\overline{u}_x\overline{u}_y) + \partial_{\overline{z}\overline{z}\overline{z}}(\overline{u}_x\overline{u}_z)\right), \tag{66b}$$

$$(\mathrm{TE}_{\mathrm{Diffusion}})_x = \left(\Lambda - \frac{1}{6}\right)\mathrm{Re}^{-1}\left(\partial_{\overline{y}\overline{y}\overline{y}\overline{y}}\overline{u}_x + \partial_{\overline{z}\overline{z}\overline{z}\overline{z}}\overline{u}_x\right). \tag{66c}$$

- Momentum balance equation along y direction [Eq. (64c)]

$$(\mathrm{TE}_{\mathrm{Coriolis}})_y = -\frac{2\,\Lambda}{3}\frac{\mathrm{Ek}}{\mathrm{Re}}\left(\partial_{\overline{y}\overline{y}}\overline{u}_x + \partial_{\overline{z}\overline{z}}\overline{u}_x + 2\,\partial_{\overline{y}\overline{y}}\overline{u}_x\right), \tag{67a}$$

$$(\mathrm{TE}_{\mathrm{Advection}})_y = -\left(\Lambda - \frac{1}{12}\right)\left(\partial_{\overline{y}}\left(\partial_{\overline{y}\overline{y}}\overline{P} + \partial_{\overline{z}\overline{z}}\overline{P}\right) + \partial_{\overline{y}\overline{y}\overline{y}}(\overline{u}_y^2) + \partial_{\overline{z}\overline{z}\overline{z}}(\overline{u}_y\overline{u}_z) + 3\,\partial_{\overline{y}\overline{y}\overline{z}}(\overline{u}_y\overline{u}_z) + \partial_{\overline{y}\overline{z}\overline{z}}(\overline{u}_y^2) + \partial_{\overline{y}\overline{z}\overline{z}}(\overline{u}_z^2) - \frac{\mathbf{1}}{\mathbf{2}}\boldsymbol{\partial}_{\overline{y}\overline{z}\overline{z}}(\overline{\boldsymbol{u}}_{\boldsymbol{x}}^{\mathbf{2}})\right), \tag{67b}$$

$$(\mathrm{TE}_{\mathrm{Diffusion}})_y = \left(\Lambda - \frac{1}{6}\right)\mathrm{Re}^{-1}\left(3\,\partial_{\overline{y}\overline{y}\overline{y}\overline{y}}\overline{u}_y + \partial_{\overline{z}\overline{z}\overline{z}\overline{z}}\overline{u}_y + 6\,\partial_{\overline{y}\overline{y}\overline{z}\overline{z}}\overline{u}_y + 4\,\partial_{\overline{y}\overline{z}}\left(\partial_{\overline{y}\overline{y}}\overline{u}_z + \partial_{\overline{z}\overline{z}}\overline{u}_z\right)\right). \tag{67c}$$

- Momentum balance equation along z direction [Eq. (64d)]

$$(\mathrm{TE}_{\mathrm{Coriolis}})_z = -\frac{4\,\Lambda}{3}\frac{\mathrm{Ek}}{\mathrm{Re}}\,\partial_{\overline{y}\overline{z}}\overline{u}_x, \tag{68a}$$

$$(\mathrm{TE}_{\mathrm{Advection}})_z = -\left(\Lambda - \frac{1}{12}\right)\left(\partial_{\overline{z}}\left(\partial_{\overline{y}\overline{y}}\overline{P} + \partial_{\overline{z}\overline{z}}\overline{P}\right) + \partial_{\overline{y}\overline{y}\overline{y}}(\overline{u}_y\overline{u}_z) + \partial_{\overline{z}\overline{z}\overline{z}}(\overline{u}_z^2) + 3\,\partial_{\overline{y}\overline{z}\overline{z}}(\overline{u}_y\overline{u}_z) + \partial_{\overline{y}\overline{y}\overline{z}}(\overline{u}_y^2) + \partial_{\overline{y}\overline{y}\overline{z}}(\overline{u}_z^2) - \frac{\mathbf{1}}{\mathbf{2}}\boldsymbol{\partial}_{\overline{y}\overline{y}\overline{z}}(\overline{\boldsymbol{u}}_{\boldsymbol{x}}^{\mathbf{2}})\right), \tag{68b}$$

$$(\mathrm{TE}_{\mathrm{Diffusion}})_z = \left(\Lambda - \frac{1}{6}\right)\mathrm{Re}^{-1}\left(\partial_{\overline{y}\overline{y}\overline{y}\overline{y}}\overline{u}_z + 3\,\partial_{\overline{z}\overline{z}\overline{z}\overline{z}}\overline{u}_z + 6\,\partial_{\overline{y}\overline{y}\overline{z}\overline{z}}\overline{u}_z + 4\,\partial_{\overline{y}\overline{z}}\left(\partial_{\overline{y}\overline{y}}\overline{u}_y + \partial_{\overline{z}\overline{z}}\overline{u}_y\right)\right). \tag{68c}$$

The terms highlighted in bold appear in Eqs. (67b) and (68b), namely, $\frac{1}{2}\partial_{\overline{y}\overline{z}\overline{z}}(\overline{u}_x^2)$ and $\frac{1}{2}\partial_{\overline{y}\overline{y}\overline{z}}(\overline{u}_x^2)$, are specific to the D3Q19-SE model. As will be discussed next, these terms are responsible for the breakdown of the rotational invariance of the numerical scheme whenever $\mathrm{Re} \neq 0$.

First, let us put aside the rotation effect, i.e., $\mathrm{Ek} = 0$. In this case, the only momentum sources acting along the transverse flow direction come from the $\mathcal{O}(\epsilon^2)$ terms $\frac{1}{2}\partial_{\overline{y}\overline{z}\overline{z}}(\overline{u}_x^2)$ and $\frac{1}{2}\partial_{\overline{y}\overline{y}\overline{z}}(\overline{u}_x^2)$ in Eqs. (67b) and (68b). Since these terms arise from the D3Q19-SE model's lack of isotropy, it is obvious that the secondary flow field generated by them is unphysical. Figure 15 quantifies the impact of these unphysical source terms on the main and secondary flow solutions. The streamlined structure generated by them is also illustrated in Fig. 16. As shown in a previous work[78] and further confirmed here, see Fig. 15, the relative magnitude of the spurious currents can be quantified by $\max(u_y, u_z)/\max(u_x)$ and this metric decreases quadratically with the mesh refinement as $\mathcal{O}(\epsilon^2)$, except when $\Lambda = \frac{1}{12}$ where the spurious effect decreases quartically as $\mathcal{O}(\epsilon^4)$. These observations are in line with the truncation error analysis shown above, namely on the scaling of the $(\mathrm{TE}_{\mathrm{Advection}})_y$ and $(\mathrm{TE}_{\mathrm{Advection}})_z$ terms displayed in Eqs. (67b) and (68b).

Second, let us add the effect of rotation to the flow field, i.e., $\mathrm{Ek} > 0$, while holding $\mathrm{Re} \sim \mathcal{O}(1)$ fixed. In this case, two momentum sources will act in competition: (1) the (physical) Coriolis force term, which scales with Ek/Re; and (2) the above reported (unphysical) numerical anisotropy force terms, coming from $(\mathrm{TE}_{\mathrm{Advection}})_y$ and $(\mathrm{TE}_{\mathrm{Advection}})_z$, which scale with $\mathcal{O}(\epsilon^2)$. In the weakly rotating flow regime, we typically have $\mathcal{O}(\mathrm{Ek}/\mathrm{Re}) \ll \mathcal{O}(\epsilon^2)$ so that the (physical) Coriolis force effect becomes completely overshadowed by the (unphysical) spurious currents generated by the $(\mathrm{TE}_{\mathrm{Advection}})_y$ and $(\mathrm{TE}_{\mathrm{Advection}})_z$ anisotropic corrections. This conclusion is supported by the similarity between the Ek = 0 solution, depicted in Fig. 16, and the

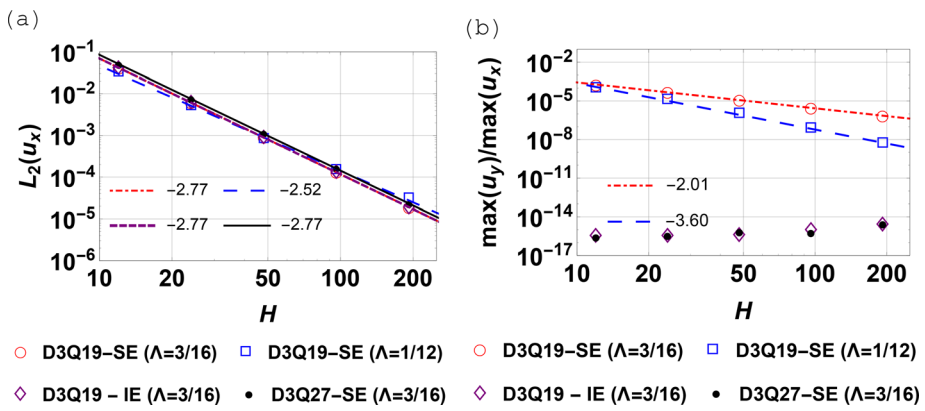

FIG. 15. Mesh convergence analysis of the TRT simulations performed on a square duct Poiseuille NSE flow in a non-rotating setup with BB no-slip walls. Physical regime: Ek = 0 and Re = 10. Panel (a) Accuracy in the main flow direction [reference solution: Eq. (63a)]. Panel (b) Accuracy in the cross flow direction [reference solution: Eq. (63b)].

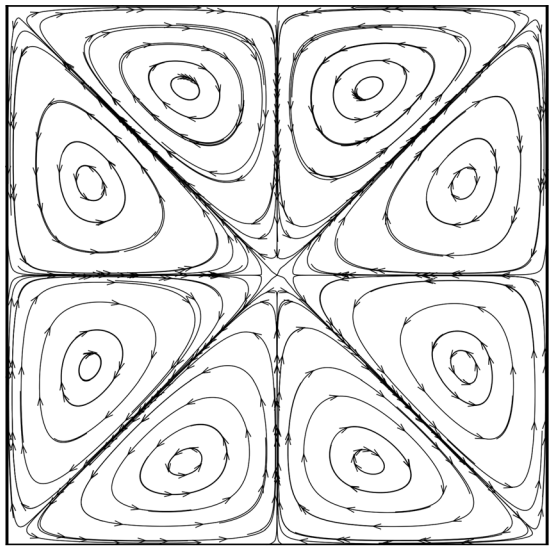

Ek/Re = 0

FIG. 16. Streamlines along (y, z) plane of the unphysical cross flow (u_y, u_x) generated by the D3Q19-SE scheme in the simulation of the square duct Poiseuille NSE flow in a non-rotating setup with BB no-slip walls. Physical regime: Ek = 0 and Re = 10. Numerical parameters: $H = 60$ and $\Lambda = 3/16$. Magnitude of secondary vs main flow fields: $\max(u_y, u_z)/\max(u_x) = 7.5 \times 10^{-6}$.

finite $\mathcal{O}(\mathrm{Ek/Re}) \ll \mathcal{O}(\epsilon^2)$ solution, depicted in Fig. 17(a). At moderate values within the weakly rotating flow regime, i.e., when $\mathcal{O}(\mathrm{Ek/Re}) \approx \mathcal{O}(\epsilon^2)$, the aforementioned two momentum source terms act on an equal footing. The competition between them leads to very exotic but unphysical flow patterns. This case is illustrated in Figs. 17(b) and 17(c). Only at larger rotation values within the weakly rotating flow regime, i.e., when $\mathcal{O}(\mathrm{Ek/Re}) \gg \mathcal{O}(\epsilon^2)$, the numerical solution starts approaching the physically expected solution. However, even in this case, the solution remains contaminated by minor distortions, as confirmed in Fig. 17(d).

2. D3Q19-IE

Now, we consider the solution of the same problem, but employing the D3Q19 lattice with the improved quadratic equilibrium, named D3Q19-IE, and expressed by Eq. (17) given in Sec. II D. Then, by redoing the derivations presented in Subsection 1 of Appendix E, with the information provided in Table X, we arrive at the conclusion that the fourth-order expansion of the LBM equations remains given by Eqs. (64), but without the terms in bold, i.e., $\frac{1}{2}\partial_{\overline{yzz}}(\overline{u}_x^2)$ and $\frac{1}{2}\partial_{\overline{yyz}}(\overline{u}_x^2)$ in Eqs. (67b) and (68b), which are removed. In Sec. IV C, it will be numerically confirmed that, owing to the absence of these sources of anisotropy, the corresponding D3Q19 lattice solution becomes free from the previously reported (unphysical) spurious currents.

3. D3Q27-SE

Finally, the same solution procedure is repeated, but this time for the D3Q27 lattice with the standard quadratic equilibrium, named D3Q27-SE, which was described in Sec. II B. Once again, starting from the derivations presented in Subsection 2 of Appendix E with the information provided in Table XI, and after proper non-dimensionalization, the LBM fourth-order approximation of the problem governed by Eqs. (61) is derived as follows.

- Mass balance equation [Eq. (64a)]

$$\mathrm{TE}_{\mathrm{Poisson}} = \frac{\Lambda}{3}\mathrm{Re}\left(\left(\partial_{\overline{yy}}\overline{P} + \partial_{\overline{zz}}\overline{P}\right) + \left(\partial_{\overline{yy}}\overline{u}_y^2 + \partial_{\overline{zz}}\overline{u}_z^2 + 2\,\partial_{\overline{yz}}(\overline{u}_y\overline{u}_z)\right) + 2\,\frac{\mathrm{Ek}}{\mathrm{Re}}\,\partial_{\overline{y}}\overline{u}_x\right), \tag{69a}$$

$$\mathrm{TE}_{\mathrm{Solenoidal}} = -\left(\Lambda - \frac{1}{12}\right)\left(\partial_{\overline{yyy}}\overline{u}_y + \partial_{\overline{zzz}}\overline{u}_z + \partial_{\overline{yzz}}(\overline{u}_y + \overline{u}_z)\right). \tag{69b}$$

- Momentum balance equation along x direction [Eq. (64b)]

$$(\mathrm{TE}_{\mathrm{Coriolis}})_x = \frac{2}{3}\frac{\Lambda}{\mathrm{Re}}\,\mathrm{Ek}\left(\partial_{\overline{yy}}\overline{u}_y + \partial_{\overline{zz}}\overline{u}_y\right), \tag{70a}$$

$$(\mathrm{TE}_{\mathrm{Advection}})_x = -\left(\Lambda - \frac{1}{12}\right)\left(\partial_{\overline{yyy}}(\overline{u}_x\overline{u}_y) + \partial_{\overline{zzz}}(\overline{u}_x\overline{u}_z) + \partial_{\overline{yyz}}(\overline{u}_x\overline{u}_z) + \partial_{\overline{yzz}}(\overline{u}_x\overline{u}_y)\right), \tag{70b}$$

$$(\mathrm{TE}_{\mathrm{Diffusion}})_x = \left(\Lambda - \frac{1}{6}\right)\mathrm{Re}^{-1}\left(\partial_{\overline{yyyy}}\overline{u}_x + \partial_{\overline{zzzz}}\overline{u}_x + 2\,\partial_{\overline{yyzz}}\overline{u}_x + \frac{4}{3}\,\partial_{\overline{yyyz}}\overline{u}_y + \frac{4}{3}\,\partial_{\overline{yzzz}}\overline{u}_z\right). \tag{70c}$$

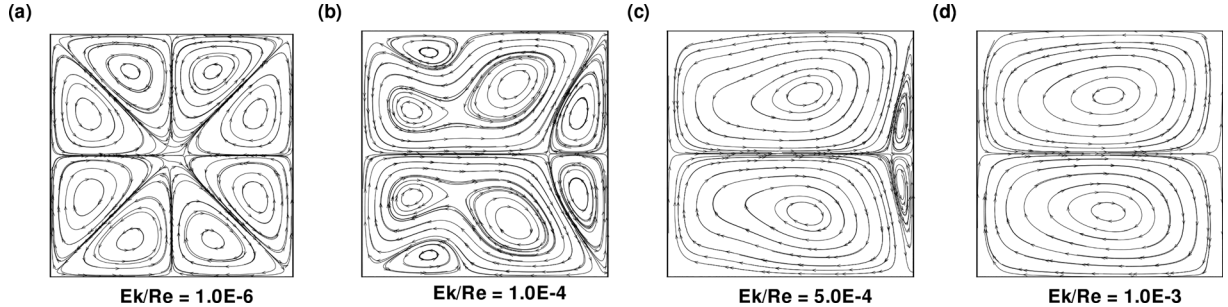

FIG. 17. Streamlines along (y, z) plane predicted by D3Q19-SE simulations at different Ek numbers and Re = 10 fixed, using BB no-slip walls with $\Lambda = 3/16$. (a) Ek = 0.00001 and $\max(u_y, u_z)/\max(u_x) = 7.5 \times 10^{-6}$. (b) Ek = 0.001 and $\max(u_y, u_z)/\max(u_x) = 9.0 \times 10^{-6}$. (c) Ek = 0.005 and $\max(u_y, u_z)/\max(u_x) = 2.0 \times 10^{-5}$. (d) Ek = 0.01 and $\max(u_y, u_z)/\max(u_x) = 3.3 \times 10^{-5}$.

- Momentum balance equation along y direction [Eq. (64c)]

$$(\mathrm{TE}_{\mathrm{Coriolis}})_y = -\frac{2\,\Lambda}{3}\frac{\mathrm{Ek}}{\mathrm{Re}}\left(\partial_{\overline{y}\overline{y}}\overline{u}_x + \partial_{\overline{z}\overline{z}}\overline{u}_x + 2\,\partial_{\overline{y}\overline{y}}\overline{u}_x\right), \tag{71a}$$

$$(\mathrm{TE}_{\mathrm{Advection}})_y = -\left(\Lambda - \frac{1}{12}\right)\left(\partial_{\overline{y}}\left(\partial_{\overline{y}\overline{y}}\overline{P} + \partial_{\overline{z}\overline{z}}\overline{P}\right) + \partial_{\overline{y}\overline{y}\overline{y}}(\overline{u}_y^2) + \partial_{\overline{z}\overline{z}\overline{z}}(\overline{u}_y\overline{u}_z) + 3\,\partial_{\overline{y}\overline{y}\overline{z}}(\overline{u}_y\overline{u}_z) + \partial_{\overline{y}\overline{z}\overline{z}}(\overline{u}_y^2) + \partial_{\overline{y}\overline{z}\overline{z}}(\overline{u}_z^2)\right), \tag{71b}$$

$$(\mathrm{TE}_{\mathrm{Diffusion}})_y = \left(\Lambda - \frac{1}{6}\right)\mathrm{Re}^{-1}\left(3\,\partial_{\overline{y}\overline{y}\overline{y}\overline{y}}\overline{u}_y + \partial_{\overline{z}\overline{z}\overline{z}\overline{z}}\overline{u}_y + 6\,\partial_{\overline{y}\overline{y}\overline{z}\overline{z}}\overline{u}_y + 4\,\partial_{\overline{y}\overline{z}}\left(\partial_{\overline{y}\overline{y}}\overline{u}_z + \partial_{\overline{z}\overline{z}}\overline{u}_z\right)\right). \tag{71c}$$

- Momentum balance equation along z direction [Eq. (64d)]

$$(\mathrm{TE}_{\mathrm{Coriolis}})_z = -\frac{4\,\Lambda}{3}\frac{\mathrm{Ek}}{\mathrm{Re}}\,\partial_{\overline{y}\overline{z}}\overline{u}_x, \tag{72a}$$

$$(\mathrm{TE}_{\mathrm{Advection}})_z = -\left(\Lambda - \frac{1}{12}\right)\left(\partial_{\overline{z}}\left(\partial_{\overline{y}\overline{y}}\overline{P} + \partial_{\overline{z}\overline{z}}\overline{P}\right) + \partial_{\overline{y}\overline{y}\overline{y}}(\overline{u}_y\overline{u}_z) + \partial_{\overline{z}\overline{z}\overline{z}}(\overline{u}_z^2) + 3\,\partial_{\overline{y}\overline{z}\overline{z}}(\overline{u}_y\overline{u}_z) + \partial_{\overline{y}\overline{y}\overline{z}}(\overline{u}_y^2) + \partial_{\overline{y}\overline{y}\overline{z}}(\overline{u}_z^2)\right), \tag{72b}$$

$$(\mathrm{TE}_{\mathrm{Diffusion}})_z = \left(\Lambda - \frac{1}{6}\right)\mathrm{Re}^{-1}\left(\partial_{\overline{y}\overline{y}\overline{y}\overline{y}}\overline{u}_z + 3\,\partial_{\overline{z}\overline{z}\overline{z}\overline{z}}\overline{u}_z + 6\,\partial_{\overline{y}\overline{y}\overline{z}\overline{z}}\overline{u}_z + 4\,\partial_{\overline{y}\overline{z}}\left(\partial_{\overline{y}\overline{y}}\overline{u}_y + \partial_{\overline{z}\overline{z}}\overline{u}_y\right)\right). \tag{72c}$$

The comparison of the TE terms indicates that, with the exception of the momentum balance equation along the x direction, i.e., Eq. (66c) vs Eq. (70c), the remaining macroscopic equations recovered by the D3Q19 lattice with the improved equilibrium (D3Q19-IE) and the D3Q27 lattice with standard equilibrium (D3Q27-SE) are identical, up to $\mathcal{O}(\epsilon^4)$ accuracy. In both cases, the sources of anisotropy in the momentum balance conditions are absent, which permits recovering cross-flow velocity patterns free from the (unphysical) spurious currents.

C. Numerical tests

This section contains numerical support for the truncation error analysis previously presented in Sec. IV B. The rotating duct flow problem, formulated in Sec. IV A, is here simulated through two strategies: (1) the TRT model, using D3Q19-SE, D3Q19-IE, and D3Q27-SE schemes, and (2) the FEM, using linear interpolation functions on uniform Cartesian meshes. For brevity, all LBM results shown here, which refer to Fig. 15 up to Fig. 19, employ BB boundaries only. Other LBM boundary schemes, such as the LSOB wet node boundary, were also tested and confirmed to produce similar observations. Periodic boundary conditions are considered along the main flow direction. In terms of discretization, the square channel cross section is covered by $H \times H$ computational cells of square shape and unitary length. Grid nodes in LBM are cell centered, e.g., $z_j = -\frac{H}{2} + \frac{1}{2} + j$ $(j = 0, 1, \ldots, H-1)$, and in FEM are located at cell vertices, e.g., $z_j = -\frac{H}{2} + j$ $(j = 0, 1, \ldots, H)$. Both schemes adopt the same initialization routine, set by a uniform pressure and zero velocity field. In LBM, the traditional stream-and-collide time evolution is employed until meeting the steady-state convergence criterion $|\langle u_x\rangle(t)/\langle u_x\rangle(t-100) - 1| \leq 10^{-12}$. In FEM, the solution procedure operates with the GMRES iterative solver (without any preconditioner), and the steady-state stopping criterion checks whether its relative residual has become less than a prescribed tolerance, set as 10^{-12}.

1. Non-rotating duct flow

This test case corresponds to the NSE Poiseuille flow solution in a square duct, governed by Eq. (63). The main flow solution is given by Eq. (63a) and the cross flow solution has zero velocity and is given by Eqs. (63b) and (63c).

Figure 15(a) displays the $\mathrm{L}_2(u_x)$ error evolution as a function of the mesh refinement $H = \{12, 24, 48, 96, 192\}$, where H determines the number of computational cells along an edge of the channel square cross section. As expected, second-order convergence is supported by all schemes, namely D3Q19-SE, D3Q19-IE, and D3Q27-SE. Quantitatively, D3Q19-SE and D3Q19-IE have a similar $\mathrm{L}_2(u_x)$ accuracy, which is slightly better than the D3Q27-SE accuracy. The difference lies in the structure of the $\mathcal{O}(\epsilon^2)$ truncations featuring in the x-momentum balance equation, namely the $\mathcal{O}(\epsilon^2)$ viscous correction in the D3Q19 lattice [Eq. (66c)] is less dissipative than in the D3Q27 lattice [Eq. (70c)].

Figure 15(b) displays the evolution of the metric $\max(u_y)/\max(u_x)$ for the simulations depicted in Fig. 15(a). Theoretically, the result of this metric should be zero (within machine accuracy). However, only the D3Q27-SE and D3Q19-IE schemes yield the physical solution. The D3Q19-SE recovers non-zero (u_y, u_z) velocities, which decrease quadratically with the mesh resolution, except for $\Lambda = 1/12$ where a quartic decrease is observed. These error decreasing rates are in agreement with the truncation error analysis developed in Sec. IV B. Figure 16 depicts the streamlines of the cross flow artificially generated by the D3Q19-SE scheme. Repeating these simulations with the Stokes equilibrium, i.e., by setting $E_q = 0$ in e_q^+, then the unphysical flow patterns here reported are absent, which further confirms the source of the identified errors.

2. Rotating duct flow

This test case considers the same duct flow problem, but now subject to rotation, which is governed by Eqs. (61) and the geometry setup is depicted in Fig. 14(a). In the problem discretization, both LBM and FEM employ $H = 60$ computational cells along the edge of the channel square cross section. Furthermore, TRT simulations are run with $\Lambda = 3/16$ fixed. Simulations are run for $\mathrm{Re} = 10$ fixed (slow laminar regime) while the effect of rotation is tested over the range

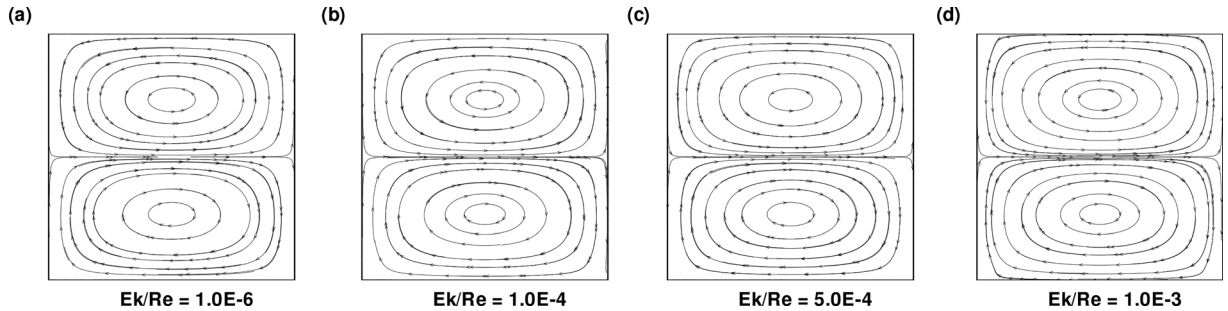

FIG. 18. Streamlines along (y, z) plane predicted by D3Q19-IE simulations at different Ek numbers and Re = 10 fixed, using BB no-slip walls with $\Lambda = 3/16$. (a) Ek = 0.00001 and $\max(u_y, u_z)/\max(u_x) = 5.8 \times 10^{-8}$. (b) Ek = 0.001 and $\max(u_y, u_z)/\max(u_x) = 5.8 \times 10^{-6}$. (c) Ek = 0.005 and $\max(u_y, u_z)/\max(u_x) = 2.9 \times 10^{-5}$. (d) Ek = 0.01 and $\max(u_y, u_z)/\max(u_x) = 5.8 \times 10^{-5}$.

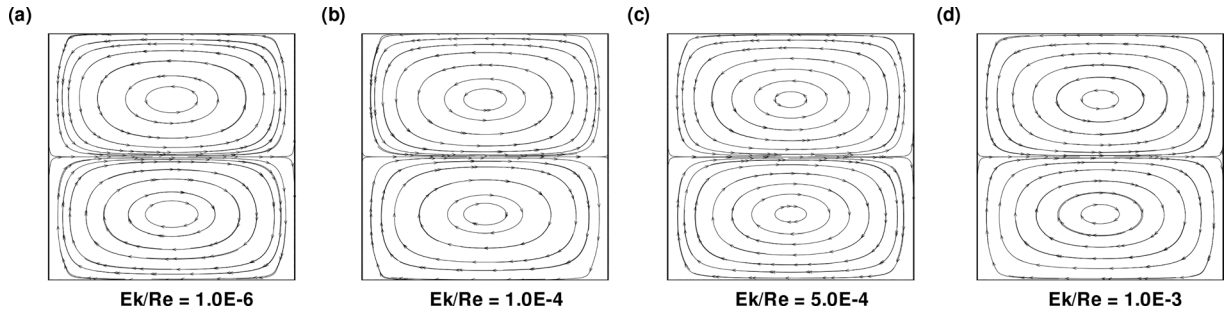

FIG. 19. Streamlines along (y, z) plane predicted by D3Q27-SE simulations at different Ek numbers and Re = 10 fixed, using BB no-slip walls with $\Lambda = 3/16$. (a) Ek = 0.00001 and $\max(u_y, u_z)/\max(u_x) = 5.8 \times 10^{-8}$. (b) Ek = 0.001 and $\max(u_y, u_z)/\max(u_x) = 5.8 \times 10^{-6}$. (c) Ek = 0.005 and $\max(u_y, u_z)/\max(u_x) = 2.9 \times 10^{-5}$. (d) Ek = 0.01 and $\max(u_y, u_z)/\max(u_x) = 5.8 \times 10^{-5}$.

Ek $\leq$ 0.01, which corresponds to Ek/Re $\leq$ 0.001. As noted in Sec. IV A, the individual values of Re and Ek may be varied so that the structure of solutions will remain unchanged, providing the flow solution holds within the weakly rotating regime. This behavior is known as the "*asymptotic invariance property*."[86] Even though we only display the assessment of this property through varying the Ek number, we emphasize that similar conclusions are obtained (although not shown here) when varying Re providing, of course, that the solution remains within the weakly rotating regime.

Figures 17–20 display the streamline solutions of the cross-flow patterns produced by, respectively, D3Q19-SE, D3Q19-IE, D3Q27-SE, and FEM, covering the following values: Ek $\leq$ 0.01 and Re = 10 fixed. The inspection of these figures reveals that, with the exception of the D3Q19-SE scheme, depicted in Fig. 17, all remaining schemes (D3Q19-IE, D3Q27-SE, and FEM) invariably predict the same type of two-cell cross-flow patterns, providing they pertain to the range Ek/Re $\leq$ 0.001. These results are in line with the asymptotic invariance property characteristic of the weakly rotating regime.[7,9–11,86]

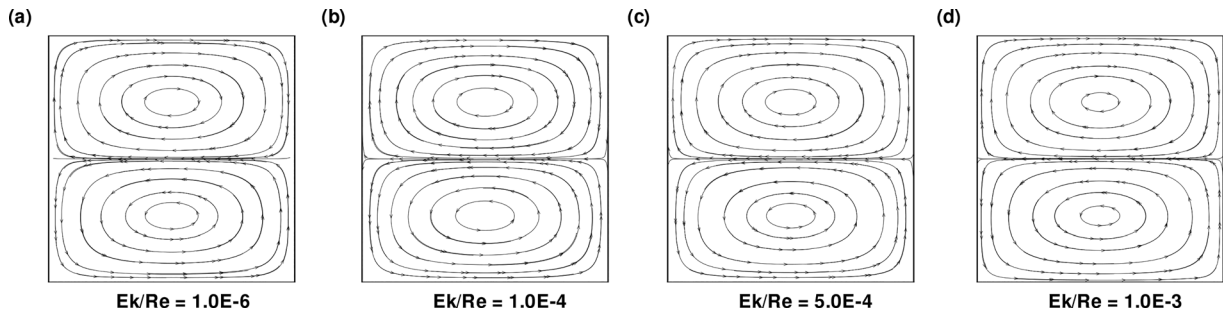

FIG. 20. Streamlines along (y, z) plane predicted by FEM simulations at different Ek numbers and Re = 10 fixed with $\Lambda = 3/16$. (a) Ek = 0.00001 and $\max(u_y, u_z)/\max(u_x) = 5.2 \times 10^{-8}$. (b) Ek = 0.001 and $\max(u_y, u_z)/\max(u_x) = 5.2 \times 10^{-6}$. (c) Ek = 0.005 and $\max(u_y, u_z)/\max(u_x) = 2.6 \times 10^{-5}$. (d) Ek = 0.01 and $\max(u_y, u_z)/\max(u_x) = 5.2 \times 10^{-5}$.

The violation of this invariance property condition renders the D3Q19-SE solutions unphysical and casts doubt on previous LBM studies tackling this problem class while using the D3Q19-SE model. For example, the work by Zhang *et al.*[31] attributed to the solutions shown in Fig. 17 the discovery of a new physical regime. However, as shown in this work, these multiple cell patterns are, in reality, numerically generated artifacts introduced by the anisotropic structure of the truncation error terms[75] supported by the D3Q19-SE model. A more detailed explanation of the root of these unphysical patterns, which arise from the interplay between physical and unphysical terms, can be found in Sec. IV B.

V. CONCLUSIONS

The present work examined the LBM modeling of rotating channel flows. While this problem constitutes a fundamental building block of many scientific and engineering applications, its accurate numerical modeling remains a challenging task, as unveiled throughout this manuscript.

For the LBM model, the two-relaxation-time (TRT) collision operator[40–42] was chosen for its ability to support the parametrization of steady solutions in agreement with the principle of dimensional similarity, a principle that should guide the scaling of any physical law and, consequently, the solution structure of any numerical scheme. It turns out that this consistency requirement is violated by single-relaxation-time collision models, such as the BGK[46] or the Regularized[88] models. This work proposed formulating the elements within the TRT framework, namely the equilibrium and source terms, as projections onto a series of Hermite tensor polynomials $\mathcal{H}^{(n)}$. The adoption of this theoretical perspective allows us to reinterpret previously known results as follows:

- The standard NSE equilibrium, based on a second-order expansion in velocity space, when formulated into the TRT framework decomposes e_q into symmetric and anti-symmetric components. The symmetrical part e_q^+ deals with the projection of the macroscopic variables of interest onto both $\mathcal{H}^{(0)}$ and $\mathcal{H}^{(2)}$ bases while the anti-symmetrical part e_q^- only considers the projection onto the $\mathcal{H}^{(1)}$ basis.
- The LBM source term describes an external momentum source, i.e., an external body force, and follows a similar decomposition. The anti-symmetric component F_q projects the macroscopic body force onto the $\mathcal{H}^{(1)}$ basis. The symmetric part S_q may include $\mathcal{H}^{(0)}$ projections if an external mass source is present, but this possibility is excluded here. The so-called Guo forcing model[26] considers the additional S_q component as a projection onto the $\mathcal{H}^{(2)}$ basis. However, as demonstrated in previous works[49–52] and also proven in Appendix A of the current manuscript, consistency demands the symmetric component S_q to be zero; otherwise, the aforementioned similarity property of the TRT steady state will breakdown[52] and spurious terms will appear in the steady solutions, regardless of the collision model adopted.

Through careful examination of selected rotating channel flow problems modeled with the TRT scheme, the impact of the equilibrium and source terms, e_q and F_q, was assessed and strategies to improve their solution accuracy were proposed. This study allowed us to draw the following two main conclusions:

- The LBM modeling of a velocity-dependent source term inevitably brings in unphysical velocity Laplacian terms, at the discrete level, within the momentum balance equations. These discretization errors are found to be similar in form to the physical viscous diffusion terms. Hence, to avoid any potential interference between them, we suggested in Sec. II E to operate with an improved source model, $F_q^{(\star)}$, which supplements the standard formulation of F_q with the inclusion of an extra correction term that features projections of the macroscopic body force onto the $\mathcal{H}^{(3)}$ basis. This additional source correction does not act at hydrodynamic level but permits canceling or, at least, to mitigate the undesirable discretization artifacts that are introduced by the source term at a higher order. By examining the LBM exact solution of a Poiseuille–Ekman rotating channel flow, thoroughly discussed in Sec. III and Appendix C, this strategy was confirmed to effectively improve the accuracy with the external momentum source (featuring the Coriolis force) in the dynamics of rotating flows.
- The standard equilibrium used in the LBM modeling of the isothermal NSEs is typically built on a second-order Hermite expansion of the continuous Maxwell–Boltzmann equilibrium. Although the non-linear velocity part of this equilibrium, E_q, when projected onto the $\mathcal{H}^{(2)}$ basis, holds the full isotropic structure of the continuous equilibrium in the D3Q27 lattice, for the D3Q19 lattice the expected isotropy conditions are not met. This shortcoming impairs the isotropy of the truncation errors of the momentum advection terms supported by the D3Q19 lattice, making them angular dependent. These general observations are pinpointed in Appendix E. It turns out that this defect is particularly harmful in the simulation of flows pertaining to the weakly rotating regime, as illustrated in Sec. IV. In order to correct these anisotropy defects, Sec. II D proposed the usage of an improved equilibrium model $E_q^{(\star)}$ for the D3Q19 lattice, named the D3Q19-IE model, which considers projections of the non-linear velocity term onto the $\mathcal{H}^{(4)}$ basis, besides the $\mathcal{H}^{(2)}$ basis. By examining the LBM solution of a rotating duct flow problem in Sec. IV, it was confirmed that the proposed improved equilibrium $E_q^{(\star)}$ for the D3Q19 lattice effectively improves the accuracy of modeling of the momentum advection term, reaching the isotropy level of the D3Q27 model. Considering that the D3Q27 model requires about 42% more CPU time and storage than the D3Q19 model per lattice node, the attractiveness of the D3Q19-IE model is evident. By exploring this difference, one may be able to enlarge the scale of the trackable computational problems without sacrificing accuracy.

Alongside the aforementioned two main contributions, this work also discussed the operation of each family of LBM boundary schemes, the (off-node) linkwise and the (on-node) wet node strategies, and how accurately they accommodate the numerical solution of rotating fluid flows, particularly in under-resolved scenarios.

- The wet node strategy locates the boundary node at the wall. This places the grid nodes at the vertices of the computational cells. While the explicit enforcement of the BC at the boundary node may be more accurate in well-resolved simulations, when operating in under-resolved scenarios, the requirement to exactly satisfy the BC may act as an over-constraint and distort the bulk solution in the attempt to accommodate it. Finally, as LBM operates

on uniform Cartesian meshes, the wet node strategy considered here applies only for straight on-node boundaries, and its generalization to set the no-slip condition on arbitrarily shaped walls typically becomes more cumbersome to realize on regular grids.
- The linkwise strategy locates the physical boundary off-node, placing the wall some distance away from the boundary node. In this framework, it is preferable to consider the grid nodes at the centroid of the computational cells. With this strategy, the boundary condition is prescribed implicitly, as a truncated Taylor series, with coefficients dictating the distance between the wall and boundary node. With the exception of very particular polynomial flows (e.g., linear and parabolic flows), the boundary condition imposed may feature a certain degree of slip due to the unaccounted terms in the series approximation. However, when adopting higher-order linkwise strategies, such as the MLI or multireflection schemes,[41,43,45,61,62] this numerical slip becomes restricted to the effect of $\mathcal{O}(\epsilon^3)$ terms, making the slip phenomenon of very small magnitude in well-resolved simulations. On the other hand, in under-resolved simulations, the ability to have slip at walls tends to be a beneficial issue since it permits a smoother accommodation of the bulk solution toward the boundary. Finally, the linkwise operation principle permits describing, in a more natural way, wall-boundary shapes that do not align with the underlying mesh. In Sec. II F 2, this work proposed a revision of the parabolic accurate MLI boundary scheme, including an additional term to correct for specific artifacts that may be introduced at the boundary by the rotation modeling effect.

Finally, to establish this work on more general grounds, both LBM test cases considered in this study have been accompanied by FEM simulations. To establish fair comparisons with LBM, we considered a FEM numerical scheme with linear interpolation functions on uniform Cartesian meshes. This study permitted identifying differences and similarities between the LBM and the FEM modeling approaches when tackling this problem class. Most notably, for the modeling of the Poiseuille–Ekman rotating channel flow, it was found that the TRT, with $\Lambda = 1/8$, when using the SF scheme for the source term and the wet node at boundaries, exactly matches the discrete solution predicted by the linear FEM considered here. Such a finding is in agreement with previous studies.[55,56]

As future work, it is planned to extend this study toward the simulation of more complex geometries and flow regimes, which include the modeling of time-dependent effects and turbulent flows.[28–30] Also, since rotation has great utility in boosting the rates of many transport phenomena processes,[32,33] the LBM modeling of conjugate heat and mass transfer in problems subject to rotation is programmed as the next logical step in this study. In principle, a similar kind of numerical analysis to that developed herein must be applied to those problem classes in order to identify and correct the sort of numerical artifacts discussed in this work, which were found to individually affect the modeling of the diffusion and advection terms in the isothermal NSEs under rotation.

ACKNOWLEDGMENTS

This article is dedicated to the memory of Professor Viriato Semiao, a dear friend and mentor of G. Silva. G. Silva acknowledges Fundação para a Ciência e a Tecnologia (FCT) for its financial support via the project LAETA Base Funding (DOI:10.54499/UIDB/50022/2020), and Agenda Mobilizadora New Space Portugal (Ref. C644936537-00000046, Notice ACC02/CO5-i01/2022), funded by the Mobilising Agendas for Business Innovation through the Recovery and Resilience Programme (PRR).

AUTHOR DECLARATIONS

Conflict of Interest

The authors have no conflicts to disclose.

Author Contributions

Goncalo Silva: Conceptualization (equal); Formal analysis (equal); Investigation (equal); Methodology (equal); Resources (equal); Software (equal); Writing – original draft (equal); Writing – review & editing (equal). **Irina Ginzburg:** Formal analysis (equal); Methodology (equal); Writing – review & editing (supporting).

DATA AVAILABILITY

The data that support the findings of this study are available from the corresponding author upon reasonable request.

APPENDIX A: SECOND-ORDER SOURCE TERM: TRT FORMULATION AND INCONSISTENCY PROOF

1. TRT formulation

The LBM source term formulation, expanded up to second order in discrete velocity space, is popularized as the Guo forcing formulation.[26] The TRT representation of the Guo source model requires modifying the symmetrical part of the original equilibrium, Eq. (7), as follows:

$$e_q^+ = P_q + E_q + \Lambda^+ S_q, \tag{A1a}$$

$$e_q^- = j_q + \Lambda^- F_q. \tag{A1b}$$

Explicitly, the symmetric S_q and anti-symmetric F_q source contributions are given by

$$\begin{aligned} F_q &= t_q \mathcal{H}^{(1)}_{q\alpha} F_\alpha \\ &= t_q c_{q\alpha} F_{q\alpha}, \end{aligned} \tag{A2a}$$

$$\begin{aligned} S_q &= 3\, t_q \mathcal{H}^{(2)}_{q\alpha\beta} \frac{j_\alpha F_\beta}{\rho_0} \\ &= 3\, t_q \left(c_{q\alpha} c_{q\beta} - \frac{1}{3}\delta_{\alpha\beta} \right) \frac{j_\alpha F_\beta}{\rho_0}. \end{aligned} \tag{A2b}$$

2. Inconsistency proof

Consider the use of Eq. (A2) to represent the rotating force term given in Eq. (15), for a fixed Cartesian reference frame (x, y, z), takes the following explicit form:

$$F_q = t_q \left[c_{qx} (\rho_0 a_x + 2\,\Omega_z j_y) + c_{qy} (-2\,\Omega_z j_x) \right], \tag{A3a}$$

$$S_q = t_q\Bigg[(3\,c_{qx}^2-1)\left(a_x\,j_x+2\,\Omega_z\,\frac{j_y j_x}{\rho_0}\right)+3\,c_{qx}c_{qy}\left(a_x\,j_y+2\,\Omega_z\,\frac{j_y^2}{\rho_0}\right)$$
$$+3\,c_{qx}c_{qy}\left(-2\,\Omega_z\,\frac{j_x^2}{\rho_0}\right)+(3\,c_{qy}^2-1)\left(-2\,\Omega_z\,\frac{j_x j_y}{\rho_0}\right)\Bigg]. \tag{A3b}$$

In a previous work[51] the consistency of this second-order force formulation, Eq. (A2), to model rotating fluids was studied for a rotating channel Poiseuille flow. This case simplifies the macroscopic forcing in Eq. (15) to $F_x=\rho_0\,a_x$ and $F_y=-2\,\Omega_z\,j_x$. It turns out that, for this simple setup, it is already possible to verify that the inclusion of the symmetric source component S_q in the forcing formulation, makes the TRT scheme exactly equivalent to the following finite-difference equation along the x-momentum component:

$$\rho_0\,a_x+\frac{\Lambda^+}{3}\overline{\Delta}_z^2 j_x+\frac{2\,\Omega_z\,\Lambda^+}{\rho_0}\overline{\Delta}_z j_x^2=0. \tag{A4}$$

Above, the last term on the left-hand side of Eq. (A4) is unphysical. Its presence leads to many detrimental effects on the LBM steady solution, as reported in previous studies.[51,52] In this case, whenever Eq. (A2b) is used to describe the Coriolis force term, the identified unphysical quadratic velocity term in Eq. (A4), coming from the inadequacy of the second-order LBM source formulation, will have a negative impact on the LBM modeling of any kind of rotating flow problem.[27–39]

APPENDIX B: ALTERNATIVE REPRESENTATION OF THE NON-LINEAR EQUILIBRIA GIVEN IN SECS. II B AND II D

Sections II B and II D present the structure of the standard and improved equilibrium in terms of Hermite polynomials. While this notation is suitable from a theoretical analysis perspective, the computational implementation of the equilibrium term may follow a more convenient structure[77,78] which is also more computationally efficient.

Hence, the symmetrical component of the standard equilibrium term, named D3Q19-SE, which was originally presented in Eq. (8b), may be rewritten in compact form as

$$E_q=\frac{t_q}{2\rho_0}\begin{cases}-j_\alpha j_\alpha & \vec{c}_q=(0,0,0)\\ 3(c_{q\alpha}j_\alpha)^2-j_\alpha j_\alpha & \vec{c}_q\in\{(\pm1,0,0),(0,\pm1,0),(0,0,\pm1)\}\\ 3(c_{q\alpha}j_\alpha)^2-j_\alpha j_\alpha & \text{else.}\end{cases} \tag{B1}$$

Similarly, the symmetrical component of the improved equilibrium term, named D3Q19-IE, which was originally presented in Eq. (17), may be rewritten in compact form as[77,78]

$$E_q^\star=\frac{t_q}{2\rho_0}\begin{cases}-\frac{2}{3}j_\alpha j_\alpha & \vec{c}_q=(0,0,0)\\ 4(c_{q\alpha}j_\alpha)^2-2j_\alpha j_\alpha & \vec{c}_q\in\{(\pm1,0,0),(0,\pm1,0),(0,0,\pm1)\}\\ 3(c_{q\alpha}j_\alpha)^2-c_{q\alpha}^2 j_\alpha^2 & \text{else.}\end{cases} \tag{B2}$$

In the above equations, summation applies over repeated α indices, where $\alpha=\{x,y,z\}$. Comparing Eqs. (B1) and (B2), virtually the same number of operations is required. Hence, although the D3Q19-IE model formulated on the Hermite basis formalism, given by Eq. (17), may seem to increase the model complexity, its careful implementation[77,78] through Eq. (B2) does not introduce any additional computational cost compared to the classical D3Q19-SE model.

APPENDIX C: DERIVATION OF BULK EQUATIONS OF POISEUILLE–EKMAN CHANNEL FLOW GIVEN IN SEC. III B1

Starting with the exact steady-state recurrence equations of the TRT scheme,[41,42,44] given by the anti-symmetric component of Eq. (5a), and then taking the first-order velocity moment along the x' and y' directions in the (x',y',z') frame, Eq. (14), we obtain

$$\sum_{q=1}^{Q_m/2}\hat{n}_q^-c_{qx'}=\sum_{q=1}^{Q_m/2}\overline{\Delta}_q e_q^+c_{qx'}-\Lambda^+\sum_{q=1}^{Q_m/2}\overline{\Delta}_q^2 e_q^-c_{qx'}$$
$$+\left(\Lambda-\frac{1}{4}\right)\sum_{q=1}^{Q_m/2}\overline{\Delta}_q^2\hat{n}_q^-c_{qx'}, \tag{C1a}$$

$$\sum_{q=1}^{Q_m/2}\hat{n}_q^-c_{qy'}=\sum_{q=1}^{Q_m/2}\overline{\Delta}_q e_q^+c_{qy'}-\Lambda^+\sum_{q=1}^{Q_m/2}\overline{\Delta}_q^2 e_q^-c_{qy'}$$
$$+\left(\Lambda-\frac{1}{4}\right)\sum_{q=1}^{Q_m/2}\overline{\Delta}_q^2\hat{n}_q^-c_{qy'}. \tag{C1b}$$

For the purpose of analysis, let us neglect the $\overline{\Delta}_q e^+$ terms in these equations. This option boils down to neglecting the pressure gradient and the momentum inertia terms. Such a simplification is justifiable here because (i) these terms are absent from the Poiseuille–Ekman rotating channel flow, described in Sec. III, and (ii) even if they were present, as in general flows, they would not interfere with the force implementation, which is the goal of the present analysis.

Let us consider a rotated channel setup. Here, only the diagonal links $c_{qx'}c_{qz'}\neq0$ and $c_{qy'}c_{qz'}\neq0$ (in the rotated setup) will provide a non-trivial solution, whereas the solution pertaining to the non-diagonal links (in the rotated setup) is at equilibrium. The application of the momentum conservation law, given by Eq. (11), over the diagonal links permits determining the exact solution of $\hat{n}_q^-$ for this channel problem,[44] which is given by

$$\hat{n}_q^-=3\,t_q\,c_{qz'}^2(c_{qx'}F_{x'}+c_{qy'}F_{y'}). \tag{C2}$$

Then, the introduction of Eq. (C2) for $\hat{n}_q^-$, Eq. (7) for e_q^-, and Eq. (19) for $F_q^{(\star)}$ [the improved force (IF) scheme] into the TRT recurrence equations, Eq. (C1), and considering the relation between linkwise and finite-difference operators, $\overline{\Delta}_q^2\psi=c_{qz'}^2\,\overline{\Delta}_{z'}^2\psi$, we obtain

$$3F_{x'}\sum_{q=1}^{Q_m/2}t_q c_{qx'}^2c_{qz'}^2+3F_{y'}\sum_{q=1}^{Q_m/2}t_q c_{qx'}c_{qy'}c_{qz'}^2$$
$$=-\Lambda^+\overline{\Delta}_{z'}^2 j_{x'}\sum_{q=1}^{Q_m/2}t_q c_{qx'}^2c_{qz'}^2-\Lambda^+\overline{\Delta}_{z'}^2 j_{y'}\sum_{q=1}^{Q_m/2}t_q c_{qx'}c_{qy'}c_{qz'}^2$$
$$-\Lambda\,\overline{\Delta}_{z'}^2F_{x'}\sum_{q=1}^{Q_m/2}t_q c_{qx'}^2c_{qz'}^2\left(1+3\,k_{x'}\left(c_{qz'}^2-\frac{1}{3}\right)\right)$$

$$-\Lambda\overline{\Delta}_{z'}^2F_{y'}\sum_{q=1}^{Q_m/2}t_qc_{qx'}c_{qy'}c_{qz'}^2\left(1+3\,k_{y'}\left(c_{qz'}^2-\frac{1}{3}\right)\right)+3\left(\Lambda-\frac{1}{4}\right)\overline{\Delta}_{z'}^2F_{x'}\sum_{q=1}^{Q_m/2}t_qc_{qx'}^2c_{qz'}^4+3\left(\Lambda-\frac{1}{4}\right)\overline{\Delta}_{z'}^2F_{y'}\sum_{q=1}^{Q_m/2}t_qc_{qx'}c_{qy'}c_{qz'}^4, \tag{C3a}$$

$$\begin{aligned}3F_{x'}\sum_{q=1}^{Q_m/2}t_qc_{qx'}c_{qy'}c_{qz'}^2+3F_{y'}\sum_{q=1}^{Q_m/2}t_qc_{qy'}^2c_{qz'}^2=&-\Lambda^+\overline{\Delta}_{z'}^2j_{x'}\sum_{q=1}^{Q_m/2}t_qc_{qx'}c_{qy'}c_{qz'}^2-\Lambda^+\overline{\Delta}_{z'}^2j_{y'}\sum_{q=1}^{Q_m/2}t_qc_{qy'}^2c_{qz'}^2\\&-\Lambda\overline{\Delta}_{z'}^2F_{x'}\sum_{q=1}^{Q_m/2}t_qc_{qx'}c_{qy'}c_{qz'}^2\left(1+3\,k_{x'}\left(c_{qz'}^2-\frac{1}{3}\right)\right)-\Lambda\overline{\Delta}_{z'}^2F_{y'}\sum_{q=1}^{Q_m/2}t_qc_{qy'}^2c_{qz'}^2\left(1+3\,k_{y'}\left(c_{qz'}^2-\frac{1}{3}\right)\right)\\&+3\left(\Lambda-\frac{1}{4}\right)\overline{\Delta}_{z'}^2F_{x'}\sum_{q=1}^{Q_m/2}t_qc_{qx'}c_{qy'}c_{qz'}^4+3\left(\Lambda-\frac{1}{4}\right)\overline{\Delta}_{z'}^2F_{y'}\sum_{q=1}^{Q_m/2}t_qc_{qy'}^2c_{qz'}^4.\end{aligned} \tag{C3b}$$

Finally, we compute the second- and fourth-order velocity moments, given by Eq. (10), and the sixth-order velocity moment, given by Eq. (26). As a result, Eqs. (C3a) and (C3b), respectively, reduce to

$$F_{x'}=-\frac{\Lambda^+}{3}\overline{\Delta}_{z'}^2j_{x'}+\left[\frac{4\Lambda(3\,\gamma_{x'}(\theta)-1)(1-k_{x'})-3\,\gamma_{x'}(\theta)}{12}\right]\overline{\Delta}_{z'}^2F_{x'}, \tag{C4a}$$

$$F_{y'}=-\frac{\Lambda^+}{3}\overline{\Delta}_{z'}^2j_{y'}+\left[\frac{4\Lambda(3\,\gamma_{y'}(\alpha)-1)(1-k_{y'})-3\,\gamma_{y'}(\alpha)}{12}\right]\overline{\Delta}_{z'}^2F_{y'}. \tag{C4b}$$

It must be noted that the above results are only exact if the flow solutions are aligned with the lattice. Otherwise, these results are only approximate. Both cases will be covered next.

1. Horizontal channel—exact solutions

By setting the angles $\theta=0$ and $\alpha=0$, Eqs. (C4a) and (C4b), respectively, reduce to

$$F_x=-\frac{\Lambda^+}{3}\overline{\Delta}_z^2j_x-\left[\frac{\Lambda}{3}(1+2k_x)-\left(\Lambda-\frac{1}{4}\right)\right]\overline{\Delta}_z^2F_x, \tag{C5a}$$

$$F_y=-\frac{\Lambda^+}{3}\overline{\Delta}_z^2j_y-\left[\frac{\Lambda}{3}(1+2k_y)-\left(\Lambda-\frac{1}{4}\right)\right]\overline{\Delta}_z^2F_y. \tag{C5b}$$

The substitution of k_x and k_y by Eq. (22) into Eqs. (C5a) and (C5b) vanishes the spurious Laplacian force errors. Otherwise, by using the standard force (SF) scheme, where $k_x=k_y=0$, the Eqs. (C4a) and (C4b) yield

$$F_x=-\frac{\Lambda^+}{3}\overline{\Delta}_z^2j_x+\left(\frac{8\Lambda-3}{12}\right)\overline{\Delta}_z^2F_x, \tag{C6a}$$

$$F_y=-\frac{\Lambda^+}{3}\overline{\Delta}_z^2j_y+\left(\frac{8\Lambda-3}{12}\right)\overline{\Delta}_z^2F_y. \tag{C6b}$$

The reproduction of the Poiseuille–Ekman channel flow equations requires substituting the F_x and F_y terms in Eqs. (C6a) and (C6b) by Eq. (15). The result leads to the following equations:

$$\rho_0a_x+2\,\Omega_z\,j_y=-\frac{\Lambda^+}{3}\overline{\Delta}_z^2j_x+\left(\frac{8\Lambda-3}{12}\right)2\,\Omega_z\overline{\Delta}_z^2j_y, \tag{C7a}$$

$$-2\,\Omega_z\,j_x=-\frac{\Lambda^+}{3}\overline{\Delta}_z^2j_y-\left(\frac{8\Lambda-3}{12}\right)2\,\Omega_z\overline{\Delta}_z^2j_x. \tag{C7b}$$

Finally, by introducing the definitions of the fluid viscosity ν and the viscosity correction $\overline{\delta\nu}$, given by Eqs. (4) and (43), respectively, we arrive at Eqs. (41). In accordance with other problems solved with the TRT scheme,[44,54–57] also in this case the source term correction vanishes for the choice $\Lambda=\frac{3}{8}$.

2. Inclined channel—approximate solutions

Equations (C4) are exact when $\theta=n\,\pi/4$, with $n=0,1,2,\ldots$, and $\alpha=k\,\pi/4$, with $k\in\mathbb{N}_0$; otherwise, the obtained results are only approximate. That is, when the angles θ and/or α take arbitrary values, then the linkwise difference operators must be evaluated through the following second-order (isotropic) approximations given by, e.g., $\overline{\Delta}_q^2j_{x'}c_{qx'}\approx\partial_{z'z'}j_{x'}c_{qx'}c_{qz'}^2$, so that Eqs. (C4) become expressed by the following second-order partial differential equations:

$$\rho_0 a_{x'} + 2\,\Omega_{z'} j_{y'} \approx -\nu\,\partial_{z'z'} j_{x'} + \nu\,\overline{\delta\nu}^{(2)}_{x'}\,\partial_{z'z'} j_{y'}, \tag{C8}$$

$$-2\,\Omega_{z'} j_{x'} \approx -\nu\,\partial_{z'z'} j_{y'} - \nu\,\overline{\delta\nu}^{(2)}_{y'}\,\partial_{z'z'} j_{x'}, \tag{C9}$$

with the following second-order approximation for the viscosity correction terms in arbitrary inclined flow:

$$\overline{\delta\nu}^{(2)}_{x'} = \left[\frac{4\Lambda(3\gamma_{x'}(\theta)-1)(1-k_{x'}) - 3\gamma_{x'}(\theta)}{12}\right]\frac{2\,\Omega_{z'}}{\nu}, \tag{C10}$$

$$\overline{\delta\nu}^{(2)}_{y'} = \left[\frac{4\Lambda(3\gamma_{y'}(\alpha)-1)(1-k_{y'}) - 3\gamma_{y'}(\alpha)}{12}\right]\frac{2\,\Omega_{z'}}{\nu}. \tag{C11}$$

APPENDIX D: DERIVATION OF BOUNDARY SCHEME [MODIFIED LINEAR INTERPOLATION (MLI)] GIVEN IN SEC. II F 2

The modified linear interpolation (MLI) scheme[41,45,61,62] makes use of the adjustable coefficients in its update rule, given by Eq. (32), so that its steady-state closure relation obeys the second-order Taylor expansion along the wall cut link q, given by

$$\alpha^{(u)}\left(j_q + \delta_q\overline{\Delta}_q j_q + \frac{\delta_q^2}{2}\overline{\Delta}_q^2 j_q\right)(\vec{x}_{\rm b}) = \alpha^{(u)} j_q(\vec{x}_{\rm w}), \quad \forall\alpha^{(u)} \neq 0, \tag{D1}$$

where $j_q(\vec{x}_{\rm w}) = t_q\,\rho_0\,\vec{c}_q\cdot\vec{u}_{\rm w}$, with $\vec{u}_{\rm w}$ accounting for the wall movement. The pre-factor $\alpha^{(u)}$ parameterizes the interpolation coefficients $\{\kappa_1, \overline{\kappa}_{-1}, \kappa_0\}$ as given by Eq. (D6).

The procedure to satisfy Eq. (D1) develops as follows. We expand the populations $f_q = e_q^+ + e_q^- + n_q^+ + n_q^-$ and $\hat{f}_q = e_q^+ + e_q^- + n_q^+ + n_q^- + \hat{n}_q^+ + \hat{n}_q^-$ (recall $\hat{n}_q^{\pm} = -\frac{1}{\tau^{\pm}} n_q^{\pm}$) and insert them into Eq. (32). Then, we collect the coefficients from identical terms, which can be represented as follows:

$$\left[\mathcal{A}^+ e_q^+ + \mathcal{A}^- e_q^- + \mathcal{B}^+\hat{n}_q^+ + \mathcal{B}^-\hat{n}_q^- + F_q^{p.c.}\right](\vec{x}_{\rm b}) = \alpha^{(u)} j_q(\vec{x}_{\rm w}), \tag{D2}$$

with

$$\begin{gathered}\mathcal{A}^+ = (\kappa_1 + \overline{\kappa}_{-1} + \kappa_0 - 1), \quad \mathcal{A}^- = (\kappa_1 - \overline{\kappa}_{-1} + \kappa_0 + 1),\\ \mathcal{B}^+ = \left[(\kappa_1 + \overline{\kappa}_{-1}) - \left(\Lambda^+ + \frac{1}{2}\right)\mathcal{A}^+\right], \quad \mathcal{B}^- = \left[(\kappa_1 - \overline{\kappa}_{-1}) - \left(\Lambda^- + \frac{1}{2}\right)\mathcal{A}^-\right].\end{gathered} \tag{D3}$$

Subsequently, we make explicit the macroscopic content of the equilibrium $e_q^{\pm}$ and the symmetric non-equilibrium $\hat{n}_q^+$ populations. The $e_q^{\pm}$ terms are given by Eq. (7) where, as before, we neglect the non-linear contribution E_q from e_q^+ term. The $\hat{n}_q^+$ term is determined by combining Eq. (5a) with Eq. (5b) and, toward this end, we need the $\hat{n}_q^-$ solution too, which for this problem is given by Eq. (C2) in the rotated Cartesian frame. Then, the $\hat{n}_q^+$ term is given by

$$\hat{n}_q^+ = \overline{\Delta}_q j_q - \frac{\overline{\delta\nu}^{(2)}_{\alpha}}{2\,\Omega_{z'}}\,\overline{\Delta}_q F_q, \tag{D4}$$

with $\overline{\delta\nu}^{(2)}_{\alpha} = (\overline{\delta\nu}^{(2)}_{x'}, \overline{\delta\nu}^{(2)}_{y'}, 0)$. Altogether, this allows us to re-express Eq. (D2) in terms of macroscopic variables

$$\left[\mathcal{A}^+ P_q + \mathcal{A}^- j_q + \mathcal{A}^-\Lambda^- F_q^{(\star)} + \mathcal{B}^+\left(\overline{\Delta}_q j_q - \frac{\overline{\delta\nu}^{(2)}_{\alpha}}{2\,\Omega_{z'}}\,\overline{\Delta}_q F_q\right) + \mathcal{B}^-\hat{n}_q^- + F_q^{p.c.}\right](\vec{x}_{\rm b}) = \alpha^{(u)} j_q(\vec{x}_{\rm w}). \tag{D5}$$

Finally, we require that Eq. (D5) matches Eq. (D1). To this end, we solve the following system:

$$\begin{cases}\mathcal{A}^+ = (\kappa_1 + \overline{\kappa}_{-1} + \kappa_0 - 1) = 0\\ \mathcal{A}^- = (\kappa_1 - \overline{\kappa}_{-1} + \kappa_0 + 1) = \alpha^{(u)}\\ \mathcal{B}^+ = \left[(\kappa_1 + \overline{\kappa}_{-1}) - \left(\Lambda^+ + \frac{1}{2}\right)\mathcal{A}^+\right] = \alpha^{(u)}\delta_q\end{cases} \Rightarrow \quad \begin{cases}\kappa_1 = -1 + \alpha^{(u)}\left(\delta_q + \frac{1}{2}\right)\\ \kappa_0 = 1 - \alpha^{(u)}\delta_q\\ \overline{\kappa}_{-1} = 1 - \frac{\alpha^{(u)}}{2}.\end{cases} \tag{D6}$$

The solution of Eq. (D6) yields

$$\alpha^{(u)}\left(j_q+\delta_q\overline{\Delta}_q j_q-\delta_q\,\frac{\overline{\delta\nu}_\alpha^{(2)}}{2\,\Omega_{z'}}\,\overline{\Delta}_q F_q+\Lambda^-F_q^{(\star)}\right)\Bigg|_{(\vec{x}_\mathrm{b})}+\mathcal{B}^-\hat{n}_q^-(\vec{x}_\mathrm{b})+F_q^{p.c.}(\vec{x}_\mathrm{b})=\alpha^{(u)}j_q(\vec{x}_\mathrm{w}). \tag{D7}$$

Equation (D7) can be further simplified by developing $\mathcal{B}^-=[(\kappa_1-\overline{\kappa}_{-1})-(\Lambda^-+\frac{1}{2})\mathcal{A}^-]=-\Lambda^-\alpha^{(u)}+(\kappa_1-1)$, so that

$$\alpha^{(u)}\left(j_q+\delta_q\overline{\Delta}_q j_q-\delta_q\,\frac{\overline{\delta\nu}_\alpha^{(2)}}{2\,\Omega_{z'}}\,\overline{\Delta}_q F_q+\Lambda^-(F_q^{(\star)}-\hat{n}_q^-)\right)\Bigg|_{(\vec{x}_\mathrm{b})}+(\kappa_1-1)\hat{n}_q^-(\vec{x}_\mathrm{b})+F_q^{p.c.}(\vec{x}_\mathrm{b})=\alpha^{(u)}j_q(\vec{x}_\mathrm{w}). \tag{D8}$$

It is evident that, to recover the second-order Taylor expansion along each cut link q, as given by Eq. (D1), the content of the post-collision correction $F_q^{p.c.}$ in Eq. (D8) should be given by

$$F_q^{p.c.}=\alpha^{(u)}\Lambda^-(\hat{n}_q^--F_q^{(\star)})+(1-\kappa_1)\hat{n}_q^-+\alpha^{(u)}\,\delta_q\,\frac{\overline{\delta\nu}_\alpha^{(2)}}{2\,\Omega_{z'}}\,\overline{\Delta}_q F_q+\alpha^{(u)}\,\frac{\delta_q^2}{2}\,\overline{\Delta}_q^2 j_q. \tag{D9}$$

Note that, in Eq. (D8), all terms are determined at the boundary node location $\vec{x}_\mathrm{b}$.

In order to compute the last two terms in Eq. (D9), we can make use of the linkwise second-order finite-difference approximations $\overline{\Delta}_q F_q|^{f.d.}$ and $\overline{\Delta}_q^2 j_q|^{f.d.}$. Considering the approximation for $\overline{\Delta}_q F_q|^{f.d.}$ given in Eq. (35), then the term $\alpha^{(u)}\,\delta_q\,\frac{\overline{\delta\nu}_\alpha^{(2)}}{2\Omega_{z'}}\,\overline{\Delta}_q F_q$ can be computed as follows:

$$\begin{aligned}\alpha^{(u)}\,\delta_q\,\frac{\overline{\delta\nu}_\alpha^{(2)}}{2\,\Omega_{z'}}\,\overline{\Delta}_q F_q|^{f.d.}(\vec{x}_\mathrm{b})=\alpha^{(u)}\,\frac{\delta_{z'}}{(\delta_{z'}+\delta_{\overline{z}'})}\,t_q\,c_{qz'}\Bigg[&\frac{\overline{\delta\nu}_{x'}^{(2)}}{2\,\Omega_{z'}}\,c_{qx'}\left(\frac{\delta_{\overline{z}'}}{\delta_{z'}}\left(F_{x'}(\vec{x}_\mathrm{w})-F_{x'}(\vec{x}_\mathrm{b})\right)+\frac{\delta_{z'}}{\delta_{\overline{z}'}}\left(F_{x'}(\vec{x}_\mathrm{b})-F_{x'}(\vec{x}_{\overline{\mathrm{w}}})\right)\right)\\&+\frac{\overline{\delta\nu}_{y'}^{(2)}}{2\,\Omega_{z'}}\,c_{qy'}\left(\frac{\delta_{\overline{z}'}}{\delta_{z'}}\left(F_{y'}(\vec{x}_\mathrm{w})-F_{y'}(\vec{x}_\mathrm{b})\right)+\frac{\delta_{z'}}{\delta_{\overline{z}'}}\left(F_{y'}(\vec{x}_\mathrm{b})-F_{y'}(\vec{x}_{\overline{\mathrm{w}}})\right)\right)\Bigg].\end{aligned} \tag{D10}$$

Moreover, considering the approximation for $\overline{\Delta}_q^2 j_q|^{f.d.}$ given Eq. (34), the term $\alpha^{(u)}\,\frac{\delta_q^2}{2}\,\overline{\Delta}_q^2 j_q$ can be computed as follows:

$$\alpha^{(u)}\,\frac{\delta_q^2}{2}\,\overline{\Delta}_q^2 j_q|^{f.d.}(\vec{x}_\mathrm{b})=\alpha^{(u)}\,\frac{\delta_{z'}^2}{(\delta_{z'}+\delta_{\overline{z}'})}\,t_q\left[c_{qx'}\left(\frac{j_{x'}(\vec{x}_\mathrm{w})-j_{x'}(\vec{x}_\mathrm{b})}{\delta_{z'}}-\frac{j_{x'}(\vec{x}_\mathrm{b})-j_{x'}(\vec{x}_{\overline{\mathrm{w}}})}{\delta_{\overline{z}'}}\right)+c_{qy'}\left(\frac{j_{y'}(\vec{x}_\mathrm{w})-j_{y'}(\vec{x}_\mathrm{b})}{\delta_{z'}}-\frac{j_{y'}(\vec{x}_\mathrm{b})-j_{y'}(\vec{y}_{\overline{\mathrm{w}}})}{\delta_{\overline{z}'}}\right)\right]. \tag{D11}$$

Overall, this completes the proof that the MLI scheme, determined by the update rule given by Eq. (32), establishes an accurate parabolic approximation for the no-slip velocity boundary condition, given by Eq. (D1), considering a wall moving with velocity $\vec{u}_\mathrm{w}$ and located with an offset from the boundary node given by δ_q, where $\delta_q=\delta_{z'}\,c_{qz'}$ in the adopted coordinate system, see Fig. 3(b).

APPENDIX E: DERIVATION OF BULK EQUATIONS OF ROTATING DUCT FLOW GIVEN IN SEC. IV B

Consider the steady-state Chapman–Enskog fourth-order expansion applied to the TRT equation[41]

$$\hat{n}_q^+=\partial_q e_q^- -\Lambda^-\,\partial_q^2 e_q^+ +\left(\Lambda-\frac{1}{12}\right)\partial_q^3 e_q^- -\Lambda^-\left(\Lambda-\frac{1}{6}\right)\partial_q^4 e_q^+, \tag{E1a}$$

$$\hat{n}_q^-=\partial_q e_q^+ -\Lambda^+\,\partial_q^2 e_q^- +\left(\Lambda-\frac{1}{12}\right)\partial_q^3 e_q^+ -\Lambda^+\left(\Lambda-\frac{1}{6}\right)\partial_q^4 e_q^-, \tag{E1b}$$

with $\partial_q=c_{q\alpha}\,\partial_\alpha$, $\partial_q^2=c_{q\alpha}c_{q\beta}\,\partial_{\alpha\beta}$, etc.

The approximation of the mass and momentum balance equations is produced by the zeroth-order velocity moment over Eq. (E1a) and the first-order velocity moment over Eq. (E1b), respectively

$$\sum_{q=0}^{Q-1}\hat{n}_q^+=\partial_\alpha\sum_{q=0}^{Q-1}c_{q\alpha}\,e_q^- -\Lambda^-\,\partial_{\alpha\beta}\sum_{q=0}^{Q-1}c_{q\alpha}c_{q\beta}\,e_q^+ +\left(\Lambda-\frac{1}{12}\right)\partial_{\alpha\beta\gamma}\sum_{q=0}^{Q-1}c_{q\alpha}c_{q\beta}c_{q\gamma}\,e_q^- -\Lambda^-\left(\Lambda-\frac{1}{6}\right)\partial_{\alpha\beta\gamma\xi}\sum_{q=0}^{Q-1}c_{q\alpha}c_{q\beta}c_{q\gamma}c_{q\xi}\,e_q^+, \tag{E2a}$$

$$\begin{aligned}\sum_{q=0}^{Q-1}c_{q\alpha}\,\hat{n}_q^-=\partial_\beta\sum_{q=1}^{Q-1}c_{q\alpha}c_{q\beta}\,e_q^+ -\Lambda^+\,\partial_{\beta\gamma}\sum_{q=0}^{Q-1}c_{q\alpha}c_{q\beta}c_{q\gamma}\,e_q^- +\left(\Lambda-\frac{1}{12}\right)\partial_{\beta\gamma\xi}\sum_{q=1}^{Q-1}c_{q\alpha}c_{q\beta}c_{q\gamma}c_{q\xi}\,e_q^+\\-\Lambda^+\left(\Lambda-\frac{1}{6}\right)\partial_{\alpha\beta\gamma\xi\eta}\sum_{q=1}^{Q-1}c_{q\alpha}c_{q\beta}c_{q\gamma}c_{q\xi}c_{q\eta}\,e_q^-.\end{aligned} \tag{E2b}$$

For convenience, let us introduce the compact notation

$$\Pi_{\alpha}^{(\mathrm{eq})^-} = \sum_{q=1}^{Q-1} c_{q\alpha}\, e_q^-, \quad \Pi_{\alpha\beta}^{(\mathrm{eq})^+} = \sum_{q=1}^{Q-1} c_{q\alpha} c_{q\beta}\, e_q^+, \quad \Pi_{\alpha\beta\gamma}^{(\mathrm{eq})^-} = \sum_{q=1}^{Q-1} c_{q\alpha} c_{q\beta} c_{q\gamma}\, e_q^-,$$
$$\Pi_{\alpha\beta\gamma\xi}^{(\mathrm{eq})^+} = \sum_{q=1}^{Q-1} c_{q\alpha} c_{q\beta} c_{q\gamma} c_{q\xi}\, e_q^+, \quad \Pi_{\alpha\beta\gamma\xi\eta}^{(\mathrm{eq})^-} = \sum_{q=1}^{Q-1} c_{q\alpha} c_{q\beta} c_{q\gamma} c_{q\xi} c_{q\eta}\, e_q^-. \tag{E3}$$

Equation (E1a) subject to the mass conservation law $\sum_{q=0}^{Q-1} \hat{n}_q^+ = 0$ yields

$$0 = \partial_\alpha \Pi_{\alpha}^{(\mathrm{eq})^-} - \Lambda^- \partial_{\alpha\beta} \Pi_{\alpha\beta}^{(\mathrm{eq})^+} + \left(\Lambda - \frac{1}{12}\right) \partial_{\alpha\beta\gamma} \Pi_{\alpha\beta\gamma}^{(\mathrm{eq})^-} - \Lambda^- \left(\Lambda - \frac{1}{6}\right) \partial_{\alpha\beta\gamma\xi} \Pi_{\alpha\beta\gamma\xi}^{(\mathrm{eq})^+}. \tag{E4}$$

Equation (E1b) subject to the momentum conservation law $\sum_{q=1}^{Q-1} c_{q\alpha}\, \hat{n}_q^- = F_\alpha$ yields

$$F_\alpha = \partial_\beta \Pi_{\alpha\beta}^{(\mathrm{eq})^+} - \Lambda^+ \partial_{\beta\gamma} \Pi_{\alpha\beta\gamma}^{(\mathrm{eq})^-} + \left(\Lambda - \frac{1}{12}\right) \partial_{\beta\gamma\xi} \Pi_{\alpha\beta\gamma\xi}^{(\mathrm{eq})^+} - \Lambda^+ \left(\Lambda - \frac{1}{6}\right) \partial_{\beta\gamma\xi\eta} \Pi_{\alpha\beta\gamma\xi\eta}^{(\mathrm{eq})^-}. \tag{E5}$$

Developing Eq. (E4) over the $\{x, y, z\}$ Cartesian system yields

$$\begin{aligned}
0 = {} & \partial_x \Pi_x^{(\mathrm{eq})^-} + \partial_y \Pi_y^{(\mathrm{eq})^-} + \partial_z \Pi_z^{(\mathrm{eq})^-} - \Lambda^- \left[\partial_{xx} \Pi_{xx}^{(\mathrm{eq})^+} + \partial_{yy} \Pi_{yy}^{(\mathrm{eq})^+} + \partial_{zz} \Pi_{zz}^{(\mathrm{eq})^+} + 2\,\partial_{xy} \Pi_{xy}^{(\mathrm{eq})^+} + 2\,\partial_{xz} \Pi_{xz}^{(\mathrm{eq})^+} + 2\,\partial_{yz} \Pi_{yz}^{(\mathrm{eq})^+}\right] \\
& + \left(\Lambda - \frac{1}{12}\right) \left[\partial_{xxx} \Pi_{xxx}^{(\mathrm{eq})^-} + \partial_{yyy} \Pi_{yyy}^{(\mathrm{eq})^-} + \partial_{zzz} \Pi_{zzz}^{(\mathrm{eq})^-} + 3\,\partial_{xxy} \Pi_{xxy}^{(\mathrm{eq})^-} + 3\,\partial_{xxz} \Pi_{xxz}^{(\mathrm{eq})^-} + 3\,\partial_{xyy} \Pi_{xyy}^{(\mathrm{eq})^-} + 3\,\partial_{xzz} \Pi_{xzz}^{(\mathrm{eq})^-} + 3\,\partial_{yyz} \Pi_{yyz}^{(\mathrm{eq})^-}\right. \\
& \left. + 3\,\partial_{yzz} \Pi_{yzz}^{(\mathrm{eq})^-} + 6\,\partial_{xyz} \Pi_{xyz}^{(\mathrm{eq})^-}\right] - \Lambda^- \left(\Lambda - \frac{1}{6}\right) \left[\partial_{xxxx} \Pi_{xxxx}^{(\mathrm{eq})^+} + \partial_{yyyy} \Pi_{yyyy}^{(\mathrm{eq})^+} + \partial_{zzzz} \Pi_{zzzz}^{(\mathrm{eq})^+} + 6\,\partial_{xxyy} \Pi_{xxyy}^{(\mathrm{eq})^+} + 6\,\partial_x \partial_x \partial_z \partial_z \Pi_{xxzz}^{(\mathrm{eq})^+}\right. \\
& + 6\,\partial_{yyzz} \Pi_{yyzz}^{(\mathrm{eq})^+} + 12\,\partial_{xxyz} \Pi_{xxyz}^{(\mathrm{eq})^+} + 12\,\partial_{xyyz} \Pi_{xyyz}^{(\mathrm{eq})^+} + 12\,\partial_{xyzz} \Pi_{xyzz}^{(\mathrm{eq})^+} + 4\,\partial_{xxxy} \Pi_{xxxy}^{(\mathrm{eq})^+} + 4\,\partial_{xxxz} \Pi_{xxxz}^{(\mathrm{eq})^+} + 4\,\partial_{xyyy} \Pi_{xyyy}^{(\mathrm{eq})^+} \\
& \left. + 4\,\partial_{xzzz} \Pi_{xzzz}^{(\mathrm{eq})^+} + 4\,\partial_{yyyz} \Pi_{yyyyz}^{(\mathrm{eq})^+} + 4\,\partial_{yzzz} \Pi_{yzzz}^{(\mathrm{eq})^+}\right],
\end{aligned} \tag{E6}$$

and developing Eq. (E5) over each component of the $\{x, y, z\}$ Cartesian system yields:

$$\begin{aligned}
F_x = {} & \partial_x \Pi_{xx}^{(\mathrm{eq})^+} + \partial_y \Pi_{xy}^{(\mathrm{eq})^+} + \partial_z \Pi_{xz}^{(\mathrm{eq})^+} - \Lambda^+ \left[\partial_{xx} \Pi_{xxx}^{(\mathrm{eq})^-} + 2\,\partial_{xy} \Pi_{xxy}^{(\mathrm{eq})^-} + 2\,\partial_{xz} \Pi_{xxz}^{(\mathrm{eq})^-} + \partial_{yy} \Pi_{xyy}^{(\mathrm{eq})^-} + 2\,\partial_{yz} \Pi_{xyz}^{(\mathrm{eq})^-} + \partial_{zz} \Pi_{xzz}^{(\mathrm{eq})^-}\right] \\
& + \left(\Lambda - \frac{1}{12}\right) \left[\partial_{xxx} \Pi_{xxxx}^{(\mathrm{eq})^+} + 3\,\partial_{xxy} \Pi_{xxxy}^{(\mathrm{eq})^+} + 3\,\partial_{xxz} \Pi_{xxxz}^{(\mathrm{eq})^+} + 3\,\partial_{xyy} \Pi_{xxyy}^{(\mathrm{eq})^+} + 6\,\partial_{xyz} \Pi_{xxyz}^{(\mathrm{eq})^+}\right. \\
& \left. + 3\,\partial_{xzz} \Pi_{xxzz}^{(\mathrm{eq})^+} + \partial_{yyy} \Pi_{xyyy}^{(\mathrm{eq})^+} + 3\,\partial_{yyz} \Pi_{xyyz}^{(\mathrm{eq})^+} + 3\,\partial_{yzz} \Pi_{xyzz}^{(\mathrm{eq})^+} + \partial_{zzz} \Pi_{xzzz}^{(\mathrm{eq})^+}\right] - \Lambda^+ \left(\Lambda - \frac{1}{6}\right) \left[\partial_{xxxx} \Pi_{xxxxx}^{(\mathrm{eq})^-} + \partial_{yyyy} \Pi_{xyyyy}^{(\mathrm{eq})^-} + \partial_{zzzz} \Pi_{xzzzz}^{(\mathrm{eq})^-}\right. \\
& + 6\,\partial_{xxyy} \Pi_{xxxyy}^{(\mathrm{eq})^-} + 6\,\partial_{xxzz} \Pi_{xxxzz}^{(\mathrm{eq})^-} + 6\,\partial_{yyzz} \Pi_{xyyzz}^{(\mathrm{eq})^-} + 12\,\partial_{xxyz} \Pi_{xxxyz}^{(\mathrm{eq})^-} + 12\,\partial_{xyyz} \Pi_{xxyyz}^{(\mathrm{eq})^-} + 12\,\partial_{xyzz} \Pi_{xxyzz}^{(\mathrm{eq})^-} \\
& \left. + 4\,\partial_{xxxy} \Pi_{xxxxy}^{(\mathrm{eq})^-} + 4\,\partial_{xxxz} \Pi_{xxxxz}^{(\mathrm{eq})^-} + 4\,\partial_{xyyy} \Pi_{xxyyy}^{(\mathrm{eq})^-} + 4\,\partial_{xzzz} \Pi_{xxzzz}^{(\mathrm{eq})^-} + 4\,\partial_{yyyz} \Pi_{xyyyz}^{(\mathrm{eq})^-} + 4\,\partial_{yzzz} \Pi_{xyzzz}^{(\mathrm{eq})^-}\right],
\end{aligned} \tag{E7}$$

$$\begin{aligned}
F_y = {} & \partial_x \Pi_{xy}^{(\mathrm{eq})^+} + \partial_y \Pi_{yy}^{(\mathrm{eq})^+} + \partial_z \Pi_{yz}^{(\mathrm{eq})^+} - \Lambda^+ \left[\partial_{xx} \Pi_{xxy}^{(\mathrm{eq})^-} + 2\,\partial_{xy} \Pi_{xyy}^{(\mathrm{eq})^-} + 2\,\partial_{xz} \Pi_{xyz}^{(\mathrm{eq})^-} + \partial_{yy} \Pi_{yyy}^{(\mathrm{eq})^-} + 2\,\partial_{yz} \Pi_{yyz}^{(\mathrm{eq})^-} + \partial_{zz} \Pi_{yzz}^{(\mathrm{eq})^-}\right] \\
& + \left(\Lambda - \frac{1}{12}\right) \left[\partial_{xxx} \Pi_{xxxy}^{(\mathrm{eq})^+} + 3\,\partial_{xxy} \Pi_{xxyy}^{(\mathrm{eq})^+} + 3\,\partial_{xxz} \Pi_{xxyz}^{(\mathrm{eq})^+} + 3\,\partial_{xyy} \Pi_{xyyy}^{(\mathrm{eq})^+} + 6\,\partial_{xyz} \Pi_{xyyz}^{(\mathrm{eq})^+}\right. \\
& \left. + 3\,\partial_{xzz} \Pi_{xyzz}^{(\mathrm{eq})^+} + \partial_{yyy} \Pi_{yyyy}^{(\mathrm{eq})^+} + 3\,\partial_{yyz} \Pi_{yyyz}^{(\mathrm{eq})^+} + 3\,\partial_{yzz} \Pi_{yyzz}^{(\mathrm{eq})^+} + \partial_{zzz} \Pi_{yzzz}^{(\mathrm{eq})^+}\right] - \Lambda^+ \left(\Lambda - \frac{1}{6}\right) \left[\partial_{xxxx} \Pi_{xxxxy}^{(\mathrm{eq})^-} + \partial_{yyyy} \Pi_{yyyyy}^{(\mathrm{eq})^-} + \partial_{zzzz} \Pi_{yzzzz}^{(\mathrm{eq})^-}\right. \\
& + 6\,\partial_{xxyy} \Pi_{xxyyy}^{(\mathrm{eq})^-} + 6\,\partial_{xxzz} \Pi_{xxyzz}^{(\mathrm{eq})^-} + 6\,\partial_{yyzz} \Pi_{yyyzz}^{(\mathrm{eq})^-} + 12\,\partial_{xxyz} \Pi_{xxyyz}^{(\mathrm{eq})^-} + 12\,\partial_{xyyz} \Pi_{xyyyz}^{(\mathrm{eq})^-} + 12\,\partial_{xyzz} \Pi_{xyyzz}^{(\mathrm{eq})^-} \\
& \left. + 4\,\partial_{xxxy} \Pi_{xxxyy}^{(\mathrm{eq})^-} + 4\,\partial_{xxxz} \Pi_{xxxyz}^{(\mathrm{eq})^-} + 4\,\partial_{xyyy} \Pi_{xyyyy}^{(\mathrm{eq})^-} + 4\,\partial_{xzzz} \Pi_{xyzzz}^{(\mathrm{eq})^-} + 4\,\partial_{yyyz} \Pi_{yyyyz}^{(\mathrm{eq})^-} + 4\,\partial_{yzzz} \Pi_{yyzzz}^{(\mathrm{eq})^-}\right],
\end{aligned} \tag{E8}$$

$$
\begin{aligned}
F_z = {} & \partial_x \Pi_{xz}^{(\mathrm{eq})^+} + \partial_y \Pi_{yz}^{(\mathrm{eq})^+} + \partial_z \Pi_{zz}^{(\mathrm{eq})^+} - \Lambda^+ \left[\partial_{xx} \Pi_{xxz}^{(\mathrm{eq})^-} + 2\,\partial_{xy} \Pi_{xyz}^{(\mathrm{eq})^-} + 2\,\partial_{xz} \Pi_{xzz}^{(\mathrm{eq})^-} + \partial_{yy} \Pi_{yyz}^{(\mathrm{eq})^-} + 2\,\partial_{yz} \Pi_{yzz}^{(\mathrm{eq})^-} + \partial_{zz} \Pi_{zzz}^{(\mathrm{eq})^-} \right] \\
& + \left(\Lambda - \frac{1}{12} \right) \left[\partial_{xxx} \Pi_{xxxz}^{(\mathrm{eq})^+} + 3\,\partial_{xxy} \Pi_{xxyz}^{(\mathrm{eq})^+} + 3\,\partial_{xxz} \Pi_{xxzz}^{(\mathrm{eq})^+} + 3\,\partial_{xyy} \Pi_{xyyz}^{(\mathrm{eq})^+} + 6\,\partial_{xyz} \Pi_{xyzz}^{(\mathrm{eq})^+} \right. \\
& \left. + 3\,\partial_{xzz} \Pi_{xzzz}^{(\mathrm{eq})^+} + \partial_{yyy} \Pi_{yyyz}^{(\mathrm{eq})^+} + 3\,\partial_{yyz} \Pi_{yyzz}^{(\mathrm{eq})^+} + 3\,\partial_{yzz} \Pi_{yzzz}^{(\mathrm{eq})^+} + \partial_{zzz} \Pi_{zzzz}^{(\mathrm{eq})^+} \right] \\
& - \Lambda^+ \left(\Lambda - \frac{1}{6} \right) \left[\partial_{xxx} \partial_x \Pi_{xxxxz}^{(\mathrm{eq})^-} + \partial_{yyyy} \Pi_{yyyyz}^{(\mathrm{eq})^-} + \partial_{zzzz} \Pi_{zzzzz}^{(\mathrm{eq})^-} + 6\,\partial_{xxyy} \Pi_{xxyyz}^{(\mathrm{eq})^-} + 6\,\partial_{xxzz} \Pi_{xxzzz}^{(\mathrm{eq})^-} + 6\,\partial_{yyzz} \Pi_{yyzzz}^{(\mathrm{eq})^-} \right. \\
& + 12\,\partial_{xxyz} \Pi_{xxyzz}^{(\mathrm{eq})^-} + 12\,\partial_{xyyz} \Pi_{xyyzz}^{(\mathrm{eq})^-} + 12\,\partial_{xyzz} \Pi_{xyzzz}^{(\mathrm{eq})^-} + 4\,\partial_{xxxy} \Pi_{xxxyz}^{(\mathrm{eq})^-} + 4\,\partial_{xxxz} \Pi_{xxxzz}^{(\mathrm{eq})^-} + 4\,\partial_{xyyy} \Pi_{xyyyz}^{(\mathrm{eq})^-} \\
& \left. + 4\,\partial_{xzzz} \Pi_{xzzzz}^{(\mathrm{eq})^-} + 4\,\partial_{yyyz} \Pi_{yyyzz}^{(\mathrm{eq})^-} + 4\,\partial_y \partial_z \partial_z \partial_z \Pi_{yzzzz}^{(\mathrm{eq})^-} \right]. \qquad \text{(E9)}
\end{aligned}
$$

1. D3Q19 model

Table X lists the TRT D3Q19 velocity moments, defined in Eq. (E3). Differences between D3Q19-SE and D3Q19-IE models lie in the bold terms inside $\Pi_{xxyy}^{(\mathrm{eq})^+}$, $\Pi_{xxzz}^{(\mathrm{eq})^+}$, and $\Pi_{yyzz}^{(\mathrm{eq})^+}$ moments. The source term is considered inside the equilibrium, as defined in Eq. (7b), and F_q is formulated based on the SF model, Eq. (8d).

The substitution of the TRT D3Q19 velocity moments displayed in Table X into Eq. (E6) yields

TABLE X. TRT velocity moments in D3Q19. The Hermite based standard equilibrium (D3Q19-SE) cannot be considered compatible with the D3Q19 lattice discretization as it introduces the spurious terms in $\Pi_{xxyy}^{(\mathrm{eq})^+}$, $\Pi_{xxzz}^{(\mathrm{eq})^+}$, and $\Pi_{yyzz}^{(\mathrm{eq})^+}$, which are marked in bold. The improved D3Q19 equilibrium (D3Q19-IE) recovers the exact same discretization structure, with the exception of the undesirable bold terms, which are eliminated.

$\Pi_{x}^{(\mathrm{eq})^-} = j_x + \Lambda^- F_x$	$\Pi_{y}^{(\mathrm{eq})^-} = j_y + \Lambda^- F_y$	$\Pi_{z}^{(\mathrm{eq})^-} = j_z + \Lambda^- F_z$
$\Pi_{xx}^{(\mathrm{eq})^+} = P + \frac{j_x^2}{\rho_0}$	$\Pi_{yy}^{(\mathrm{eq})^+} = P + \frac{j_y^2}{\rho_0}$	$\Pi_{zz}^{(\mathrm{eq})^+} = P + \frac{j_z^2}{\rho_0}$
$\Pi_{xy}^{(\mathrm{eq})^+} = \frac{j_x j_y}{\rho_0}$	$\Pi_{xz}^{(\mathrm{eq})^+} = \frac{j_x j_z}{\rho_0}$	$\Pi_{yz}^{(\mathrm{eq})^+} = \frac{j_y j_z}{\rho_0}$
$\Pi_{xxx}^{(\mathrm{eq})^-} = j_x + \Lambda^- F_x$	$\Pi_{yyy}^{(\mathrm{eq})^-} = j_y + \Lambda^- F_y$	$\Pi_{zzz}^{(\mathrm{eq})^-} = j_z + \Lambda^- F_z$
$\Pi_{xyy}^{(\mathrm{eq})^-} = \Pi_{xzz}^{(\mathrm{eq})^-} = \frac{j_x}{3} + \Lambda^- \frac{F_x}{3}$	$\Pi_{xxy}^{(\mathrm{eq})^-} = \Pi_{yzz}^{(\mathrm{eq})^-} = \frac{j_y}{3} + \Lambda^- \frac{F_y}{3}$	$\Pi_{xxz}^{(\mathrm{eq})^-} = \Pi_{yyz}^{(\mathrm{eq})^-} = \frac{j_z}{3} + \Lambda^- \frac{F_z}{3}$
	$\Pi_{xyz}^{(\mathrm{eq})^-} = 0$	
$\Pi_{xxxx}^{(\mathrm{eq})^+} = P + \frac{j_x^2}{\rho_0}$	$\Pi_{yyyy}^{(\mathrm{eq})^+} = P + \frac{j_y^2}{\rho_0}$	$\Pi_{zzzz}^{(\mathrm{eq})^+} = P + \frac{j_z^2}{\rho_0}$
$\Pi_{xxxy}^{(\mathrm{eq})^+} = \Pi_{xyyy}^{(\mathrm{eq})^+} = \frac{j_x j_y}{\rho_0}$	$\Pi_{xxxz}^{(\mathrm{eq})^+} = \Pi_{xzzz}^{(\mathrm{eq})^+} = \frac{j_x j_z}{\rho_0}$	$\Pi_{yyyz}^{(\mathrm{eq})^+} = \Pi_{yzzz}^{(\mathrm{eq})^+} = \frac{j_y j_z}{\rho_0}$
$\Pi_{xxyz}^{(\mathrm{eq})^+} = \Pi_{xyyz}^{(\mathrm{eq})^+} = \Pi_{xyzz}^{(\mathrm{eq})^+} = 0$		
$\Pi_{xxyy}^{(\mathrm{eq})^+} = \frac{P}{3} + \frac{j_x^2 + j_y^2}{3\rho_0} - \frac{\mathbf{j_z^2}}{\mathbf{6}\rho_0}$	$\Pi_{xxzz}^{(\mathrm{eq})^+} = \frac{P}{3} + \frac{j_x^2 + j_z^2}{3\rho_0} - \frac{\mathbf{j_y^2}}{\mathbf{6}\rho_0}$	$\Pi_{yyzz}^{(\mathrm{eq})^+} = \frac{P}{3} + \frac{j_y^2 + j_z^2}{3\rho_0} - \frac{\mathbf{j_x^2}}{\mathbf{6}\rho_0}$
$\Pi_{xxxxx}^{(\mathrm{eq})^-} = j_x + \Lambda^- F_x$	$\Pi_{yyyyy}^{(\mathrm{eq})^-} = j_y + \Lambda^- F_y$	$\Pi_{zzzzz}^{(\mathrm{eq})^-} = j_z + \Lambda^- F_z$
	$\Pi_{xyyyy}^{(\mathrm{eq})^-} = \Pi_{xzzzz}^{(\mathrm{eq})^-} = \Pi_{xxxyy}^{(\mathrm{eq})^-} = \Pi_{xxxzz}^{(\mathrm{eq})^-} = \frac{j_x}{3} + \Lambda^- \frac{F_x}{3}$	
	$\Pi_{xxxxy}^{(\mathrm{eq})^-} = \Pi_{xxyyy}^{(\mathrm{eq})^-} = \Pi_{yzzzz}^{(\mathrm{eq})^-} = \Pi_{yyyzz}^{(\mathrm{eq})^-} = \frac{j_y}{3} + \Lambda^- \frac{F_y}{3}$	
	$\Pi_{xxxxz}^{(\mathrm{eq})^-} = \Pi_{xxzzz}^{(\mathrm{eq})^-} = \Pi_{yyyyz}^{(\mathrm{eq})^-} = \Pi_{yyzzz}^{(\mathrm{eq})^-} = \frac{j_z}{3} + \Lambda^- \frac{F_z}{3}$	
	$\Pi_{xyyzz}^{(\mathrm{eq})^-} = \Pi_{xxxyz}^{(\mathrm{eq})^-} = \Pi_{xxyzz}^{(\mathrm{eq})^-} = \Pi_{xyyyz}^{(\mathrm{eq})^-} = \Pi_{xxyyz}^{(\mathrm{eq})^-} = \Pi_{xyzzz}^{(\mathrm{eq})^-} = 0$	

$$
\begin{aligned}
0 = &\left[\partial_x j_x + \partial_y j_y + \partial_z j_z\right] + \Lambda^-\left[\partial_x F_x + \partial_y F_y + \partial_z F_z\right] \\
&- \Lambda^-\left[\partial_{xx}\left(P + \frac{j_x^2}{\rho_0}\right) + \partial_{yy}\left(P + \frac{j_y^2}{\rho_0}\right) + \partial_{zz}\left(P + \frac{j_z^2}{\rho_0}\right) + 2\,\partial_{xy}\left(\frac{j_x j_y}{\rho_0}\right) + 2\,\partial_{xz}\left(\frac{j_x j_z}{\rho_0}\right) + 2\,\partial_{yz}\left(\frac{j_y j_z}{\rho_0}\right)\right] \\
&+ \left(\Lambda - \frac{1}{12}\right)\left[\partial_{xxx} j_x + \partial_{yyy} j_y + \partial_{zzz} j_z + \partial_{xyy} j_x + \partial_{xzz} j_x + \partial_{xxy} j_y + \partial_{yzz} j_y + \partial_{xxz} j_z + \partial_{yzz} j_z\right] \\
&+ \Lambda^-\left(\Lambda - \frac{1}{12}\right)\left[\partial_{xxx} F_x + \partial_{yyy} F_y + \partial_{zzz} F_z + \partial_{xyy} F_x + \partial_{xzz} F_x + \partial_{xxy} F_y + \partial_{yzz} F_y + \partial_{xxz} F_z + \partial_{yzz} F_z\right] \\
&- \Lambda^-\left(\Lambda - \frac{1}{6}\right)\left[\partial_{xxxx}\left(P + \frac{j_x^2}{\rho_0}\right) + \partial_{yyyy}\left(P + \frac{j_y^2}{\rho_0}\right) + \partial_{zzzz}\left(P + \frac{j_z^2}{\rho_0}\right)\right. \\
&+ 2\,\partial_{xxyy}\left(P + \frac{j_x^2 + j_y^2}{\rho_0} - \frac{\mathbf{j_z^2}}{\mathbf{2\rho_0}}\right) + 2\,\partial_{xxzz}\left(P + \frac{j_x^2 + j_z^2}{\rho_0} - \frac{\mathbf{j_y^2}}{\mathbf{2\rho_0}}\right) + 2\,\partial_{yyzz}\left(P + \frac{j_y^2 + j_z^2}{\rho_0} - \frac{\mathbf{j_x^2}}{\mathbf{2\rho_0}}\right) \\
&\left.+ 4\,\partial_{xxxy}\left(\frac{j_x j_y}{\rho_0}\right) + 4\,\partial_{xxxz}\left(\frac{j_x j_z}{\rho_0}\right) + 4\,\partial_{xyyy}\left(\frac{j_x j_y}{\rho_0}\right) + 4\,\partial_{xzzz}\left(\frac{j_x j_z}{\rho_0}\right) + 4\,\partial_{yyyz}\left(\frac{j_y j_z}{\rho_0}\right) + 4\,\partial_{yzzz}\left(\frac{j_y j_z}{\rho_0}\right)\right]. \qquad \text{(E10)}
\end{aligned}
$$

The substitution of the TRT D3Q19 velocity moments of Table X into Eqs. (E7)–(E9) yields

$$
\begin{aligned}
F_x = &\,\partial_x\left(P + \frac{j_x^2}{\rho_0}\right) + \partial_y\left(\frac{j_x j_y}{\rho_0}\right) + \partial_z\left(\frac{j_x j_z}{\rho_0}\right) - \frac{\Lambda^+}{3}\left[\partial_{xx} j_x + \partial_{yy} j_x + \partial_{zz} j_x + 2\,\partial_x\left(\partial_x j_x + \partial_y j_y + \partial_z j_z\right)\right] \\
&- \frac{\Lambda}{3}\left[\partial_{xx} F_x + \partial_{yy} F_x + \partial_{zz} F_x + 2\,\partial_x\left(\partial_x F_x + \partial_y F_y + \partial_z F_z\right)\right] + \left(\Lambda - \frac{1}{12}\right)\left[\partial_{xxx}\left(P + \frac{j_x^2}{\rho_0}\right) + \partial_{yyy}\left(\frac{j_x j_y}{\rho_0}\right) + \partial_{zzz}\left(\frac{j_x j_z}{\rho_0}\right)\right. \\
&\left.+ 3\,\partial_{xxy}\left(\frac{j_x j_y}{\rho_0}\right) + 3\,\partial_{xxz}\left(\frac{j_x j_z}{\rho_0}\right) + \partial_{xyy}\left(P + \frac{j_x^2 + j_y^2}{\rho_0} - \frac{\mathbf{j_z^2}}{\mathbf{2\rho_0}}\right) + \partial_{xzz}\left(P + \frac{j_x^2 + j_z^2}{\rho_0} - \frac{\mathbf{j_y^2}}{\mathbf{2\rho_0}}\right)\right] \\
&- \frac{\Lambda^+}{3}\left(\Lambda - \frac{1}{6}\right)\left[3\,\partial_{xxxx} j_x + \partial_{yyyy} j_x + \partial_{zzzz} j_x + 6\,\partial_{xxyy} j_x + 6\,\partial_{xxzz} j_x + 4\,\partial_{xxxy} j_y + 4\,\partial_{xyyy} j_y + 4\,\partial_{xxxz} j_z + 4\,\partial_{xzzz} j_z\right] \\
&- \frac{\Lambda}{3}\left(\Lambda - \frac{1}{6}\right)\left[3\,\partial_{xxxx} F_x + \partial_{yyyy} F_x + \partial_{zzzz} F_x + 6\,\partial_{xxyy} F_x + 6\,\partial_{xxzz} F_x + 4\,\partial_{xxxy} F_y + 4\,\partial_{xyyy} F_y + 4\,\partial_{xxxz} F_z + 4\,\partial_{xzzz} F_z\right], \qquad \text{(E11)}
\end{aligned}
$$

$$
\begin{aligned}
F_y = &\,\partial_x\left(\frac{j_x j_y}{\rho_0}\right) + \partial_y\left(P + \frac{j_y^2}{\rho_0}\right) + \partial_z\left(\frac{j_y j_z}{\rho_0}\right) - \frac{\Lambda^+}{3}\left[\partial_{xx} j_y + \partial_{yy} j_y + \partial_{zz} j_y + 2\,\partial_y\left(\partial_x j_x + \partial_y j_y + \partial_z j_z\right)\right] \\
&- \frac{\Lambda}{3}\left[\partial_{xx} F_y + \partial_{yy} F_y + \partial_{zz} F_y + 2\,\partial_y\left(\partial_x F_x + \partial_y F_y + \partial_z F_z\right)\right] + \left(\Lambda - \frac{1}{12}\right)\left[\partial_{xxx}\left(\frac{j_x j_y}{\rho_0}\right) + \partial_{yyy}\left(P + \frac{j_y^2}{\rho_0}\right) + \partial_{zzz}\left(\frac{j_y j_z}{\rho_0}\right)\right. \\
&\left.+ 3\,\partial_{xyy}\left(\frac{j_x j_y}{\rho_0}\right) + 3\,\partial_{yyz}\left(\frac{j_y j_z}{\rho_0}\right) + \partial_{xxy}\left(P + \frac{j_x^2 + j_y^2}{\rho_0} - \frac{\mathbf{j_z^2}}{\mathbf{2\rho_0}}\right) + \partial_{yzz}\left(P + \frac{j_y^2 + j_z^2}{\rho_0} - \frac{\mathbf{j_x^2}}{\mathbf{2\rho_0}}\right)\right] \\
&- \frac{\Lambda^+}{3}\left(\Lambda - \frac{1}{6}\right)\left[\partial_{xxxx} j_y + 3\,\partial_{yyyy} j_y + \partial_{zzzz} j_y + 6\,\partial_{xxyy} j_y + 6\,\partial_{yyzz} j_y + 4\,\partial_{xxxy} j_x + 4\,\partial_{xyyy} j_x + 4\,\partial_{yyyz} j_z + 4\,\partial_{yzzz} j_z\right] \\
&- \frac{\Lambda}{3}\left(\Lambda - \frac{1}{6}\right)\left[\partial_{xxxx} F_y + 3\,\partial_{yyyy} F_y + \partial_{zzzz} F_y + 6\,\partial_{xxyy} F_y + 6\,\partial_{yyzz} F_y + 4\,\partial_{xxxy} F_x + 4\,\partial_{xyyy} F_x + 4\,\partial_{yyyz} F_z + 4\,\partial_{yzzz} F_z\right], \qquad \text{(E12)}
\end{aligned}
$$

$$
\begin{aligned}
F_z = {} & \partial_x\left(\frac{j_x j_z}{\rho_0}\right) + \partial_y\left(\frac{j_y j_z}{\rho_0}\right) + \partial_z\left(P + \frac{j_z^2}{\rho_0}\right) - \frac{\Lambda^+}{3}\left[\partial_{xx} j_z + \partial_{yy} j_z + \partial_{zz} j_z + 2\,\partial_z\left(\partial_x j_x + \partial_y j_y + \partial_z j_z\right)\right] \\
& - \frac{\Lambda}{3}\left[\partial_{xx} F_z + \partial_{yy} F_z + \partial_{zz} F_z + 2\,\partial_z\left(\partial_x F_x + \partial_y F_y + \partial_z F_z\right)\right] + \left(\Lambda - \frac{1}{12}\right)\left[\partial_{xxx}\left(\frac{j_x j_z}{\rho_0}\right) + \partial_{yyy}\left(\frac{j_y j_z}{\rho_0}\right) + \partial_{zzz}\left(P + \frac{j_z^2}{\rho_0}\right)\right. \\
& \left. + 3\,\partial_{xzz}\left(\frac{j_x j_z}{\rho_0}\right) + 3\,\partial_{yzz}\left(\frac{j_y j_z}{\rho_0}\right) + \partial_{xxz}\left(P + \frac{j_x^2 + j_z^2}{\rho_0} - \frac{\mathbf{j_y^2}}{\mathbf{2\rho_0}}\right) + \partial_{yyz}\left(P + \frac{j_y^2 + j_z^2}{\rho_0} - \frac{\mathbf{j_x^2}}{\mathbf{2\rho_0}}\right)\right] \\
& - \frac{\Lambda^+}{3}\left(\Lambda - \frac{1}{6}\right)\left[\partial_{xxxx} j_z + \partial_{yyyy} j_z + 3\,\partial_{zzzz} j_z + 6\,\partial_{xxzz} j_z + 6\,\partial_{yyzz} j_z + 4\,\partial_{xxxz} j_x + 4\,\partial_{xzzz} j_x + 4\,\partial_{yyyz} j_y + 4\,\partial_{yzzz} j_y\right] \\
& - \frac{\Lambda}{3}\left(\Lambda - \frac{1}{6}\right)\left[\partial_{xxxx} F_z + \partial_{yyyy} j_z + 3\,\partial_{zzzz} F_z + 6\,\partial_{xxzz} F_z + 6\,\partial_{yyzz} F_z + 4\,\partial_{xxxz} F_x + 4\,\partial_{xzzz} F_x + 4\,\partial_{yyyz} F_y + 4\,\partial_{yzzz} F_y\right]. \qquad \text{(E13)}
\end{aligned}
$$

2. D3Q27 model

Table XI lists the TRT D3Q27 velocity moments, defined in Eq. (E3). Similarly to the previous case, the source term is considered inside the equilibrium, as defined in Eq. (7b), and F_q is formulated based on the SF model, Eq. (8d).

The substitution of the TRT D3Q27 velocity moments of Table XI into Eq. (E6) yields

TABLE XI. TRT velocity moments in D3Q27. The Hermite based standard equilibrium (D3Q27-SE) is considered.

$\Pi_x^{(\mathrm{eq})^-} = j_x + \Lambda^- F_x$	$\Pi_y^{(\mathrm{eq})^-} = j_y + \Lambda^- F_y$	$\Pi_z^{(\mathrm{eq})^-} = j_z + \Lambda^- F_z$
$\Pi_{xx}^{(\mathrm{eq})^+} = P + \frac{j_x^2}{\rho_0}$	$\Pi_{yy}^{(\mathrm{eq})^+} = P + \frac{j_y^2}{\rho_0}$	$\Pi_{zz}^{(\mathrm{eq})^+} = P + \frac{j_z^2}{\rho_0}$
$\Pi_{xy}^{(\mathrm{eq})^+} = \frac{j_x j_y}{\rho_0}$	$\Pi_{xz}^{(\mathrm{eq})^+} = \frac{j_x j_z}{\rho_0}$	$\Pi_{yz}^{(\mathrm{eq})^+} = \frac{j_y j_z}{\rho_0}$
$\Pi_{xxx}^{(\mathrm{eq})^-} = j_x + \Lambda^- F_x$	$\Pi_{yyy}^{(\mathrm{eq})^-} = j_y + \Lambda^- F_y$	$\Pi_{zzz}^{(\mathrm{eq})^-} = j_z + \Lambda^- F_z$
$\Pi_{xyy}^{(\mathrm{eq})^-} = \Pi_{xzz}^{(\mathrm{eq})^-} = \frac{j_x}{3} + \Lambda^- \frac{F_x}{3}$	$\Pi_{xxy}^{(\mathrm{eq})^-} = \Pi_{yzz}^{(\mathrm{eq})^-} = \frac{j_y}{3} + \Lambda^- \frac{F_y}{3}$	$\Pi_{xxz}^{(\mathrm{eq})^-} = \Pi_{yyz}^{(\mathrm{eq})^-} = \frac{j_z}{3} + \Lambda^- \frac{F_z}{3}$
	$\Pi_{xyz}^{(\mathrm{eq})^-} = 0$	
$\Pi_{xxxx}^{(\mathrm{eq})^+} = P + \frac{j_x^2}{\rho_0}$	$\Pi_{yyyy}^{(\mathrm{eq})^+} = P + \frac{j_y^2}{\rho_0}$	$\Pi_{zzzz}^{(\mathrm{eq})^+} = P + \frac{j_z^2}{\rho_0}$
$\Pi_{xxxy}^{(\mathrm{eq})^+} = \Pi_{xyyy}^{(\mathrm{eq})^+} = \frac{j_x j_y}{\rho_0}$	$\Pi_{xxxz}^{(\mathrm{eq})^+} = \Pi_{xzzz}^{(\mathrm{eq})^+} = \frac{j_x j_z}{\rho_0}$	$\Pi_{yyyz}^{(\mathrm{eq})^+} = \Pi_{yzzz}^{(\mathrm{eq})^+} = \frac{j_y j_z}{\rho_0}$
$\Pi_{xxyz}^{(\mathrm{eq})^+} = \frac{j_y j_z}{3\rho_0}$	$\Pi_{xyyz}^{(\mathrm{eq})^+} = \frac{j_x j_z}{3\rho_0}$	$\Pi_{xyzz}^{(\mathrm{eq})^+} = \frac{j_x j_y}{3\rho_0}$
$\Pi_{xxyy}^{(\mathrm{eq})^+} = \frac{P}{3} + \frac{j_x^2 + j_y^2}{3\rho_0}$	$\Pi_{xxzz}^{(\mathrm{eq})^+} = \frac{P}{3} + \frac{j_x^2 + j_z^2}{3\rho_0}$	$\Pi_{yyzz}^{(\mathrm{eq})^+} = \frac{P}{3} + \frac{j_y^2 + j_z^2}{3\rho_0}$
$\Pi_{xxxxx}^{(\mathrm{eq})^-} = j_x + \Lambda^- F_x$	$\Pi_{yyyyy}^{(\mathrm{eq})^-} = j_y + \Lambda^- F_y$	$\Pi_{zzzzz}^{(\mathrm{eq})^-} = j_z + \Lambda^- F_z$
	$\Pi_{xyyyy}^{(\mathrm{eq})^-} = \Pi_{xzzzz}^{(\mathrm{eq})^-} = \Pi_{xxxyy}^{(\mathrm{eq})^-} = \Pi_{xxxzz}^{(\mathrm{eq})^-} = \frac{j_x}{3} + \Lambda^- \frac{F_x}{3}$	
	$\Pi_{xxxxy}^{(\mathrm{eq})^-} = \Pi_{xxyyy}^{(\mathrm{eq})^-} = \Pi_{yzzzz}^{(\mathrm{eq})^-} = \Pi_{yyyzz}^{(\mathrm{eq})^-} = \frac{j_y}{3} + \Lambda^- \frac{F_y}{3}$	
	$\Pi_{xxxxz}^{(\mathrm{eq})^-} = \Pi_{xxzzz}^{(\mathrm{eq})^-} = \Pi_{yyyyz}^{(\mathrm{eq})^-} = \Pi_{yyzzz}^{(\mathrm{eq})^-} = \frac{j_z}{3} + \Lambda^- \frac{F_z}{3}$	
$\Pi_{xyyzz}^{(\mathrm{eq})^-} = \Pi_{xxxyz}^{(\mathrm{eq})^-} = \frac{j_x}{9} + \Lambda^- \frac{F_x}{9}$	$\Pi_{xxyzz}^{(\mathrm{eq})^-} = \Pi_{xyyyz}^{(\mathrm{eq})^-} = \frac{j_y}{9} + \Lambda^- \frac{F_y}{9}$	$\Pi_{xxyyz}^{(\mathrm{eq})^-} = \Pi_{xyzzz}^{(\mathrm{eq})^-} = \frac{j_z}{9} + \Lambda^- \frac{F_z}{9}$

$$
\begin{aligned}
0 = &\left[\partial_x j_x + \partial_y j_y + \partial_z j_z\right] + \Lambda^-\left[\partial_x F_x + \partial_y F_y + \partial_z F_z\right] \\
&- \Lambda^-\left[\partial_{xx}\left(P + \frac{j_x^2}{\rho_0}\right) + \partial_{yy}\left(P + \frac{j_y^2}{\rho_0}\right) + \partial_{zz}\left(P + \frac{j_z^2}{\rho_0}\right) + 2\,\partial_{xy}\left(\frac{j_x j_y}{\rho_0}\right) + 2\,\partial_{xz}\left(\frac{j_x j_z}{\rho_0}\right) + 2\,\partial_{yz}\left(\frac{j_y j_z}{\rho_0}\right)\right] \\
&+ \left(\Lambda - \frac{1}{12}\right)\left[\partial_{xxx} j_x + \partial_{yyy} j_y + \partial_{zzz} j_z + \partial_{xyy} j_x + \partial_{xzz} j_x + \partial_{xxy} j_y + \partial_{yzz} j_y + \partial_{xxz} j_z + \partial_{yzz} j_z\right] \\
&+ \Lambda^-\left(\Lambda - \frac{1}{12}\right)\left[\partial_{xxx} F_x + \partial_{yyy} F_y + \partial_{zzz} F_z + \partial_{xyy} F_x + \partial_{xzz} F_x + \partial_{xxy} F_y + \partial_{yzz} F_y + \partial_{xxz} F_z + \partial_{yzz} F_z\right] \\
&- \Lambda^-\left(\Lambda - \frac{1}{6}\right)\left[\partial_{xxxx}\left(P + \frac{j_x^2}{\rho_0}\right) + \partial_{yyyy}\left(P + \frac{j_y^2}{\rho_0}\right) + \partial_{zzzz}\left(P + \frac{j_z^2}{\rho_0}\right)\right. \\
&+ 2\,\partial_{xxyy}\left(P + \frac{j_x^2 + j_y^2}{\rho_0}\right) + 2\,\partial_{xxzz}\left(P + \frac{j_x^2 + j_z^2}{\rho_0}\right) + 2\,\partial_{yyzz}\left(P + \frac{j_y^2 + j_z^2}{\rho_0}\right) \\
&+ 4\,\partial_{xxyz}\left(\frac{j_y j_z}{\rho_0}\right) + 4\,\partial_{xyyz}\left(\frac{j_x j_z}{\rho_0}\right) + 4\,\partial_{xyzz}\left(\frac{j_x j_y}{\rho_0}\right) + 4\,\partial_{xxxy}\left(\frac{j_x j_y}{\rho_0}\right) + 4\,\partial_{xxxz}\left(\frac{j_x j_z}{\rho_0}\right) + 4\,\partial_{xyyy}\left(\frac{j_x j_y}{\rho_0}\right) \\
&\left.+ 4\,\partial_{xzzz}\left(\frac{j_x j_z}{\rho_0}\right) + 4\,\partial_{yyyz}\left(\frac{j_y j_z}{\rho_0}\right) + 4\,\partial_{yzzz}\left(\frac{j_y j_z}{\rho_0}\right)\right]. \qquad \text{(E14)}
\end{aligned}
$$

The substitution of the TRT D3Q27 velocity moments displayed in Table XI into Eqs. (E7)–(E9) yields

$$
\begin{aligned}
F_x = &\,\partial_x\left(P + \frac{j_x^2}{\rho_0}\right) + \partial_y\left(\frac{j_x j_y}{\rho_0}\right) + \partial_z\left(\frac{j_x j_z}{\rho_0}\right) - \frac{\Lambda^+}{3}\left[\partial_{xx} j_x + \partial_{yy} j_x + \partial_{zz} j_x + 2\,\partial_x\left(\partial_x j_x + \partial_y j_y + \partial_z j_z\right)\right] \\
&- \frac{\Lambda}{3}\left[\partial_{xx} F_x + \partial_{yy} F_x + \partial_{zz} F_x + 2\,\partial_x\left(\partial_x F_x + \partial_y F_y + \partial_z F_z\right)\right] + \left(\Lambda - \frac{1}{12}\right)\left[\partial_{xxx}\left(P + \frac{j_x^2}{\rho_0}\right) + \partial_{yyy}\left(\frac{j_x j_y}{\rho_0}\right) + \partial_{zzz}\left(\frac{j_x j_z}{\rho_0}\right)\right. \\
&+ 3\,\partial_{xxy}\left(\frac{j_x j_y}{\rho_0}\right) + 3\,\partial_{xxz}\left(\frac{j_x j_z}{\rho_0}\right) + 2\,\partial_{xyz}\left(\frac{j_y j_z}{\rho_0}\right) + \partial_{yyz}\left(\frac{j_x j_z}{\rho_0}\right) + \partial_{yzz}\left(\frac{j_x j_y}{\rho_0}\right) + \partial_{xyy}\left(P + \frac{j_x^2 + j_y^2}{\rho_0}\right) + \partial_{xzz}\left(P + \frac{j_x^2 + j_z^2}{\rho_0}\right)\left.\right] \\
&- \frac{\Lambda^+}{3}\left(\Lambda - \frac{1}{6}\right)\left[3\,\partial_{xxxx} j_x + \partial_{yyyy} j_x + \partial_{zzzz} j_x + 6\,\partial_{xxyy} j_x + 6\,\partial_{xxzz} j_x + 2\,\partial_{yyzz} j_x + 4\,\partial_{xxyz} j_x + 4\,\partial_{xyzz} j_y + 4\,\partial_{xxxy} j_y + 4\,\partial_{xyyy} j_y\right. \\
&\left.+ 4\,\partial_{xxxz} j_z + 4\,\partial_{xyyz} j_z + 4\,\partial_{xzzz} j_z + \frac{4}{3}\,\partial_{yyyz} j_y + \frac{4}{3}\,\partial_{yzzz} j_z\right] - \frac{\Lambda}{3}\left(\Lambda - \frac{1}{6}\right)\left[3\,\partial_{xxxx} F_x + \partial_{yyyy} F_x + \partial_{zzzz} F_x\right. \\
&+ 6\,\partial_{xxyy} F_x + 6\,\partial_{xxzz} F_x + 2\,\partial_{yyzz} F_x + 4\,\partial_{xxyz} F_x + 4\,\partial_{xyzz} F_y + 4\,\partial_{xxxy} F_y + 4\,\partial_{xyyy} F_y \\
&\left.+ 4\,\partial_{xxxz} F_z + 4\,\partial_{xyyz} F_z + 4\,\partial_{xzzz} F_z + \frac{4}{3}\,\partial_{yyyz} F_y + \frac{4}{3}\,\partial_{yzzz} F_z\right], \qquad \text{(E15)}
\end{aligned}
$$

$$
\begin{aligned}
F_y = &\,\partial_x\left(\frac{j_x j_y}{\rho_0}\right) + \partial_y\left(P + \frac{j_y^2}{\rho_0}\right) + \partial_z\left(\frac{j_y j_z}{\rho_0}\right) - \frac{\Lambda^+}{3}\left[\partial_{xx} j_y + \partial_{yy} j_y + \partial_{zz} j_y + 2\,\partial_y\left(\partial_x j_x + \partial_y j_y + \partial_z j_z\right)\right] \\
&- \frac{\Lambda}{3}\left[\partial_{xx} F_y + \partial_{yy} F_y + \partial_{zz} F_y + 2\,\partial_y\left(\partial_x F_x + \partial_y F_y + \partial_z F_z\right)\right] + \left(\Lambda - \frac{1}{12}\right)\left[\partial_{xxx}\left(\frac{j_x j_y}{\rho_0}\right) + \partial_{yyy}\left(P + \frac{j_y^2}{\rho_0}\right) + \partial_{zzz}\left(\frac{j_y j_z}{\rho_0}\right) + \partial_{xxz}\left(\frac{j_y j_z}{\rho_0}\right)\right. \\
&+ 2\,\partial_{xyz}\left(\frac{j_x j_z}{\rho_0}\right) + \partial_{xzz}\left(\frac{j_x j_y}{\rho_0}\right) + 3\,\partial_{xyy}\left(\frac{j_x j_y}{\rho_0}\right) + 3\,\partial_{yyz}\left(\frac{j_y j_z}{\rho_0}\right) + \partial_{xxy}\left(P + \frac{j_x^2 + j_y^2}{\rho_0}\right) + \partial_{yzz}\left(P + \frac{j_y^2 + j_z^2}{\rho_0}\right)\left.\right] \\
&- \frac{\Lambda^+}{3}\left(\Lambda - \frac{1}{6}\right)\left[\partial_{xxxx} j_y + 3\,\partial_{yyyy} j_y + \partial_{zzzz} j_y + 6\,\partial_{xxyy} j_y + 6\,\partial_{yyzz} j_y + 2\,\partial_{xxzz} j_y + 4\,\partial_{xxxy} j_x + 4\,\partial_{xyyy} j_x + 4\,\partial_{xyzz} j_x + 4\,\partial_{xyyz} j_y\right. \\
&\left.+ 4\,\partial_{xxyz} j_z + 4\,\partial_{yyyz} j_z + 4\,\partial_{yzzz} j_z + \frac{4}{3}\,\partial_{xxxz} j_x + \frac{4}{3}\,\partial_{xzzz} j_z\right] - \frac{\Lambda}{3}\left(\Lambda - \frac{1}{6}\right)\left[\partial_{xxxx} F_y + 3\,\partial_{yyyy} F_y + \partial_{zzzz} F_y + 6\,\partial_{xxyy} F_y + 6\,\partial_{yyzz} F_y\right. \\
&\left.+ 2\,\partial_{xxzz} F_y + 4\,\partial_{xxxy} F_x + 4\,\partial_{xyyy} F_x + 4\,\partial_{xyzz} F_x + 4\,\partial_{xyyz} F_y + 4\,\partial_{xxyz} F_z + 4\,\partial_{yyyz} F_z + 4\,\partial_{yzzz} F_z + \frac{4}{3}\,\partial_{xxxz} F_x + \frac{4}{3}\,\partial_{xzzz} F_z\right], \\
& \qquad \text{(E16)}
\end{aligned}
$$

$$F_z = \partial_x\left(\frac{j_x j_z}{\rho_0}\right) + \partial_y\left(\frac{j_y j_z}{\rho_0}\right) + \partial_z\left(P + \frac{j_z^2}{\rho_0}\right) - \frac{\Lambda^+}{3}\left[\partial_{xx} j_z + \partial_{yy} j_z + \partial_{zz} j_z + 2\,\partial_z\left(\partial_x j_x + \partial_y j_y + \partial_z j_z\right)\right]$$
$$- \frac{\Lambda}{3}\left[\partial_{xx} F_z + \partial_{yy} F_z + \partial_{zz} F_z + 2\,\partial_z\left(\partial_x F_x + \partial_y F_y + \partial_z F_z\right)\right] + \left(\Lambda - \frac{1}{12}\right)\left[\partial_{xxx}\left(\frac{j_x j_z}{\rho_0}\right) + \partial_{yyy}\left(\frac{j_y j_z}{\rho_0}\right) + \partial_{zzz}\left(P + \frac{j_z^2}{\rho_0}\right) + \partial_{xxy}\left(\frac{j_y j_z}{\rho_0}\right)\right.$$
$$\left. + \partial_{xyy}\left(\frac{j_x j_z}{\rho_0}\right) + 2\,\partial_{xyz}\left(\frac{j_x j_y}{\rho_0}\right) + 3\,\partial_{xzz}\left(\frac{j_x j_z}{\rho_0}\right) + 3\,\partial_{yzz}\left(\frac{j_y j_z}{\rho_0}\right) + \partial_{xxz}\left(P + \frac{j_x^2 + j_z^2}{\rho_0}\right) + \partial_{yyz}\left(P + \frac{j_y^2 + j_z^2}{\rho_0}\right)\right]$$
$$- \frac{\Lambda^+}{3}\left(\Lambda - \frac{1}{6}\right)\left[\partial_{xxxx} j_z + \partial_{yyyy} j_z + 3\,\partial_{zzzz} j_z + \frac{2}{3}\,\partial_{xxyy} j_z + 6\,\partial_{xxzz} j_z + 6\,\partial_{yyzz} j_z + 4\,\partial_{xxxz} j_x + 4\,\partial_{xyyz} j_x + 4\,\partial_{xzzz} j_x + 4\,\partial_{xxyz} j_y\right.$$
$$\left. + 4\,\partial_{yyyz} j_y + 4\,\partial_{yzzz} j_y + 4\,\partial_{xyzz} j_z + \frac{4}{3}\,\partial_{xxxy} j_x + \frac{4}{3}\,\partial_{xyyy} j_y\right] - \frac{\Lambda}{3}\left(\Lambda - \frac{1}{6}\right)\left[\partial_{xxxx} F_z + \partial_{yyyy} F_z + 3\,\partial_{zzzz} F_z + \frac{2}{3}\,\partial_{xxyy} F_z\right.$$
$$\left. + 6\,\partial_{xxzz} F_z + 6\,\partial_{yyzz} F_z + 4\,\partial_{xxxz} F_x + 4\,\partial_{xyyz} F_x + 4\,\partial_{xzzz} F_x + 4\,\partial_{xxyz} F_y + 4\,\partial_{yyyz} F_y + 4\,\partial_{yzzz} F_y + 4\,\partial_{xyzz} F_z + \frac{4}{3}\,\partial_{xxxy} F_x + \frac{4}{3}\,\partial_{xyyy} F_y\right]. \tag{E17}$$

REFERENCES

[1]H. P. Greenspan, *The Theory of Rotating Fluids*, 2nd ed. (Cambridge University Press, 1969).
[2]G. K. Vallis, *Atmospheric and Oceanic Fluid Dynamics: Fundamentals and Large-Scale Circulation*, 2nd ed. (Cambridge University Press, 2017).
[3]G. F. Round, *Incompressible Flow Turbomachines: Design, Selection, Applications, and Theory*, 1st ed. (Butterworth-Heinemann, 2004).
[4]M. Madou, J. Zoval, G. Jia, H. Kido, J. Kim, and N. Kim, "Lab on a CD," Annu. Rev. Biomed. Eng. **8**, 601–628 (2006).
[5]D. Carlo, "Inertial microfluidics," Lab Chip **9**, 3038–3046 (2009).
[6]M. Madadelahi, L. F. Acosta-Soto, S. Hosseini, S. O. Martinez-Chapa, and M. J. Madou, "Mathematical modeling and computational analysis of centrifugal microfluidic platforms: A review," Lab Chip **20**, 1318–1357 (2020).
[7]S. N. Baura, "Secondary flow in a rotating straight pipe," Proc. R. Soc. London A **227**, 133–139 (1954).
[8]G. S. Benton and D. Boyer, "Flow through a rapidly rotating conduit of arbitrary cross-section," J. Fluid Mech. **26**, 69–79 (1966).
[9]H. S. Kheshgi and L. E. Scriven, "Viscous flow through a rotating square channel," Phys. Fluids **28**, 2968 (1985).
[10]U. Lei and C. H. Hsu, "Flow through rotating straight pipes," Phys. Fluids A **2**, 63–75 (1990).
[11]K. Nandakumar, H. Raszillier, and F. Durst, "Flow through rotating rectangular ducts," Phys. Fluids A **3**, 770–781 (1991).
[12]T. Glatzel, C. Litterst, C. Cupelli, T. Lindemann, C. Moosmann, R. Niekrawietz, W. Streule, R. Zengerle, and P. Koltay, "Computational fluid dynamics (CFD) software tools for microfluidic applications—A case study," Comput. Fluids **37**, 218–235 (2008).
[13]G. K. Batchelor, *An Introduction to Fluid Dynamics*, 2nd ed. (Cambridge University Press, 2000).
[14]C. Y. Wang, "Exact solutions of the steady-state Navier-Stokes equations," Annu. Rev. Fluid Mech. **23**, 159–177 (1991).
[15]P. B. Yoseph, J. J. Blech, and A. Solan, "Finite element solution of the Navier-Stokes equations in rotating flow," Int. J. Numer. Meth. Eng. **17**, 1123–1146 (1981).
[16]R. Codina, "Numerical solution of the incompressible Navier–Stokes equations with Coriolis forces based on the discretization of the total time derivative," J. Comput. Phys. **148**, 467–496 (1999).
[17]R. Benzi, S. Succi, and M. Vergassola, "The lattice Boltzmann equation: Theory and applications," Phys. Rep. **222**, 145–197 (1992).
[18]S. Chen and G. Doolen, "Lattice-Boltzmann method for fluid flows," Annu. Rev. Fluid Mech. **30**, 329 (1998).
[19]C. K. Aidun and J. R. Clausen, "Lattice-Boltzmann method for complex flows," Annu. Rev. Fluid Mech. **42**, 439 (2010).
[20]Z. Guo and C. Shu, *Lattice Boltzmann Method and Its Application in Engineering*, 1st ed. (World Scientific Pub Co Inc, 2013).
[21]T. Krüger, H. Kusumaatmaja, A. Kuzmin, O. Shardt, G. Silva, and E. M. Viggen, *The Lattice Boltzmann Method—Principles and Practice*, 1st ed. (Springer, 2016).
[22]S. Succi, *The Lattice Boltzmann Equation: For Complex States of Flowing Matter*, 1st ed. (Oxford University Press, 2018).
[23]R. Salmon, "The lattice Boltzmann method as a basis for ocean circulation modeling," J. Mar. Res. **57**, 503–535 (1999).
[24]R. Salmon, "Lattice Boltzmann solutions of the three-dimensional planetary geostrophic equations," J. Mar. Res. **57**, 847–884 (1999).
[25]P. J. Dellar, "A priori derivation of lattice Boltzmann equations for rotating fluids," preprint (2001).
[26]Z. Guo, C. Zheng, and B. Shi, "Discrete lattice effects on the forcing term in the lattice Boltzmann method," Phys. Rev. E **65**, 046308 (2002).
[27]F. Shi-De, M. Jiang-Yu, and Z. Qiong, "Lattice Boltzmann equation model in the Coriolis field," Chin. Phys. **10**, 1103 (2001).
[28]H. Yu, S. S. Girimaji, and L.-S. Luo, "DNS and LES of decaying isotropic turbulence with and without frame rotation using lattice Boltzmann method," J. Comput. Phys. **209**, 599–616 (2005).
[29]T.-M. Liou and C.-S. Wang, "Large eddy simulation of rotating turbulent flows and heat transfer by the lattice Boltzmann method," Phys. Fluids **30**, 015106 (2018).
[30]C.-S. Wang and T.-M. Liou, "Lattice Boltzmann simulation of turbulent flow in rotating rectangular ducts with various aspect ratios," Phys. Rev. Fluids **5**, 124608 (2020).
[31]J. L. Zhang, Y. Liu, J. F. Zhang, and J. Yan, "Study of force-dependent and time-dependent transition of secondary flow in a rotating straight channel by lattice Boltzmann method," Physica A **388**, 288–294 (2009).
[32]M. Basha, N. A. C. Sidik, and M. Beriache, "Numerical simulation of fluid flow and heat transfer in rotating channels using parallel lattice Boltzmann method," Int. J. Heat Mass Transfer **115**, 158–168 (2017).
[33]A. Kardani, P. Omidvar, and A. Zarghami, "Analysis of thermal flow in a rotating porous U-turn duct using lattice Boltzmann method," Transp. Porous Med. **116**, 295–318 (2017).
[34]P. Werner, J. F. Boussuge, C. Scholtes, and P. Sagaut, "Lattice-Boltzmann modeling of centrifugal buoyancy induced flows in rotating compressor cavities," Phys. Fluids **36**, 015147 (2024).
[35]D. Zhou, Z. Lu, and T. Guo, "A rotating reference frame-based lattice Boltzmann flux solver for simulation of turbomachinery flows," Numer. Methods Fluids **83**, 561–582 (2017).
[36]B. Maneshian, K. Javadi, and M. T. Rahni, "Bubble dynamics in rotating flow under an accelerating field," Phys. Fluids **30**, 082108 (2018).

[37]R. Zhang, C. Sun, Y. Li, R. Satti, R. Shock, J. Hoch, and H. Chen, "Lattice Boltzmann approach for local reference frames," Commun. Comput. Phys. **9**, 1193–1205 (2011).
[38]E. K. Far, M. Geier, and M. Krafczyk, "Simulation of rotating objects in fluids with the cumulant lattice Boltzmann model on sliding meshes," Comput. Math. Appl. **79**, 3–16 (2020).
[39]H. Yoo, M. Bahlali, J. Favier, and P. Sagaut, "A hybrid recursive regularized lattice Boltzmann model with overset grids for rotating geometries," Phys. Fluids **33**, 057113 (2021).
[40]I. Ginzburg, "Lattice Boltzmann modeling with discontinuous collision components: Hydrodynamic and advection-diffusion equations," J. Stat. Phys. **126**, 157–206 (2007).
[41]I. Ginzburg, F. Verhaeghe, and D. d'Humières, "Two-relaxation-times lattice Boltzmann scheme: About parametrization, velocity, pressure and mixed boundary conditions," Commun. Comput. Phys. **3**, 427–478 (2008).
[42]D. d'Humières and I. Ginzburg, "Viscosity independent numerical errors for lattice Boltzmann models: From recurrence equations to "magic" collision numbers," Comput. Math. Appl. **58**, 823–840 (2009).
[43]I. Ginzburg and D. d'Humières, "Multireflection boundary conditions for lattice Boltzmann models," Phys. Rev. E **68**, 066614 (2003).
[44]I. Ginzburg, "Consistent lattice Boltzmann schemes for the Brinkman model of porous flow and infinite Chapman-Enskog expansion," Phys. Rev. E **77**, 066704 (2008).
[45]S. Khirevich, I. Ginzburg, and U. Tallarek, "Coarse-and fine-grid numerical behavior of MRT/TRT lattice-Boltzmann schemes in regular and random sphere packings," J. Comput. Phys. **281**, 708–742 (2015).
[46]Y. Qian, D. d'Humières, and P. Lallemand, "Lattice BGK models for Navier-Stokes equation," Europhys. Lett. **17**, 479–483 (1992).
[47]X. Shan and X. He, "Discretization of the velocity space in solution of the Boltzmann equation," Phys. Rev. Lett. **80**, 65 (1998).
[48]X. Shan, X.-F. Yuan, and H. Chen, "Kinetic theory representation of hydrodynamics: A way beyond the Navier–Stokes equation," J. Fluid Mech. **550**, 413–441 (2006).
[49]G. Silva and V. Semiao, "A study on the inclusion of body forces in the lattice Boltzmann BGK equation to recover steady-state hydrodynamics," Physica A **390**, 1085–1095 (2011).
[50]G. Silva and V. Semiao, "First- and second-order forcing expansions in a lattice Boltzmann method reproducing isothermal hydrodynamics in artificial compressibility form," J. Fluid Mech. **698**, 282–303 (2012).
[51]G. Silva, "Discrete effects on the forcing term for the lattice Boltzmann modeling of steady hydrodynamics," Comput. Fluids **203**, 104537 (2020).
[52]B. Postma and G. Silva, "Force methods for the two-relaxation-times lattice Boltzmann," Phys. Rev. E **102**, 063307 (2020).
[53]X. Nie and N. S. Martys, "Breakdown of Chapman–Enskog expansion and the anisotropic effect for lattice-Boltzmann models of porous flow," Phys. Fluids **19**, 011702 (2007).
[54]I. Ginzburg, "Modélisation des écoulements monophasiques en Milieux Poreux 'Double Milieu' (Darcy-Brinkman) par une approche 'Lattice-Boltzmann Two-Relaxation-Time'," Rapport de la convention CEMAGREF (191040) (2012).
[55]I. Ginzburg, G. Silva, and L. Talon, "Analysis and improvement of Brinkman lattice Boltzmann schemes: Bulk, boundary, interface. Similarity and distinctness with finite elements in heterogeneous porous media," Phys. Rev. E **91**, 023307 (2015).
[56]G. Silva, L. Talon, and I. Ginzburg, "Low- and high-order accurate boundary conditions: From Stokes to Darcy porous flow modeled with standard and improved Brinkman lattice Boltzmann schemes," J. Comput. Phys. **335**, 50–83 (2017).
[57]G. Silva, "Discrete effects on the source term for the lattice Boltzmann modelling of one-dimensional reaction–diffusion equations," Comput. Fluids **251**, 105735 (2023).
[58]R. Cornubert, D. d'Humiéres, and D. Levermore, "A Knudsen layer theory for lattice gases," Physica D **47**, 241 (1991).
[59]I. Ginzbourg and P. M. Adler, "Boundary flow condition analysis for the three-dimensional lattice Boltzmann model," J. Phys. II **4**, 191 (1994).
[60]X. He, Q. Zou, L.-S. Luo, and M. Dembo, "Analytical solutions of simple flows and analysis of nonslip boundary conditions for the lattice Boltzmann BGK model," J. Stat. Phys. **87**, 115–136 (1997).
[61]I. Ginzburg, G. Silva, F. Marson, B. Chopard, and J. Latt, "Unified directional parabolic-accurate lattice Boltzmann boundary schemes for grid-rotated narrow gaps and curved walls in creeping and inertial fluid flows," Phys. Rev. E **107**, 025303 (2023).
[62]I. Ginzburg, "The lattice Boltzmann method with deformable boundary for colonic flow due to segmental circular contractions," Fluids **10**, 22 (2025).
[63]I. Ginzburg and D. d'Humières, "Local second-order boundary method for lattice Botlzmann models," J. Stat. Phys. **84**, 927–971 (1996).
[64]G. Silva and I. Ginzburg, "Reviving the local second-order boundary approach within the two-relaxation-time lattice Boltzmann modelling," Phil. Trans. R Soc. A **378**, 20190404 (2020).
[65]I. Ginzburg and G. Silva, "Mass-balance and locality versus accuracy with the new boundary and interface-conjugate approaches in advection-diffusion lattice Boltzmann method," Phys. Fluids **33**, 057104 (2021).
[66]G. Silva and I. Ginzburg, "Slip velocity boundary conditions for the lattice Boltzmann modeling of microchannel flows," Numer. Methods Fluids **94**, 2104–2136 (2022).
[67]Q. Zou and X. He, "On pressure and velocity boundary conditions for the lattice Boltzmann BGK model," Phys. Fluids. **9**, 1591–1598 (1997).
[68]J. C. C. Verschaeve and B. Müller, "A curved no-slip boundary condition for the lattice Boltzmann method," J. Comput. Phys. **229**, 6781–6803 (2010).
[69]O. R. Mohammadipour, H. Niazmand, and S. A. Mirbozorgi, "Alternative curved-boundary treatment for the lattice Boltzmann method and its application in simulation of flow and potential fields," Phys. Rev. E **89**, 013309 (2014).
[70]B. Dorschner, S. S. Chikatamarla, F. Bösch, and I. V. Karlin, "Grad's approximation for moving and stationary walls in entropic lattice Boltzmann simulations," J. Comput. Phys. **295**, 340–354 (2015).
[71]I. V. Karlin and P. Asinari, "Factorization symmetry in the lattice Boltzmann method," Physica A **389**, 1530 (2010).
[72]G. Mayer and G. Házi, "Direct numerical and large eddy simulation of longitudinal flow along triangular array of rods using the lattice Boltzmann method," Math. Comput. Simul. **72**, 173–178 (2006).
[73]A. T. White and C. K. Chong, "Rotational invariance in the three-dimensional lattice Boltzmann method is dependent on the choice of lattice," J. Comput. Phys. **230**, 6367–6378 (2011).
[74]S. K. Kang and Y. A. Hassan, "The effect of lattice models within the lattice Boltzmann method in the simulation of wall-bounded turbulent flows," J. Comput. Phys. **232**, 100–117 (2013).
[75]G. Silva and V. Semiao, "Truncation errors and the rotational invariance of three-dimensional lattice models in the lattice Boltzmann method," J. Comput. Phys. **269**, 259–279 (2014).
[76]Y. Kuwata and K. Suga, "Anomaly of the lattice Boltzmann methods in three-dimensional cylindrical flows," J. Comput. Phys. **280**, 563–569 (2015).
[77]M. Bauer and U. Rüde, "An improved lattice Boltzmann D3Q19 method based on an alternative equilibrium discretization," arXiv:1803.04937 (2018).
[78]M. Bauer, G. Silva, and U. Rüde, "Truncation errors of the D3Q19 lattice model for the lattice Boltzmann method," J. Comput. Phys. **405**, 109111 (2020).
[79]C. Coreixas, B. Chopard, and J. Latt, "Comprehensive comparison of collision models in the lattice Boltzmann framework: Theoretical investigations," Phys. Rev. E **100**, 033305 (2019).
[80]M. Taha, S. Zhao, A. Lamorlette, J.-L. Consalvi, and P. Boivin, "Large eddy simulation of fire-induced flows using lattice-Boltzmann methods," Int. J. Therm. Sci. **197**, 108801 (2024).
[81]Q. Zou, S. Hou, S. Chen, and G. D. Doolen, "An improved incompressible lattice Boltzmann model for time-independent flows," J. Stat. Phys. **81**, 35–48 (1995).
[82]X. He and L.-S. Luo, "Lattice Boltzmann model for the incompressible Navier–Stokes equation," J. Stat. Phys. **88**, 927–944 (1997).
[83]I. Ginzburg, "Truncation errors, exact and heuristic stability analysis of two-relaxation-times lattice Boltzmann schemes for anisotropic advection-diffusion equation," Commun. Comput. Phys. **11**, 1439–1502 (2012).
[84]M. Hecht and J. Harting, "Implementation of on-site velocity boundary conditions for D3Q19 lattice Boltzmann simulations," J. Stat. Mech. **2010**, P01018.
[85]Comsol, *COMSOL Multiphysics User's Guide 5.0* (Comsol, 2015).
[86]H. Ishigaki, "Analogy between laminar flows incurved pipes and orthogonally rotating pipes," J. Fluid Mech. **268**, 133–145 (1994).
[87]R. S. Maier, R. S. Bernard, and D. W. Grunau, "Boundary conditions for the lattice Boltzmann method," Phys. Fluids **8**, 1788 (1996).
[88]J. Latt, B. Chopard, O. Malaspinas, M. Deville, and A. Michler, "Straight velocity boundaries in the lattice Boltzmann method," Phys. Rev. E **77**, 056703 (2008).